



**HAL**  
open science

# Investigation on 2 $\mu\text{m}$ laser sources based on monoclinic crystals

Romain Cattoor

► **To cite this version:**

Romain Cattoor. Investigation on 2  $\mu\text{m}$  laser sources based on monoclinic crystals. Cristallography. Université de Bordeaux, 2015. English. NNT : 2015BORD0212 . tel-01249609

**HAL Id: tel-01249609**

**<https://theses.hal.science/tel-01249609>**

Submitted on 4 Jan 2016

**HAL** is a multi-disciplinary open access archive for the deposit and dissemination of scientific research documents, whether they are published or not. The documents may come from teaching and research institutions in France or abroad, or from public or private research centers.

L'archive ouverte pluridisciplinaire **HAL**, est destinée au dépôt et à la diffusion de documents scientifiques de niveau recherche, publiés ou non, émanant des établissements d'enseignement et de recherche français ou étrangers, des laboratoires publics ou privés.

UNIVERSITÉ DE BORDEAUX  
CENTRE LASERS INTENSES ET APPLICATIONS

# THÈSE

présentée en vue d'obtenir le grade de Docteur, spécialité "Lasers,  
Matière, Nanosciences"

par

Romain Cattoor

## INVESTIGATION SUR DES SOURCES LASERS ÉMETTANT À $2 \mu\text{M}$ UTILISANT DES CRISTAUX MONOCLINIQUES

Thèse soutenue le 14 septembre 2015 devant le jury composé de :

DR	PHILIPPE BALCOU	Université de Bordeaux	(Président)
Prof.	BENOIT BOULANGER	Université de Grenoble	(Rapporteur)
Prof.	RICHARD MONCORGÉ	Université de Caen	(Rapporteur)
MCF	INKA MANEK-HÖNNINGER	Université de Bordeaux	(Directeur)
Prof.	LIONEL CANIONI	Université de Bordeaux	(co-Directeur)
Dr.	MARWAN ABDOU AHMED	Institut für Strahlwerkzeuge	(Examinateur)
Dr.	MARC EICHHORN	Institut franco-allemand de recherches de Saint-Louis	(Encadrant)



*À mes parents...*



## ACKNOWLEDGMENTS

I would like to thank Inka Manek-Hönninger, who gives me the opportunity to realize this thesis. Without her support and her advices most of the work would not have been published.

I would like to express my gratitude to Marc Eichhorn for offering me the possibility to work on this interesting topic and to present it at international conferences. This work would not have been possible without the French-German research Institute of Saint-Louis (ISL) who allows researchers to work on such innovative topics.

Of course, I would like to thank my parents for their help during all my studies.

I also thank all the people of my group at ISL, more particularly to my office neighbor Stefano Bigotta and his encouragement, Georg Stoepler for his optical elements "freely" available, Thierry Ibach, Antoine Berrou, Christelle Kieleck, Anne Dhollande and Lukasz Galecki for their discussion and help.

I would like to thank and wish good luck to all the PhD students of our group, Marie Blattmann, Christian Kneis and Brenda Donelan.

Special thanks to the internal mechanical workshops of ISL, especially to Marc Christen, Jean-Luc Muller and Jean Urban, who made all the mechanical parts I needed.

I thank Yannick Petit for his expertise on monoclinic crystals and his valuable comments.

I would also like to thank Prof. Richard Moncorgé and Prof. Benoît Boulanger for having accepted to review this thesis. Moreover, I would like to thank Lionel Canioni for the co-direction, and the CELIA laboratory for have offered me the possibility to finish this thesis.

I also thank EASYJET for its very cheap connection between Bordeaux and Basel airport and the SNFC for all hours spend in its comfortable TER200 between Strasbourg and Saint-louis.

# CONTENTS

CONTENTS	vi
LIST OF FIGURES	viii
INTRODUCTION	1
1 LASER THEORY AND PRACTICAL ASPECTS	3
1.1 STIMULATED EMISSION . . . . .	4
1.2 POPULATION INVERSION, PUMPING . . . . .	5
1.3 LASER EQUATIONS . . . . .	6
1.3.1 Three-level system . . . . .	6
1.3.2 Four-level-system . . . . .	8
1.4 LASER RESONATORS . . . . .	9
1.4.1 Stability condition . . . . .	9
1.4.2 Cavity Modes . . . . .	10
1.4.3 Bessel modes . . . . .	11
1.5 THERMAL ISSUES . . . . .	13
1.5.1 Thermal fracture . . . . .	13
1.5.2 Thermal lensing . . . . .	14
2 MONOCLINIC DOUBLE TUNGSTATES	19
2.1 CRYSTAL SYMMETRY . . . . .	20
2.1.1 Seven symmetry systems . . . . .	20
2.1.2 Monoclinic system . . . . .	21
2.1.3 Crystallographic parameters of KREW . . . . .	23
2.2 DIELECTRIC TENSOR IN DIELECTRIC MEDIA . . . . .	25
2.2.1 Susceptibility tensor . . . . .	25
2.2.2 Crystallographic symmetry . . . . .	26
2.3 MEASUREMENT OF THE REFRACTIVE INDICES - PRISM METHOD	28
2.3.1 Description of the method . . . . .	30
2.3.2 Case of biaxial media . . . . .	32
2.3.3 Discussion . . . . .	35

2.4	OPTICAL PROPERTIES . . . . .	36
2.4.1	Refractive indices . . . . .	36
2.4.2	Absorption/Emission along the dielectric axes . . . . .	38
2.4.3	Absorption along the optic axis . . . . .	40
2.5	THERMAL PROPERTIES . . . . .	46
2.5.1	Thermal conductivity . . . . .	46
2.5.2	Thermal expansion . . . . .	46
2.5.3	Temperature dependence of the refractive index . . . . .	47
3	CONICAL REFRACTION	49
3.1	HISTORY OF CONICAL REFRACTION . . . . .	50
3.2	DESCRIPTION OF THE CONICAL REFRACTION . . . . .	53
3.2.1	Origin . . . . .	53
3.2.2	Practical aspects . . . . .	55
3.2.3	Index and wave surfaces and conical refraction . . . . .	57
3.2.4	Influence of those two surfaces on conical refraction . . . . .	58
3.3	MATHEMATICAL THEORY OF CONICAL REFRACTION . . . . .	62
3.3.1	Parameters of conical refraction . . . . .	62
3.3.2	Conical refraction equations . . . . .	63
3.3.3	Diffraction equations . . . . .	64
3.4	DIFFERENT BEAM PROFILES RESULTING FROM CR . . . . .	66
3.4.1	Near field . . . . .	67
3.4.2	Far field . . . . .	68
3.4.3	Raman spot . . . . .	69
4	DISPERSION AND ABSORPTION MEASUREMENT	71
4.1	DISPERSION OF THE OPTIC AXIS . . . . .	72
4.1.1	X-ray diffraction measurements . . . . .	73
4.1.2	Experimental setup . . . . .	73
4.1.3	Results . . . . .	76
4.1.4	Modification of the refractive index " $n_z$ " . . . . .	77
4.1.5	Dispersion of Holmium-doped KYW . . . . .	78
4.1.6	Conclusion . . . . .	79
4.2	ABSORPTION MEASUREMENTS NEAR THE OPTIC AXIS OF $\text{Ho}^{3+}:\text{KYW}$	80
4.2.1	Experimental setup . . . . .	80
4.2.2	Results . . . . .	81
5	LASER EXPERIMENTS	83
5.1	NEODYMIUM KGW - UNCOATED . . . . .	84
5.1.1	Motivation . . . . .	84

5.1.2	Description of the experimental setup . . . . .	84
5.1.3	Result . . . . .	86
5.1.4	Simulation . . . . .	87
5.1.5	Conclusion . . . . .	90
5.2	NEODYMIUM KGW - COATED . . . . .	90
5.2.1	Motivation . . . . .	90
5.2.2	Experimental setup . . . . .	90
5.2.3	Result . . . . .	91
5.2.4	Conclusion . . . . .	92
5.3	HOLMIUM-DOPED CR LASER . . . . .	94
5.3.1	Description of the pump laser . . . . .	94
5.3.2	Description of the crystal used . . . . .	96
5.3.3	Motivation . . . . .	97
5.3.4	CR laser: which configuration ? . . . . .	98
5.3.5	Almost hemispherical CR laser experiments . . . . .	100
5.3.6	ECR laser . . . . .	103
	<b>CONCLUSION AND PERSPECTIVE</b>	<b>107</b>
	<b>A ANNEXES</b>	<b>111</b>
A.1	RÉSUMÉ EN FRANÇAIS . . . . .	113
	<b>BIBLIOGRAPHY</b>	<b>121</b>

## LIST OF FIGURES

1.1	Schematic illustration of the stimulated emission effect. . . . .	4
1.2	Schematic of a two-level system with Einstein's coefficients. . . . .	5
1.3	Scheme of a three-level system. . . . .	6
1.4	Scheme of four-level systems. . . . .	8
1.5	Stability region (in blue) using parameters $g_1$ and $g_2$ . . . . .	9
1.6	Hermit-Gauss and Laguerre-Gauss TEM profiles . . . . .	11
1.7	Bessel-Gauss beam propagation . . . . .	12
1.8	Comparison between Bessel-Gauss and Gaussian beam . . . . .	13
1.9	Thermal lens evolution in a KYW crystal. . . . .	16

2.1	General frame of a crystallographic orientation. . . . .	20
2.2	Schematic of the monoclinic lattices. . . . .	22
2.3	Primitive and based-centered monoclinic frames. . . . .	23
2.4	Boule of KYW. . . . .	23
2.5	Schematic of the different frames. . . . .	27
2.6	Schematic of light propagation inside a prism. . . . .	30
2.7	Deviation angle as a function of the incident angle. . . . .	31
2.8	Error on refractive index measurement vs cutting error. . . . .	34
2.9	Dispersion of the refractive indices of KREW . . . . .	38
2.10	Energy diagram of Ho <sup>3+</sup> in KGW. . . . .	39
2.11	Absorption/emission cross section of Ho <sup>3+</sup> :KLuW. . . . .	40
2.12	Absorption cross section of Nd <sup>3+</sup> :KGW. . . . .	41
2.13	Evolution of absorption coefficients of Ho <sup>3+</sup> :KYW. . . . .	43
2.14	Simulated absorption profiles of Ho <sup>3+</sup> :KYW. . . . .	44
2.15	Variation of the value $\sin^2(\frac{t}{2})$ . . . . .	44
2.16	Simulated absorption profiles with a 2 mrad resolution. . . . .	45
2.17	Simulated emission cross section at 2076 nm. . . . .	45
2.18	Thermal conductivity vs temperature. . . . .	47
3.1	Refractive index surfaces of a biaxial crystal. . . . .	53
3.2	Scheme of a single ray refracted along the optic axis. . . . .	54
3.3	Scheme of a beam passing through a biaxial crystal. . . . .	54
3.4	Scheme of CR beam propagation . . . . .	55
3.5	Representation of the CR output beam . . . . .	56
3.6	Schematic of the external conical refraction (ECR. . . . .	57
3.7	Simulation of conical refraction from surfaces . . . . .	60
3.8	Simulation of conical refraction transition . . . . .	60
3.9	Simulation of conical refraction propagation . . . . .	60
3.10	Simulation of polarized conical refraction transition . . . . .	61
3.11	Scheme showing the semi-angle $A$ of the conical refraction. . . . .	62
3.12	Semi-angle $A$ . . . . .	63
3.13	Representation of a Gaussian beam. . . . .	64
3.14	CR rings intensity profile . . . . .	66
3.15	CR rings intensity profiles with propagation . . . . .	66
3.16	Near field profiles of conical refraction . . . . .	68
3.17	Far field profiles of conical refraction . . . . .	69
4.1	Dispersion of the optic axis in KREW. . . . .	72
4.2	X-ray diffraction pattern of Nd <sup>3+</sup> :KGW. . . . .	73

4.3	Orientation of Nd <sup>3+</sup> :KGW. . . . .	74
4.4	Scheme of the experimental setup. . . . .	75
4.5	Intensity profile of CR . . . . .	75
4.6	Angle V vs wavelength . . . . .	77
4.7	Derivative of refractive indices . . . . .	78
4.8	Optic axis dispersion of Ho <sup>3+</sup> :KYW . . . . .	79
4.9	Absorption profiles near the optic axis of Ho <sup>3+</sup> :KYW . . . . .	81
4.10	Absorption profiles of various polarizations. . . . .	82
4.11	Absorption profiles near the optic axis saturated . . . . .	82
5.1	Scheme showing the different distances within the laser setup. . . . .	85
5.2	Unpolarized linear absorption of Nd <sup>3+</sup> :KGW. . . . .	86
5.3	Laser curves of Nd <sup>3+</sup> :KGW. . . . .	88
5.4	Laser curves of Nd <sup>3+</sup> :KGW. . . . .	89
5.5	Laser curves of Nd <sup>3+</sup> :KGW. . . . .	89
5.6	Laser curves of coated Nd <sup>3+</sup> :KGW. . . . .	91
5.7	Beam profile Nd <sup>3+</sup> :KGW. . . . .	92
5.8	Beam profile Nd <sup>3+</sup> :KGW, IFSW. . . . .	92
5.9	Schematic of the thulium fiber laser. . . . .	94
5.10	Accordability of the Thulium fiber laser. . . . .	95
5.11	Beam propagation of the Thulium fiber laser. . . . .	95
5.12	Absorption vs length of Ho <sup>3+</sup> :KYW (1at%). . . . .	97
5.13	Crystal cuts dispersion. . . . .	98
5.14	Schematic of CR laser 1. . . . .	99
5.15	Schematic of CR laser 2. . . . .	99
5.16	Schematic of CR laser 3. . . . .	100
5.17	Schematic of ECR laser. . . . .	100
5.18	Laser setup showing the linear cavity. . . . .	101
5.19	Output power vs incident pump power Ho <sup>3+</sup> :KYW. . . . .	102
5.20	Output power vs absorbed pump power Ho <sup>3+</sup> :KYW. . . . .	102
5.21	Beam profiles. . . . .	103
5.22	ECR laser experiment. . . . .	105
5.23	ECR laser, output modes. . . . .	106
A.1	Dispersion de l'angle V . . . . .	114
A.2	Absorption du cristal Ho <sup>3+</sup> :KYW près de l'axe optique . . . . .	115
A.3	Courbe laser obtenue avec le . . . . .	116
A.4	Mode laser, Nd <sup>3+</sup> :KGW. . . . .	116
A.5	Simulation de l'absorption avec une résolution de 2 mrad. . . . .	117

A.6	Puissance de sortie vs puissance de pompe absorbée, $\text{Ho}^{3+}:\text{KYW}$ .	118
A.7	Profile du faisceau. . . . .	118



# INTRODUCTION

Lasers (Light Amplification by Stimulated Emission Radiation) are used in many industrial processes. Nowadays, lasers have a lot of practical applications. They can be used to probe matter without influencing it. For example, LiDAR (Light Detection And Ranging equivalent to the well known RADAR), allows to probe the atmospheric concentration of different chemicals. Lot of sensors can be realized using lasers, starting from temperature sensors, flow sensors, deformation sensors and more. Usually the main interest to use laser light is to avoid any contact with the probed object, the non invasive measurement, and also the fact that laser sensors can do their measurements even under hard conditions in terms of temperature, chemical risk, and the insensibility to high electric fields. As the price of lasers has decreased drastically those applications become less and less expensive and are no more reserved to high level experimental research facilities.

The research on lasers is divided into several thematics. One of them is to cover new wavelength ranges. For this purpose new materials are tested, and energy conversion techniques are developed. The physics of laser resonators can also be investigated. For example the research on ultra-short pulses, which also needs research on new materials and optics conception. More technical research can be performed in order to obtain more optical power by scaling up laser systems. Researchers are always pushing to the limit of laser systems. In the beginning there were the rubis laser, gaz lasers and dye lasers. Nowadays, the development of semiconductor lasers provides pump sources for other lasers, easily available. Those lasers have opened the way for Diode Pumped Solid State (DPSS) lasers. A wide range of wavelengths are available today as various regimes (continuous wave (CW), Q-switched, mode-locking...). One of the main work of researchers nowadays is to find a way to obtain a specific regime at a specific wavelength because lasers are just tools which need to be set for each task needed.

A challenging part in the laser field is to increase the output power. In fact, by pushing the limits, effects which were neglected for low output

power have more influence on the laser efficiency. In the case of solid state lasers with bulk materials, the maximal output power available is mainly limited by the thermal effects occurring inside the material. The rapid development of pump diodes provides high pump power easily available. In order to achieve higher output power the heat transferred to the active medium has to be removed. The choice of the material becomes then very critical. Nowadays, the Yttrium Aluminum Garnet (YAG) is the most common material. It exhibits good thermal conductivity and high damage threshold. Furthermore, it can be easily doped with rare earth ions. Those are the two reasons why this material is the most used in laser industry.

The research presented in this thesis is investigating a biaxial material as gain medium along a specific orientation in order to be able to reach higher output power.

Recently, a publication showing a so-called conical refraction (CR) laser attracted some interest. This laser had an efficiency reaching the stokes limit and an excellent beam quality with up to 3 W of output power. As the authors did not observe any thermal effect, this laser was a promising configuration in order to easily increase the output power of lasers. The theory of such a laser is not known up to now. That is why, this thesis has been started. The aim was to check the results of the mentioned publication, using similar Neodymium-doped KGW ( $\text{KGd}(\text{WO}_4)_2$ ) crystals. In a second time, Holmium-doped KYW ( $\text{KY}(\text{WO}_4)_2$ ) crystals have been investigated in order to test this so-called conical refraction laser with a quasi-three-level laser scheme. This was the main motivation of the thesis. During this research we discovered that the way of obtaining the laser effect along the optic axis of a biaxial crystal is not so obvious. Indeed, the properties of those crystals strongly depend on the orientation and on the polarization. Those properties are described in this thesis especially along the optic axis. Therefore, after a brief description of lasers, the description of the biaxial crystals of KGW and KYW is provided in Chapter 2. As the values of refractive indices given in literature were not accurate enough to predict the dispersion of the optic axis, measurements have been carried out for those two crystals. Furthermore, the absorption properties along the optic axis have been investigated. This knowledge is important in order to understand the last Chapter of this thesis. The conical refraction phenomenon being the main topic, the Chapter 3 explains this phenomenon in a simple way. The laser experiments at the end of this thesis present an innovative laser resonator.

# LASER THEORY AND PRACTICAL ASPECTS

1

## INTRODUCTION

In this first chapter, the basic theory is described. Starting from the stimulated emission proposed by Einstein the laser rate equations are given for four-level and quasi-three-level lasers. Only the continuous wave regime is mentioned in this chapter. A lot of energy transfer effects, as upconversion or cross-relaxation are not explained. The different laser modes observable for classical laser resonators are shown. Finally, the thermal issues, especially the thermal lens effect is described. The aim of this chapter is to introduce the basics of lasers in a simple way, showing the thermal limitation of the usual setup. Advanced readers might skip this chapter.

## 1.1 STIMULATED EMISSION

The story of lasers starts with the prediction of the stimulated emission by Einstein in 1917. This phenomenon has been introduced in order to fit the new model of light taking into account levels of energy introduced by Planck in 1900, with the spectral emission of a blackbody. Without this phenomenon the density of energy emitted by a blackbody radiation cannot be predicted due to the fact that the stimulated emission happens more often than the spontaneous emission.

It is really simple to understand that atoms (more often ions in the most case of lasers) can absorb and emit light (photons). The electronic shields of an atom have several energy levels depending on the nature of the atom. Once the electrons of the atom are on an excited state (higher energy level) by absorbing light or being heated, the atom will tend to de-excite (dissipate this energy). This de-excitation occurs by radiative emission and non-radiative (mainly heat). The absorbed and emitted photons depend only on the electronic configuration of the atom, which will determine the frequency  $\nu$  of the light. These are the basic phenomena occurring in an atom. The third effect called stimulated emission, takes place when an atom at the excited state receives an incident photon, there is then a higher probability for the atom to emit a photon. The energies of the emitted photon and the incident photon are equal. This effect occurs only if the transition of equal energy is possible in the atom. That means, it exists a transition of energy  $h\nu$  (with  $h$  the Planck constant and  $\nu$  the frequency) corresponding to the incident photon energy (cf. Figure 1.1).

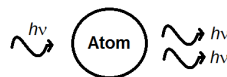


Figure 1.1 – Schematic illustration of the stimulated emission effect.

This phenomenon can be expressed using the Einstein coefficients. Assuming a group of atoms ( $N_{tot}$ ) having  $N_1$  atoms non-excited and  $N_2$  atoms excited, the Einstein coefficients  $A_{21}$  for the spontaneous emission,  $B_{12}$  for the absorption and  $B_{21}$  for the stimulated emission can be used to describe the occupancy of the two levels. Those coefficients correspond to the probability of an atom to be excited or de-excited with a light emission. The coefficient  $A_{21}$  expressed in  $s^{-1}$  gives the probability of spontaneous absorption. Both B factors will influence the level distribution only in presence of an electromagnetic wave with the same energy than the one of the transition. They are expressed in  $J^{-1}.m^3.s^{-2}$ .

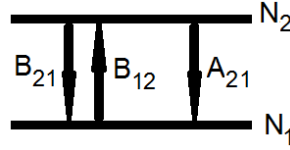


Figure 1.2 – Schematic of a two-level system with Einstein's coefficients.

The variation of the level population follows equation 1.1. Where  $\rho_{\nu_0}$  is the spectral density distribution and  $N_1^e$ ,  $N_2^e$  the populations of levels 1, 2 at thermal equilibrium (cf. Figure 1.2).

$$A_{21}N_2 + B_{21}\rho_{\nu_0}N_2^e = B_{12}\rho_{\nu_0}N_1^e \quad (1.1)$$

$$\frac{N_2^e}{N_1^e} = \frac{g_2}{g_1} \exp\left(-\frac{h\nu_0}{k_b T}\right) \quad (1.2)$$

The thermal occupancy of two different levels at thermal equilibrium is given by the Boltzmann equation 1.2 for a two-level system with  $g_1$  and  $g_2$  the degeneracy of each level,  $k_b$  and  $T$  being the Boltzmann constant and the temperature, respectively.

## 1.2 POPULATION INVERSION, PUMPING

The stimulated emission is the key of laser emission. However, it is not sufficient to create laser emission. Lasers are light amplifiers. In order to amplify one needs optical gain inside an optical medium. The upper level of the two-level system should be more populated than the lower level. At thermal equilibrium this can not occur. The thermal equilibrium population ratio of a two-level system, described by the Equation 1.2, expresses the fact that the upper level is always less populated than the lower level. The population inversion consists to increase this ratio to obtain an abnormal situation with more population on the upper level. This is done by adding energy to the system, to force the population to be on the upper level. The material is "pumped", by adding this energy. The pumping of the medium can be performed electrically or optically. Nowadays, most of the lasers are pumped by laser diodes or other lasers. They are replacing the flash-lamp pumping since they exert a better overall efficiency. Some gaz lasers pumped by electrical discharge, are still commercially available due to the fact that they cover specific wavelengths which can not be easily reached by other lasers with the power required for their applications.

This population ratio is defined by the factor  $\beta_{pop}$  being equal to the difference of the number of atoms on the excited and ground state

( $\beta_{pop} = \frac{N_2}{N_{tot}}$ ). The inversion population occurs when  $\beta_{pop}$  is superior to 0.5. This beta factor can be used to estimate the gain of a laser medium, knowing the total population  $N_{tot}$  and the absorption cross section  $\sigma_a$  and the emission cross section  $\sigma_e$  expressed in  $\text{cm}^2$ . The equation (1.3) can be then used to predict the optical gain of a medium for a specific frequency. This equation is used to rapidly estimate the potential laser transition of a crystal. It is important to note that this equation is always valid and does not depend on the pumping scheme. In fact, the pumping scheme is taken into account in the parameter  $\beta_{pop}$  related to the population inversion.

$$g(\nu) = [\beta_{pop} \cdot \sigma_e(\nu) - (1 - \beta_{pop}) \cdot \sigma_a(\nu)] N_{tot} \quad (1.3)$$

### 1.3 LASER EQUATIONS

In this section the basic laser equations are given. The difference between the four-level system and quasi-three level system is discussed.

#### 1.3.1 Three-level system

The three-level system is of course represented by three energy levels. The lower level  $N_0$  is composed of several levels but with energy differences on the order of the thermal energy. That means all those sub-levels can be considered as only one level since at room temperature.

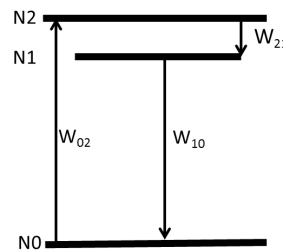


Figure 1.3 – Scheme of a three-level system.

With such a system (see Figure 1.3) the gain medium can absorb for the pumping wavelength (corresponding to the  $0 \rightarrow 2$  transition) and the lasing wavelength (corresponding to the  $1 \rightarrow 0$  transition). That means that when one wants to amplify the lasing wavelength additional losses are created by re-absorption. In order to be able to obtain laser operation in such a system one needs more pumping energy in order to compensate those re-absorption losses. In practice, strict three-level systems do not really exist due to the sub levels of the ground level, they are called quasi-

three-level. In this thesis the term quasi-three-level system just refers to the re-absorption.

The principal equation in order to be able to predict the output power of a laser is the conservation of the energy in the laser cavity. In fact, the circulating power is amplified by the gain medium and reflected by mirrors. In order to have some power out of the laser cavity one of the mirrors is only partially reflective, this is the output coupler with a transmission of  $T_{OC}$ . The value of the output coupler has to be chosen with respect to the gain of the laser medium. Indeed, an optimum value of this output coupler gives a better overall efficiency of the system. The output coupler induces some losses which have to be compensated by having more gain. Some other losses are generated by diffraction inside the laser cavity, or unwanted reflection losses on the element interfaces. Those losses will be expressed by the term  $\Lambda$ . For most of the systems this term is in the order of a few percent at maximum in order to easily reach the threshold of the laser.

The conservation of the energy in the laser systems gives the relation (1.4). It expresses the fact that the gain ( $G$ ), here without unit ( $G = e^{gL}$  with  $L$  the length of the gain medium), has to compensate the losses of the system. In fact, the pumping energy of a laser system is needed to create a gain able to compensate the losses, then the laser emission can be observed. All the energy added by the pumping system is then only used to generate more output power of the laser.

$$(1 - T_{OC})(1 - \Lambda)G^2 = 1 \quad (1.4)$$

It is possible to calculate the threshold of the laser using equation (1.6) with the saturation intensity defined by equation (1.5) taken from [1]. Those equations are derived from the laser rate equations which are not described in this thesis. They express the variation of the population for the different levels.

$$I_{sat} = \frac{hc}{\lambda_p(\sigma_a^s + \sigma_e^s)\tau_{flu0}} \quad (1.5)$$

In this equation,  $\lambda_p$  is the pump wavelength,  $\sigma_a^s$  and  $\sigma_e^s$  the absorption and emission cross sections at the laser (signal) wavelength.  $\tau_{flu0}$  corresponds to the fluorescence lifetime of the electronic transition. The pumping intensity of the laser will have to reach this saturation intensity in order to obtain population inversion.

The laser threshold can be estimated using the following equation:

$$P_{th} = \frac{I_{sat}S}{\eta_{abs}} (\ln G + \sigma_a(\lambda_s)NL) \quad (1.6)$$

The term  $\eta_{abs}$  is the fraction of the absorbed pump power. The term  $S$  corresponds to the area of the pump beam.  $G$  is the gain,  $N$  the ion concentration, and  $L$  the gain medium length. This expression is approximate. It assumes a nearly perfect overlap of the pump and cavity modes inside the gain medium.

The output power of the laser is then expressed by equation (1.7) where  $R_{OC}$  is the reflectivity of the output coupler.

$$P_{out} = \frac{\lambda_p - \log R_{OC}}{\lambda_s} \frac{1}{2 \log G} \eta_{abs} (P_p - P_{th}) \quad (1.7)$$

Those simple equations are very practical in order to estimate the laser threshold and select the design of a gain medium.

### 1.3.2 Four-level-system

In four-level lasers, ions in the laser medium can be considered to have four-levels as shown in Figure 1.4. In the schematic,  $N_i$ , with  $i = 0, 1, 2, 3$ , representing the normalized electron population on each level.  $W_{ij}$  is the rate transition in electrons per second, and  $\tau_{ij}$  the lifetime of the transitions.

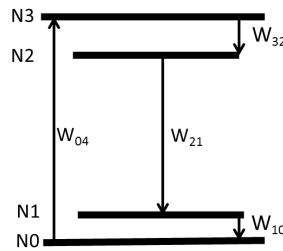


Figure 1.4 – Scheme of four-level systems.

The population inversion in the case of four-level systems occurs between level 3 and 2. For this purpose, the transitions  $4 \rightarrow 3$  and  $2 \rightarrow 1$  have to be much faster than the transition  $3 \rightarrow 2$ . In this case there are always more ions in the state three than in the state two. This leads to inversion of population as soon as one starts to pump the material.

The laser rate equations derived from such simple system are similar to the case of the three-level systems. Only the terms taking into account the re-absorption of the lasing wavelength have to be removed.

## 1.4 LASER RESONATORS

### 1.4.1 Stability condition

#### Two mirror cavity

The stability condition of a laser resonator is the key condition to build up a laser. In the case of a cavity composed of two mirrors, this stability condition can be written in a simple way using the well-known parameters  $g_1$  and  $g_2$ .

Those parameters depend on the mirrors used. They are given in the equation (1.8). The multiplication of those parameters should follow  $0 \leq g_1 g_2 \leq 1$ .

$$g_1 = 1 - \frac{L}{R_1} \quad g_2 = 1 - \frac{L}{R_2} \quad (1.8)$$

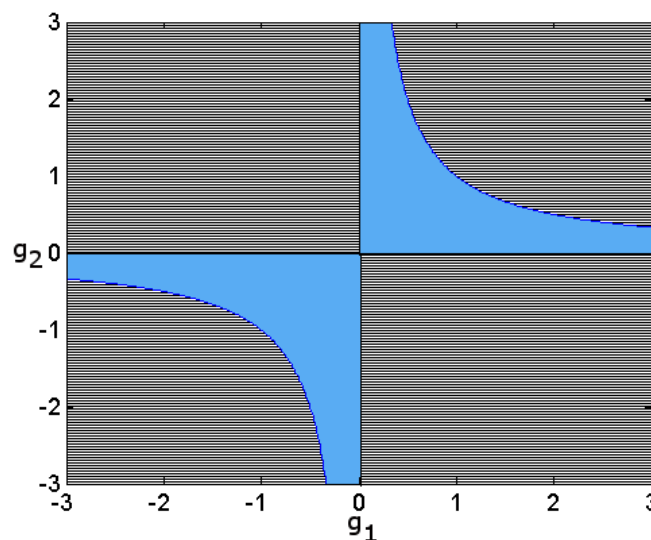


Figure 1.5 – Stability region (in blue) using parameters  $g_1$  and  $g_2$ .

Those simple equations are used in order to describe only two mirror cavities. Using the  $(g_1, g_2)$  coordinates the stability point is easily asset for a plano-plano cavity  $(1,1)$  (see Figure 1.5).

#### Using ABCD matrix

The ABCD matrix system is used to describe the beam propagation. The geometric optics approach is very powerful since most of the optical components can be described by such a matrix. The cavity matrix is determined by simply multiplying the matrix elements. The stability is expressed by equation (1.9)

$$0 \leq \frac{A + D + 2}{4} \leq 1 \quad (1.9)$$

This approach allows to take into account the variation of different parameters inside the laser cavity, as the thermal lens created inside the laser medium. This study is performed at the end of this chapter using this method.

### 1.4.2 Cavity Modes

The classical modes are determined by the alignment of the laser cavity. In order to obtain the best efficiency one has to use the fundamental mode which is the Gaussian mode. This mode provide excellent beam quality and high energy density.

It mainly exists two types of modes in order to describe the laser cavity modes, the Hermit-Gauss and the Laguerre-Gauss. The term Gauss, is always present, since those modes are always restricted as a Gaussian mode. Otherwise those modes exert an infinite transverse mode. The Laguerre-Gauss mode describes modes with cylindrical symmetry. Such kind of modes can be observed in fiber lasers for example. The Hermit-Gauss modes are present for rectangular symmetry, this is often the case of misaligned conventional cavities with mirrors.

The electric field of the Hermit-Gauss mode can be calculated using the equation (1.10) and the Laguerre-Gauss one by the equation (1.11). The factors  $m, n$  (horizontal, vertical) and  $l, p$  (azimuthal, radial) correspond to the order of the mode for Hermit-Gauss and Laguerre-Gauss, respectively. When those parameters are set to zero the mode corresponds to the classical Gaussian case, i.e. the Transverse Electromagnetic Mode  $00$  ( $TEM_{00}$ ).

$$E_{mn} \propto \frac{1}{\sqrt{1+Z^2}} H_m \left( X \sqrt{\frac{2}{1+Z^2}} \right) H_n \left( Y \sqrt{\frac{2}{1+Z^2}} \right) \exp\left(-\frac{X^2 + Y^2}{1+Z^2}\right) \\ \times \exp\left(-i\left(\frac{(1+Z)\pi R}{\lambda} + \frac{(X^2 + Y^2)Z}{1+Z^2} - (m+n+1)\left(\frac{\pi}{2} - \arctan\left(\frac{1-Z}{1+Z}\right)\right)\right)\right)$$

with  $X = x \sqrt{\frac{2\pi}{R\lambda}}, \quad Y = y \sqrt{\frac{2\pi}{R\lambda}}, \quad Z = z \frac{2}{R}$

(1.10)

$$\begin{aligned}
E_{lp} \propto & \cos(l\theta) \frac{(2\rho)^l}{(1+Z^2)^{\frac{l+1}{2}}} L_p \left( \frac{(2\rho)^2}{1+Z^2} \right) \exp\left(-\frac{\rho^2}{1+Z^2}\right) \\
& \times \exp\left(-i\left(\frac{(1+Z)\pi R}{\lambda} + \frac{\rho^2 Z}{1+Z^2} - (l+2p+1)\left(\frac{\pi}{2} - \arctan\left(\frac{1-Z}{1+Z}\right)\right)\right)\right) \\
\text{with } & \rho^2 = X^2 + Y^2, \quad Z = z \frac{2}{R}.
\end{aligned} \tag{1.11}$$

Few different modes are shown on Figure 1.6.

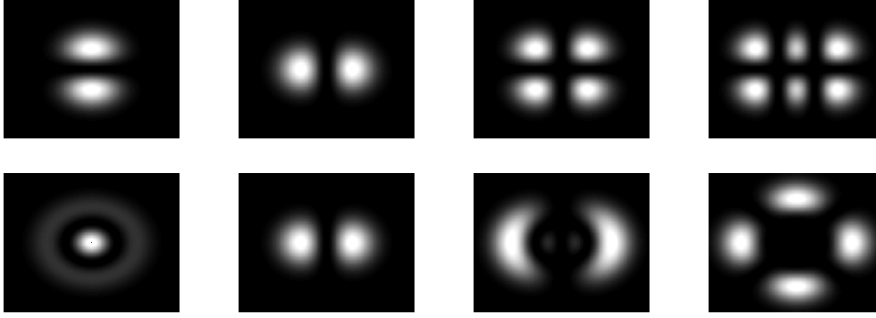


Figure 1.6 – Hermit-Gauss modes on the top, and Laguerre-Gauss modes on the bottom and from left to right  $TEM_{01}$ ,  $TEM_{10}$ ,  $TEM_{11}$ ,  $TEM_{21}$ .

### 1.4.3 Bessel modes

Here, it is useful to describe also an other kind of mode, which is not directly present in classical laser cavities, the Bessel-Gauss mode. In this case it is a simple Bessel function restricted by a Gaussian mode for the same reason than for the two previous ones. It is interesting to know that this kind of modes have attracted more and more interest in the last years. Indeed, the true Bessel (with infinite energy) beams are diffraction free. In practice, only Bessel-Gauss beams can be generated. Pure Bessel beams would need an infinite amount of energy. However, this is sufficient to observe interesting properties as beam healing, and longer 'Rayleigh range' than for classical Gaussian beams. Such a beam can be generated using diffracting surfaces, spatial light modulators etc. The conical refraction can be a way to generate such a beam but with complex polarization dependency. In fact, the most commonly used way to generate Bessel-Gauss beams are inefficient or power limited by the used optical element. The use of conical refraction in order to generate such a beam can be a way to increase the power if it is needed. In fact, nowadays Bessels-Gauss beams are studied only at low power. Thus, high output power is still not required.

The electric field of a Bessel-Gauss beam can be simply expressed by equation (1.12) from [2]. With  $w_0$  the waist of the Gaussian beam,  $z_0$  the Rayleigh range ( $= \frac{\pi w_0^2}{\lambda}$ ),  $\Psi$  the phase shift,  $k$  the wave vector ( $= \frac{2\pi}{\lambda} = \sqrt{k_\rho^2 + k_z^2}$  with  $k_\rho = \sqrt{k_x^2 + k_y^2}$ ) and  $A$  the angle of the incident plane wave as shown on Figure 1.7. It is important to note that when  $A = 0$ , the result is a simple plane wave. The perfect Bessel beam is reached when the waist of the Gaussian envelope tends to the infinite.

$$E_m(\rho, z = 0) \propto J_n(k_\rho \sin(A)) e^{-\left(\frac{\rho}{w_0}\right)}$$

$$E_m(\rho, z) \propto \frac{w_0}{w(z)} J_n\left(\frac{k_\rho \sin(A)}{1 + \frac{iz}{z_0}}\right) e^{i\left(\left(k - \frac{(k_\rho \sin(A))^2}{2k}\right)z - \Psi(z)\right)} e^{\left(-\frac{A}{w(z)^2} + \frac{ik}{2z\left[1 + \left(\frac{z_0}{z}\right)^2\right]}\right)\left((\rho^2 + k_\rho \sin(A))^2 \frac{z^2}{k^2}\right)}$$
(1.12)

One of the applications of Bessel-Gauss beams could be the propagation in atmosphere. Hence, the beam degradation due to atmospheric turbulences is reduced. If the beam is large enough, due to the beam healing properties, it can be focused behind small objects. The minimal distance needed to reconstruct the Bessel beam profile can be estimated using equation (1.13) [3].

$$z_{reconstruct} = \frac{w_{object} k}{2k_z}$$
(1.13)

There is a main drawback of such a beam compared to the classical Gaussian beam. It is the intensity! Bessel-Gauss beams always have less energy in the center region than classical Gaussian beams. In order to obtain the same intensity at the central part of the beam (drawn on Figure 1.8, one needs to have almost a factor  $\gamma = 1.5$  times more power for a Bessel-Gauss beam (with  $\gamma = \frac{\int I_{Gaussian}}{\int I_{Bessel-Gaus}}$ ). This limits drastically the benefits of such a beam.

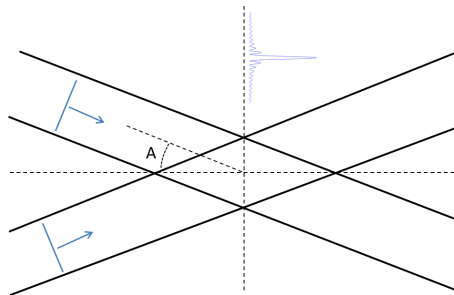


Figure 1.7 – Bessel-Gauss beam propagation created using two plane waves with a cone angle  $A$ .

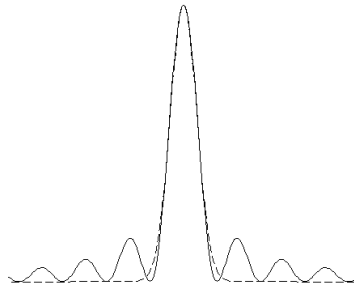


Figure 1.8 – Intensity profiles, comparison between a Bessel-Gauss (full line) and a Gaussian beam (dashed line) for beams having the same intensity in the center region.

Several publications are describing how to obtain Bessel resonators [4, 5]. These results are not described here. However, it is important to keep in mind that the conical refraction phenomenon described in Chapter 3 is a way to obtain such beams.

## 1.5 THERMAL ISSUES

By increasing the power of a laser the thermal load inside the laser medium also increases. This thermal load cannot be avoided and is mainly generated due to the "quantum defect" of the laser transition. This heat modifies the properties of the laser medium. Those modifications reduce the overall laser efficiency. Even if this heat can be removed efficiently, a thermal gradient will still be present in the medium and modify the transverse optical path length distribution of the laser beam. Almost all parameters are temperature dependent as the lattice parameters of the medium, the thermal conductivity, and the spectroscopic properties of the laser medium. In this section we will discuss the amplitude of those modifications and their influence on the overall efficiency of the laser. The ultimate limit of a laser medium is the fracture of the material caused by a too strong stress build-up on the crystal.

### 1.5.1 Thermal fracture

The ultimate limit of a solid state laser is the fracture of the crystal. This can be avoided by choosing reasonable doping concentration, pump intensity, and cooling design. The thermal fracture of a material occurs when the mechanical stress inside the material reaches the ultimate tensile strength (also called ultimate strength or simply tensile strength) value of the material.

Crystal	Value	Ref.
YAG	200 MPa	[6]
KGW	63–137 MPa	[7]

Table 1.1 – *Ultimate tensile strength parameter of KGW in comparison with YAG.*

This parameter is on the order of hundred MPa for most of the dielectric media used as gain media. The value of the ultimate strength for two crystals is given in Table 1.1. The higher this limit the more resistant will be the material.

The internal pressure of the crystal under diode pumping can be estimated using finite element analysis. Of course, in the case of lasers, the pump intensity and some other parameters as the thermal conductivity and the Young modulus of the material have to be taken into account.

In real conditions the mounting of the crystal often adds some initial stress. This results in a lower pressure limit than the measured one.

## 1.5.2 Thermal lensing

### Cylindric configuration

The thermal lens results from the heat deposition on the material. In the case of a Gaussian laser pumping scheme the intensity profile is given by the equation 1.14 [6]. Where  $\alpha_0$  is the linear absorption and  $w_p$  the radius of the pump beam.

$$I(r, z) = I_0 e^{-2\frac{r^2}{w_p^2}} e^{-\alpha_0 z} \quad (1.14)$$

For a radial heat flow the thermal focal lens can then be expressed by equation 1.15 [6]. The term  $P_{heat}$  corresponds to the thermal load generated by the absorbed pump power,  $P_{heat} = P_{abs}\eta_{heat}$ , with  $\eta_{heat}$  the fraction of the absorbed pump power converted into heat ("thermal fractional load").

$$f = \frac{\pi K w_p^2}{P_{heat} \frac{dn}{dT}} \frac{1}{1 - e^{-\alpha_0 l}} \quad (1.15)$$

In that case the thermal bulging of the facets of the crystal is not taken into account. However, for high power those thermal bulging has a non negligible contribution on the thermal lens.

The thermal lens is driven by three temperature dependent properties. The most important is the refractive index variation  $\frac{dn}{dT}$ . The other one is due to the stress induced by the heating, and modifying also the refractive indices, called the photo-elastic effect ( $P_{PE}$ ). Those two result in

Parameter	Value
K	2.8 W.m <sup>-1</sup> .K <sup>-1</sup>
w <sub>p</sub>	100 μm
$\frac{dn}{dT}$	-120 × 10 <sup>-7</sup>
n <sub>0</sub>	2
α <sub>T</sub>	2.8 W.m <sup>-1</sup> .K <sup>-1</sup>
ν	0.3

Table 1.2 – List of parameters of KYW used to show the thermal lens evolution.

a change of the refractive indices while the thermal load increases. The last parameter which is part of the overall thermal lens results from geometrical aspects. In fact under high power the crystal tends to expand which is resulting in a bulging of the facets of the crystal. This additional contribution,  $Q_{dist}$ , creates a positive lens.

The optical power of the overall lens can then be determined using the equation 1.16 [8] in the plane stress approximation. This approximation is used for long and thin crystals. In the case of a ratio between the length and the diameter of the crystal of 1.5, this term overestimates the bulging effect by 35% [9]

$$D = \frac{1}{f} = \frac{P_{heat}}{2\pi K w_p^2} \left( \frac{dn}{dT} + P_{PE} + Q_{dist} \right) \quad (1.16)$$

The bulging term can be expressed as  $Q_{dist} = (n_0 - 1)(1 + \nu)\alpha_T$ , with  $\nu$  the Poisson ratio and  $\alpha_T$  the thermal expansion coefficient.

The photo-elastic effect is expressed as  $P_{PE} = 2n_0^3\alpha_T C$ , where C is the photo-elastic coefficient depending on the radial and azimuthal position.

Those equations can be used in order to estimate the thermal lens which will result from the monoclinic double tungstate crystal. On Figure 1.9 is plotted a simple case using the parameters shown in Table 1.2. This case corresponds to a KYW crystal, but without any anisotropy taken into account. In fact, as it will be described in the next Chapter the parameters of such a crystal strongly depend on the orientation and then exert an asymmetric thermal lens effect. The values plotted here are just given to have an order of magnitude.

In the simple case present here, the created thermal lens is negative. Depending on the crystal properties this lens can either be positive or negative. All those parameters will be strongly dependent on the orientation in the case of monoclinic double tungstates. This will give rise to an astigmatic thermal lens and some possibility to obtain a so called ather-

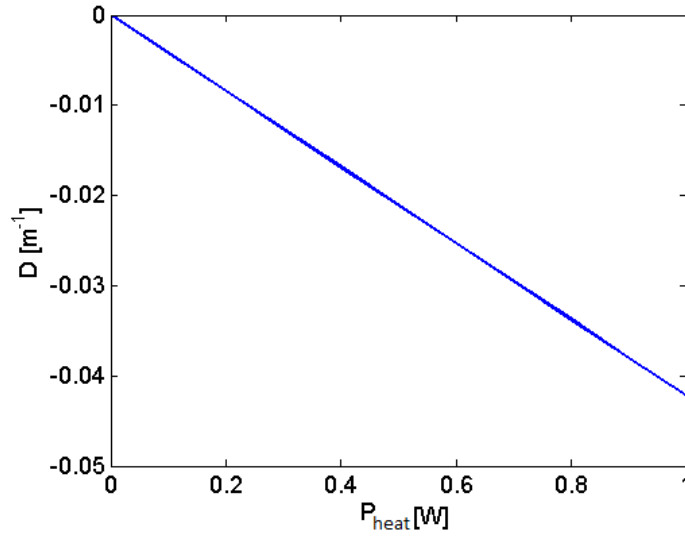


Figure 1.9 – Thermal lens evolution in a KYW crystal with the parameters in Table 1.2.

mal propagation direction, in which the thermal lensing will be drastically reduced.

Such an athermal direction can be calculated considering different parameters depending on the experimental conditions. The variation of the optical path length with the temperature should be zero. In literature one can find two definitions of the athermal direction, the etalon configuration and the laser cavity configuration [10]. The first one corresponds to light propagating through a crystal in which the variation of the interference fringe ( $\Delta F$ ) with the temperature (representing the variation of the optical path length) is expressed by the equation (1.17). In the case of the so-called laser cavity configuration, the back reflection of the light by a mirror is taken into account. In this case the variation of the fringe with the temperature is given by the equation (1.18).

$$\frac{\Delta F}{\Delta T} = \frac{2L}{\lambda} \left[ \frac{dn}{dT} + n\alpha \right] \quad (1.17)$$

$$\frac{\Delta F}{\Delta T} = \frac{2L}{\lambda} \left[ \frac{dn}{dT} + (n-1)\alpha \right] \quad (1.18)$$

In those two equations the crystal is considered to be heated uniformly [10]. Furthermore, we can see that the term  $P_{PE}$  present in the equation (1.16) is neglected.

The athermal direction is obtained when the fringe variation is equal to zero.

Thus in the case of the laser cavity configuration one has to find an orientation which fulfills equation (1.19).

$$\frac{dn}{dT} = -(n - 1)\alpha \quad (1.19)$$

This equality can be obtained only for some orientation in anisotropic media.



# MONOCLINIC DOUBLE TUNGSTATES

## INTRODUCTION

This chapter is devoted to the study of the properties of monoclinic double tungstates (KYW, KGdW, KLuW). Those materials have been intensively studied during the last decades. Even if several publications describe the optical properties, the complexity of those crystals always imposes some uncertainty on their measurements and interpretation. Simple parameters as the refractive indices are still not well known, or at least not well enough to predict the orientation of the optic axis. In the first section of this chapter, the tools needed to understand into detail monoclinic crystals are given. A short description of the symmetry system will help the reader to be familiar with those low symmetry crystals. Afterwards, a thorough description of the refractive index measurements is given. The aim of this demonstration is to explain the origin of the measurement uncertainties often present in the literature. Reading those first sections the reader will be able to easily understand the different properties describing those crystals. The refractive indices available in literature are provided as well as the absorption for Holmium-doped KYW and Neodymium-doped KGW is discussed. The absorption dependency with both orientation and polarization near the optic axis is investigated theoretically. This investigation is of great importance for the absorption measurements presented in Chapter 4 and the laser experiments presented in Chapter 5.

## 2.1 CRYSTAL SYMMETRY

Before going into the detailed description of the monoclinic system, an overview of all crystallographic symmetry systems with their specific notations will be provided. This section will only focus on optical properties of crystals. A thorough description of the symmetry and group theory will not be provided. More details can be found in the book written by Powell [11]. Then the focus will be rapidly on the monoclinic case and the consequences on optical properties.

### 2.1.1 Seven symmetry systems

Crystals are ordered matter. The atoms, or group of atoms, in crystals are periodically arranged. The same structure is repeated along the whole volume of the crystal. This initial structure defines the lattice parameters and further the crystallographic system of the crystal. It exists seven symmetry systems depending on the lattice parameters. These parameters are  $a$ ,  $b$  and  $c$ , the length of the space between two identical structures along a specific orientation, and  $\alpha$ ,  $\beta$  and  $\gamma$ , the angles between those orientations. A classical representation of those parameters is drawn in Figure 2.1.

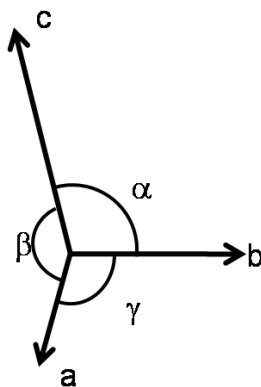


Figure 2.1 – General frame of a crystallographic orientation.

These parameters have different values depending on the shape of the unit cell of the crystal. Even for the simple case of a mono-atomic crystal several arrangements are possible. The lattice parameters depend on this arrangement. The seven symmetry systems are described by specific conditions of these lattice parameters. In table 2.1, all the systems are referenced with their parameters and optical class.

For this thesis only biaxial crystals are interesting, due to the fact that the effect of conical refraction occurs only in such crystals. The discussion is focused on the monoclinic system since the availability of monoclinic

System	Parameters	Optical class
Triclinic	$a \neq b \neq c$ $\alpha \neq \beta \neq \gamma \neq 90^\circ$	Biaxial
Monoclinic	$a \neq b \neq c$ $\alpha = \gamma = 90^\circ \neq \beta$	Biaxial
Orthorhombic	$a \neq b \neq c$ $\alpha = \beta = \gamma = 90^\circ$	Biaxial
Trigonal	$a = b = c$ $\alpha \neq \beta \neq \gamma$	Uniaxial
Tetragonal	$a = b \neq c$ $\alpha = \beta = \gamma = 90^\circ$	Uniaxial
Hexagonal	$a = b \neq c$ $\alpha = \beta = 90^\circ; \gamma = 120^\circ$	Uniaxial
Cubic	$a = b = c$ $\alpha = \beta = \gamma = 90^\circ$	Isotropic

Table 2.1 – Description of the seven crystallographic systems.

double tungstate crystals as laser material and their capabilities to exhibit conical refraction are of great interest for later experiments. As it will be discussed in the next chapter some other biaxial crystals might be investigated.

### 2.1.2 Monoclinic system

The monoclinic system is described by an axial symmetry along one of the crystallographic axes or a mirror symmetry. The lattice parameters are all different. Two angles within the plane perpendicular to the symmetry axis (or parallel to the mirror plane) are equal to  $90^\circ$ . The monoclinic systems can be divided into three classes depending on the nature of the symmetry: the monoclinic-sphenoidal class having an axial symmetry, the monoclinic-domatic class having a mirror symmetry and finally, the monoclinic-prismatic class exhibiting axial and mirror symmetries. Those different classes existing within the monoclinic system are of great interest. Indeed, the monoclinic-prismatic class, to which belong monoclinic double tungstate crystals, is centro-symmetric. That means, there is a center of symmetry. Due to this symmetry, some effects as piezo-electricity, pockels effect, frequency doubling ( $\chi^2 = 0$ ) do not exist for such crystals [12]. Thus, they are generally good candidates for higher order effects as Raman conversion ( $\chi^3$ ) or Kerr effect since no energy is lost in the pre-

viously mentioned effects. Only the monoclinic-prismatic class exhibits such properties within the monoclinic system.

Two different Bravais lattices can be used to describe the monoclinic systems. The monoclinic symmetry can be either determined in a primitive (P) lattice or in a based-centred (C) lattice. The difference between those lattices is shown on Figure 2.2. In the case of monoclinic double tungstates, it exists a two-fold symmetry ( $C_2$ ) and a mirror symmetry perpendicular to the  $\mathbf{b}$ -axis ( $C_2/c$ ). It is conventional to use the  $C_2/c$  space group in order to describe monoclinic double tungstate crystals. However, in some publications one can find the space group  $P_2/c$  (also noted  $I_2/c$ ). A simple transformation, shown in equation (2.1) can be used to switch from one lattice to the other. Furthermore, sometimes the  $P_2/a$  space group is used. One can obtain it by permuting the axes  $a$  and  $c$  of the  $P_2/c$  space group.

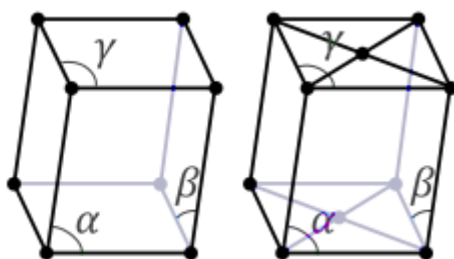


Figure 2.2 – Schematic of the primitive (on the left) and the based-centered (on the right) monoclinic lattices.

$$\begin{aligned} a_c &= a_p + c_p \\ b_c &= -b_p \\ c_c &= -c_p \end{aligned} \quad (2.1)$$

with the different parameters corresponding to the axes indicated in Figure 2.3.

In practice, during the crystal growth by the TSSG (Top Seeded Solution Growth) method the crystal has the shape of the primitive Bravais lattice ( $P_2/c$ ). Therefore, it is useful to specify the used frame when describing the crystal orientation.

The importance of this crystallographic frame is crucial when measurements have to be performed along a specific orientation. This leads to strong differences between several publications for the same values since they are not measured within the same crystal orientation. Those rather complicated notations add confusion in the description of the monoclinic double tungstates.

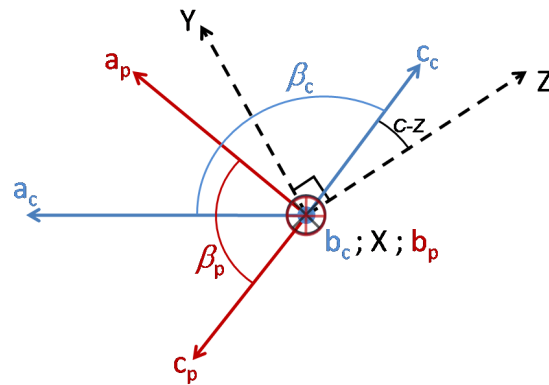


Figure 2.3 – Primitive and based-centered monoclinic frames.

Since the notation  $C_2/c$  is the most commonly used, it is this space group that we will mostly use to describe and compare the different monoclinic double tungstate crystals. Some authors claim that the base-centered system should be used to describe the monoclinic double tungstates [13] according to international nomenclature.

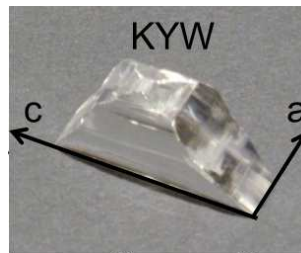


Figure 2.4 – Boule of KYW grown along the crystallographic  $b$ -axis, the  $a$  and  $c$  direction are shown corresponding to the  $P_2/c$  space group, picture from FEE GmbH.

### 2.1.3 Crystallographic parameters of KREW

This thesis is in large part devoted to the use of KGW and KYW crystals which belong to the monoclinic double tungstates KREW family, with RE (Rare Earth) ions. It exists mainly three ions used to create monoclinic double tungstates, Gadolinium (Gd), Yttrium (Y) and Lutetium (Lu). In order to use those materials as laser gain media they are doped with classical rare earth ions used for laser operation as Neodymium ( $Nd^{3+}$ ), Ytterbium ( $Yb^{3+}$ ), Erbium ( $Er^{3+}$ ), Thulium ( $Tm^{3+}$ ), Holmium ( $Ho^{3+}$ ) and others... Doping concentrations up to 100% have been realised using Holmium ions [14]. There are several publications giving the crystallographic parameters of the KREW. The ones shown in Table 2.2 are the most accurate measurements performed using the true  $C_2/c$  space group. The crystallographic matrices (KYW, KGW, KLuW) are very similar, and

Crystal	Space group	a	b	c	$\beta$	Ref.
KGW	$C_2/c$	10.652	10.374	7.582	$130.80^\circ$	[15]
KLuW	$C_2/c$	10.576	10.214	7.487	$130.68^\circ$	[16]
KYW	$C_2/c$	10.64	10.35	7.54	$130.5^\circ$	[17]

Table 2.2 – Lattice parameters of KREW, previously introduced in Figure 2.3, in Ångström.

this results in very similar properties (described in the following) for all those matrices.

## 2.2 DIELECTRIC TENSOR IN DIELECTRIC MEDIA

The most important parameter in an optical material is the dielectric permeability tensor (usually named dielectric tensor). This tensor of rank two carries the principal information for light propagation through the medium. It defines the propagation directions and the absorption properties.

In this section, the origin of this tensor will be briefly discussed and a thorough description is performed.

### 2.2.1 Susceptibility tensor

The dielectric tensor comes from the link between the electric field  $\vec{E}$  and the macroscopic polarization  $\vec{P}$  of the medium. This polarization is created by the incident wave in the medium. In the case of dielectric media this relation is expressed by the equation (2.2).

$$\vec{P} = \epsilon_0 \underline{\chi} \vec{E} \quad (2.2)$$

$$\vec{D} = \epsilon_0 \vec{E} + \vec{P} \quad (2.3)$$

The term  $\underline{\chi}$  is called the susceptibility tensor. Inserting the equation (2.2) into the constitutive relation equation (2.3) valid for dielectric media, the latter equation can be simplified:

$$\vec{D} = \epsilon_0 (\underline{1} + \underline{\chi}) \vec{E} \quad (2.4)$$

The well-known equation (2.5) is found by defining the dielectric permeability  $\underline{\epsilon}_r = \underline{1} + \underline{\chi}$ .

$$\vec{D} = \epsilon_0 \underline{\epsilon}_r \vec{E} \quad (2.5)$$

It is possible to prove, considering the Poynting hypothesis, that the values of the permeability tensor respect the condition  $\epsilon_{ij}^* = \epsilon_{ji}$ , with  $i$  and  $j$  integer 1, 2 and 3 and the star corresponding to the complex conjugate. This induces that the tensor  $\epsilon_r$  is a Hermitian matrix. One of the properties of such a matrix is to be symmetric.

The general case of the  $\epsilon_r$  matrix is written in the following form:

$$\epsilon_r = \begin{bmatrix} \epsilon_{11} & \epsilon_{12} & \epsilon_{13} \\ \epsilon_{12} & \epsilon_{22} & \epsilon_{23} \\ \epsilon_{13} & \epsilon_{23} & \epsilon_{33} \end{bmatrix} \quad (2.6)$$

As it is a Hermitian matrix, it is possible to diagonalize it. That means it exists a base  $X, Y, Z$  in which the matrix can be written as following:

$$\epsilon_r = \begin{bmatrix} \epsilon_x & 0 & 0 \\ 0 & \epsilon_y & 0 \\ 0 & 0 & \epsilon_z \end{bmatrix} = \begin{bmatrix} n_x^2 & 0 & 0 \\ 0 & n_y^2 & 0 \\ 0 & 0 & n_z^2 \end{bmatrix} \quad (2.7)$$

The  $n_i$  ( $i = x, y, z$ ) correspond to the main refractive indices of the medium. This is the main characteristic of an optical medium.

### 2.2.2 Crystallographic symmetry

The number of refractive indices of a crystal depends on the crystallographic symmetry. A discussion of the seven crystallographic systems linked to the optical properties is performed in the following.

The crystallographic symmetry depends on the crystallographic frame parameters of the crystal. Figure 2.5 represents the crystallographic frame  $\{\mathbf{a}, \mathbf{b}, \mathbf{c}\}$  with arbitrary length and angle. The parameters of this frame depend on the material symmetry. The seven crystallographic frames were described in Table 2.1 with their 'optical class'.

The isotropic crystals have the highest symmetry level. It results from those symmetries that the refractive index is the same for every direction inside the crystal.

For lower symmetry crystals, two different refractive indices are observed. Each one corresponds to one eigen polarization state. These property differences are directly linked to the crystallographic symmetry. Indeed, the symmetry will affect the dielectric tensor ((2.6)) components.

This thesis being mainly devoted to monoclinic crystals, the symmetry impact on the dielectric tensor will be derived from such system.

The monoclinic-prismatic system has a two-fold rotation symmetry around the  $\mathbf{b}$ -axis. All the optical properties depend on this symmetry. These crystals exhibit also a mirror symmetry plane perpendicular to the rotation axis.

We will not go into the detailed symmetry properties by describing all the crystallographic point and space group symmetries since they do not induce any change of the optical properties.

#### Application to the monoclinic system

The dielectric tensor of a monoclinic crystal is derived in this section.

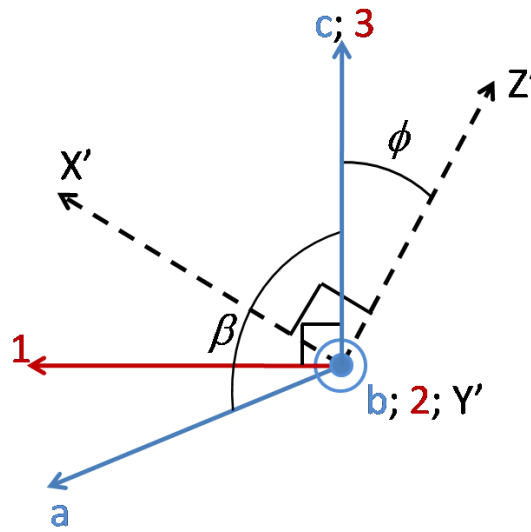


Figure 2.5 – Schematic of the different frames used; the crystallographic frame  $\{a, b, c\}$ , the main dielectric frame  $\{X', Y', Z'\}$  and the orthogonal frame  $\{\hat{1}, \hat{2}, \hat{3}\}$ .

Using the crystallographic frame  $\{a, b, c\}$  of a monoclinic system and assuming the direct orthogonal frame  $\{\hat{1}, \hat{2}, \hat{3}\}$  with the orientation  $\hat{2}$  being collinear with the crystallographic  $b$ -axis, the general dielectric tensor is the same than in equation (2.6).

The dielectric tensor  $\epsilon_r$  is affected by the symmetry of the crystal. This tensor can be rewritten by applying the crystal symmetry operator  $R$ . It results another dielectric tensor  $\epsilon'_r$  which should be equal to the previous one since the symmetry leads to have the same crystallographic arrangement and so the same propagation properties.

The equation (2.8) gives the relation between both of those dielectric frames:

$$\epsilon'_r = R\epsilon_r R^{-1} \quad (2.8)$$

In the case of monoclinic crystals the symmetry operator  $R$  is a two-fold rotation symmetry around the crystallographic  $b$ -axis. In the frame  $\{\hat{1}, \hat{2}, \hat{3}\}$ , this corresponds to a rotation of an angle  $\pi$  around the orientation  $\hat{2}$ . The  $R$  operator is then a simple rotation matrix given in equation (2.9) (In this particular case  $R=R^{-1}$ ).

$$R = \begin{bmatrix} \cos \pi & 0 & -\sin \pi \\ 0 & 1 & 0 \\ \sin \pi & 0 & \cos \pi \end{bmatrix} = \begin{bmatrix} -1 & 0 & 0 \\ 0 & 1 & 0 \\ 0 & 0 & -1 \end{bmatrix} \quad (2.9)$$

Inserted in equation (2.8), with  $\epsilon'_r = \epsilon_r$ , the new equation (2.10) is set.

$$\begin{bmatrix} \epsilon_{11} & \epsilon_{12} & \epsilon_{13} \\ \epsilon_{12} & \epsilon_{22} & \epsilon_{23} \\ \epsilon_{13} & \epsilon_{23} & \epsilon_{33} \end{bmatrix} = \begin{bmatrix} -1 & 0 & 0 \\ 0 & 1 & 0 \\ 0 & 0 & -1 \end{bmatrix} \begin{bmatrix} \epsilon_{11} & \epsilon_{12} & \epsilon_{13} \\ \epsilon_{12} & \epsilon_{22} & \epsilon_{23} \\ \epsilon_{13} & \epsilon_{23} & \epsilon_{33} \end{bmatrix} \begin{bmatrix} -1 & 0 & 0 \\ 0 & 1 & 0 \\ 0 & 0 & -1 \end{bmatrix} = \begin{bmatrix} \epsilon_{11} & -\epsilon_{12} & \epsilon_{13} \\ -\epsilon_{12} & \epsilon_{22} & -\epsilon_{23} \\ \epsilon_{13} & -\epsilon_{23} & \epsilon_{33} \end{bmatrix} \quad (2.10)$$

The only way to fulfil the equation (2.10) is to set  $\epsilon_{12} = \epsilon_{23}$  to 0. The dielectric tensor of a monoclinic crystal becomes :

$$\epsilon_r = \begin{bmatrix} \epsilon_{11} & 0 & \epsilon_{13} \\ 0 & \epsilon_{22} & 0 \\ \epsilon_{13} & 0 & \epsilon_{33} \end{bmatrix} \quad (2.11)$$

The equation (2.11) is the general matrix for a monoclinic crystal for an orthogonal frame having the orientation  $\hat{\mathbf{z}}$  along the crystallographic axis  $\mathbf{b}$ .

The triclinic system does not have any symmetry. The general dielectric tensor does not have null terms. The orthorhombic system has an orthogonal crystallographic frame. The dielectric tensor is then directly diagonalized when using the crystallographic frame.

Uniaxial crystals (i.e. trigonal, tetragonal and hexagonal systems) are characterized by a rotational symmetry of  $\frac{\pi}{2}$  around one axis which lets the system invariant. This leads to have  $\epsilon_{11} = \epsilon_{22}$  if this rotation is around the axis  $\hat{\mathbf{z}}$ . It is important to note that in uniaxial crystals the optic axis coincides with one of the principal axes. The optic axis is then fixed and does not have any dispersion, in contrast to biaxial crystals.

The cubic system is the most simple to describe since an additional symmetry leads to have  $\epsilon_{11} = \epsilon_{33}$ . The propagation properties are then no more dependent on the orientation and are the same for every polarization state.

Table 2.3 summarizes all the different dielectric tensors for the different symmetry systems using an orthogonal frame matched, as far as it is possible, to the crystallographic frame.

## 2.3 MEASUREMENT OF THE REFRACTIVE INDICES - PRISM METHOD

The refractive indices are the first parameter to be measured in optical materials besides the absorption spectra. They are needed in order to describe

System	Dielectric tensor
Triclinic	$\begin{bmatrix} \epsilon_{11} & \epsilon_{12} & \epsilon_{13} \\ \epsilon_{12} & \epsilon_{22} & \epsilon_{23} \\ \epsilon_{13} & \epsilon_{23} & \epsilon_{33} \end{bmatrix}$
Monoclinic	$\begin{bmatrix} \epsilon_{11} & 0 & \epsilon_{13} \\ 0 & \epsilon_{22} & 0 \\ \epsilon_{13} & 0 & \epsilon_{33} \end{bmatrix}$
Orthorhombic	$\begin{bmatrix} \epsilon_{11} & 0 & 0 \\ 0 & \epsilon_{22} & 0 \\ 0 & 0 & \epsilon_{33} \end{bmatrix}$
Trigonal, Tetragonal, Hexagonal	$\begin{bmatrix} \epsilon_{11} & 0 & 0 \\ 0 & \epsilon_{11} & 0 \\ 0 & 0 & \epsilon_{33} \end{bmatrix}$
Cubic	$\begin{bmatrix} \epsilon_{11} & 0 & 0 \\ 0 & \epsilon_{11} & 0 \\ 0 & 0 & \epsilon_{11} \end{bmatrix}$

Table 2.3 – Dielectric tensor of the different systems for an orthogonal frame having an orthogonal frame matched, as far as is possible, to the crystallographic frame.

the propagation of light inside the medium. Furthermore, for non-linear media, they allow to calculate the orientation for non-linear conversion. The main method used to measure refractive indices in biaxial media is to use prisms. This method can be used to measure all refractive indices, also of low symmetry materials under certain conditions as described in the following. The precision of such measurements is typically on the order of  $10^{-3}$ . Other methods using interferometry allow relative measurements down to  $10^{-6}$ .

The refractive indices depend on the wavelength, the temperature and pressure. This dependency can be significant on the order of  $10^{-6}\text{K}^{-1}$ ,  $10^{-6}\text{nm}^{-1}$ . In isotropic media there is only one refractive index describing the material properties. Materials which exhibit anisotropy have properties depending on the polarization and the orientation. Uniaxial materials have two main refractive indices, whereas biaxial materials have three main refractive indices.

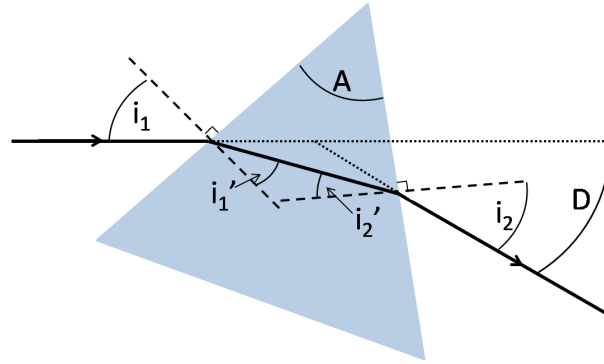


Figure 2.6 – Schematic of light propagation inside a prism with an angle  $A$ .

In this section, the prism method used to measure the refractive indices of biaxial materials is described in detail. The limitation of this measurement in case of biaxial media is also explained.

### 2.3.1 Description of the method

The refractive index measurement using the minimum deviation method (prism method), consists in the measurement of the angle of the light deviation through a prism of the measured material placed on a rotative plate. The prism is rotating until this angle reaches a minimum. Knowing the angle  $A$  of the cut of the prism, this angle measurement allows the calculation of the refractive index. This method is simple and robust. In fact, the minimum of deviation is easy to observe. However, in the case of a biaxial material precautions have to be taken in order to be sure of the measured values.

Figure 2.6 depicts the different angles of the minimum deviation method.

The Snell-Descartes law applied for a ray of light passing through the prism gives the equations 2.12 and 2.13, with  $n_{air}$  and  $n_{prism}$  the refractive indices of the air and the prism.  $i_1, i'_1$  the incident angles and  $i'_1, i_2$  the refraction angles.

$$n_{air} \sin(i_1) = n_{prism} \sin(i'_1) \quad (2.12)$$

$$n_{prism} \sin(i'_1) = n_{air} \sin(i_2) \quad (2.13)$$

The angle  $A$  of the prism is known, so the deviation angle  $D$  can be determined using the equation (2.14).

$$D = i_1 + i_2 - A \quad (2.14)$$

Knowing that  $A = i'_1 + i'_2$  and using equations (2.12) and (2.13) the deviation angle becomes :

$$D = i_1 + \arcsin \left[ \frac{n_{prism}}{n_{air}} \sin(A - \arcsin[\frac{n_{air}}{n_{prism}} \sin(i_1)]) \right] - A \quad (2.15)$$

The equation (2.16) comes from the simplification of the equation (2.15) using the small angles approximation.

$$D = A \left( \frac{n_{prism}}{n_{air}} - 1 \right) \quad (2.16)$$

On Figure 2.7 is presented the calculation of the deviation angle for prisms with different parameters  $A$ . The refractive index was set to 2. The minimum deviation angle increases with the angle  $A$ . The small angles approximation can be used only if the angle  $A$  is smaller than  $10^\circ$ . In this case the deviation angle does not change.

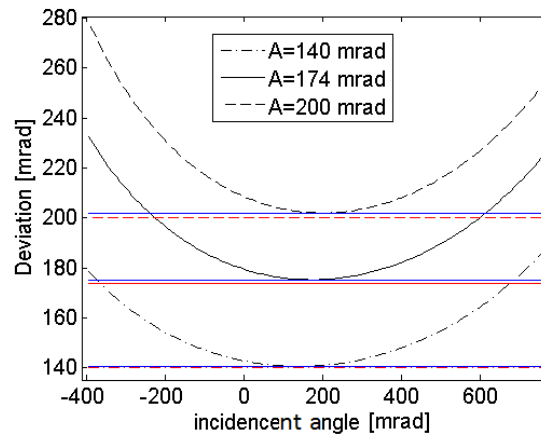


Figure 2.7 – Deviation angle as a function of the incident angle for a refractive index of 2. Black curves correspond to the complete equation 2.15 and red curves use the simplified equation 2.16. Blue curves are the minimum deviation calculated from 2.17.

In practice, the minimum angle deviation is measured to calculate the refractive index. The minimum deviation angle occurs when  $i'_1 = \frac{A}{2}$ , equation (2.17) is deduced. With a simple manipulation on this equation the refractive index of the prism can be calculated using the equation (2.18). In order to have a higher accuracy of the refractive index, the deviation angle has to be as high as possible. Usually, the angle  $A$  of the prisms are around  $40^\circ$ . The deviation angles with such an angle are higher than those on Figure 2.7.

$$D_{min} = A \left( \frac{n_{prism}}{n_{air}} - 1 \right) \quad (2.17)$$

$$n_{prism} = \frac{n_{air} \sin\left(\frac{A+D_{min}}{2}\right)}{\sin\left(\frac{A}{2}\right)} \quad (2.18)$$

The accuracy of the refractive index is determined by the measurement of the minimum deviation angle and the accuracy of the angle  $A$ . So, to be able to know the refractive index with an accuracy of  $10^{-4}$  the angle  $A$  should be known with an uncertainty of  $12''$  and  $D_{min}$  with  $0.6^\circ$  [18].

### 2.3.2 Case of biaxial media

#### General case

In the case of biaxial media, three main refractive indices allow the description of the wave surfaces of the crystal. They are represented by an ellipsoid having each refractive index ( $n_p, n_m, n_g$ ) on the axes of the orthogonal dielectric frame ( $X, Y, Z$ ). In the particular case of monoclinic crystals, one of the dielectric frame axes corresponds to the crystallographic  $\mathbf{b}$ -axis. Figure 2.5 depicts all different frames used for monoclinic crystals. The axes  $\mathbf{a}$ ,  $\mathbf{b}$  and  $\mathbf{c}$  represent the crystallographic axes with  $\mathbf{b} \perp (\mathbf{a}, \mathbf{c})$  and  $\beta$  the obtuse angle between  $\mathbf{a}$  and  $\mathbf{c}$ .

In order to measure the principal refractive indices, the light has to propagate along a principal direction of the dielectric frame.

Knowing only one of these dielectric orientations, the three refractive indices can not be directly measured.

However, only two prisms can be enough to measure the three main refractive indices. Considering the orthogonal frame (1, 2, 3) with  $2 \parallel \mathbf{b}$  and  $3 \parallel \mathbf{c}$ , depicted on Figure 2.5, the refractive indices for every propagation direction possible is described by the matrix (2.19).

$$\begin{bmatrix} 1 \\ \frac{1}{\epsilon_r'} \end{bmatrix} = \begin{bmatrix} n_{11}^{-2} & 0 & n_{13}^{-2} \\ 0 & n_{22}^{-2} & 0 \\ n_{13}^{-2} & 0 & n_{33}^{-2} \end{bmatrix} \quad (2.19)$$

As there are only four unknown values, only four measurements are necessary. That means only two prisms are sufficient to fill this matrix since on each prism two measurements corresponding to the two polarization eigen-states can be performed. This matrix (2.19) can be diagonalized. The new matrix resulting from such transformation describes the eigen dielectric frame ( $X', Y', Z'$ ). In monoclinic crystals the  $\mathbf{b}$ -axis corresponds to one of the dielectric axes, the diagonalized matrix (2.20) simply consists in rotation around this axis (here the axis 2).

$$\begin{bmatrix} 1 \\ \frac{1}{\varepsilon_r} \end{bmatrix} = \begin{bmatrix} n_1^{-2} & 0 & 0 \\ 0 & n_2^{-2} & 0 \\ 0 & 0 & n_3^{-2} \end{bmatrix} \quad (2.20)$$

In the case of monoclinic double tungstates this rotation corresponds to a counter-clockwise rotation around the axis 2 described by the equation (2.21). The transition between the two matrices can be done using the equation (2.22).

$$R_2 = \begin{bmatrix} \cos \phi & 0 & -\sin \phi \\ 0 & 1 & 0 \\ \sin \phi & 0 & \cos \phi \end{bmatrix} \quad (2.21)$$

$$\begin{bmatrix} 1 \\ \frac{1}{\varepsilon'_r} \end{bmatrix} = [R_2] \begin{bmatrix} 1 \\ \frac{1}{\varepsilon_r} \end{bmatrix} [R_2]^{-1} \quad (2.22)$$

In the following, it is considered that two prisms are cut with the axes 2 and 3 perpendicular to the bisectrix of the angle  $A$ , corresponding to the direction of the light propagation when the deviation angle is minimal. Thus, with the first prism, cut along the axis 2, the measurement with light polarized along  $[1, 0, 0]$  and  $[0, 0, 1]$  in the base  $(X', Y', Z')$  will provide the direct measurement of the refractive indices  $n_1$  and  $n_3$ .

The second crystal oriented along the axis 3 will provide the measurement of  $n_{22} = n_2$  and  $n_{13}$ . The latter is not an eigen value of the dielectric frame. However, knowing that it is only a rotation, the refractive indices can be deduced using the equation (2.23).

$$n^{-2} = \begin{pmatrix} 1 & 0 & 0 \end{pmatrix} \begin{bmatrix} n_{11}^{-2} & 0 & n_{13}^{-2} \\ 0 & n_{22}^{-2} & 0 \\ n_{13}^{-2} & 0 & n_{33}^{-2} \end{bmatrix} \begin{pmatrix} 1 \\ 0 \\ 0 \end{pmatrix} = n_{11}^{-2} = n_1^{-2} \cos^2 \phi - n_3^{-2} \sin^2 \phi \quad (2.23)$$

This fourth measurement gives information on the rotation of the ellipsoid around the  $\mathbf{b}$ -axis. The angle of the rotation  $\phi$  can be measured using equation (2.24) for a counter-clockwise rotation. This allows the measurement of the ellipsoid rotation around the  $\mathbf{b}$ -axis as a function of the wavelength.

$$\cos^2 \phi = \frac{n^{-2} + n_3^{-2}}{n_1^{-2} + n_3^{-2}} \quad (2.24)$$

With all those measurements, the 3 main refractive indices and the angle  $\phi$  can be known. In order to be general it is important to note that

the refractive indices  $n_p < n_m < n_g$  in the base (X, Y, Z), do not correspond to  $n_1, n_2, n_3$ , respectively. In fact, the order of the refractive indices can be known only after the measurement of the monoclinic crystal.

### Monoclinic Double tungstates and measurement accuracy

In the particular case of the monoclinic double tungstates (KGdW, KYW, KLuW) some refractive index measurements have already been performed. The ellipsoid orientation is known. The X axis corresponding to the refractive index  $n_p$  is parallel to the crystallographic **b**-axis. The angle  $\phi$  is around  $17^\circ$  to  $21,5^\circ$  [13, 19].

On the basis of those measurements, the error on the refractive index values as a function of the misalignment between the crystal cut and the dielectric frame is described. Figure 2.8 shows the error on the measurement as a function of the misalignment using the equation (2.25).

$$\epsilon_{n_g} \simeq -\frac{1}{2}\epsilon_{cut}n_g^3n_p^{-2} \quad (2.25)$$

with  $\epsilon_{cut}$  the maximal cut error in order to have an error  $\epsilon_n$  on the refractive index value.

This equation is expressing the refractive index  $n_g$  since this angle is the most sensitive to the cut error. In fact, the  $n_m$  refractive index is described by a circle, so it is not sensitive to any misalignment, and for the  $n_p$  refractive indices the radius of curvature of the surface is flatter than the one for the  $n_g$  refractive index.

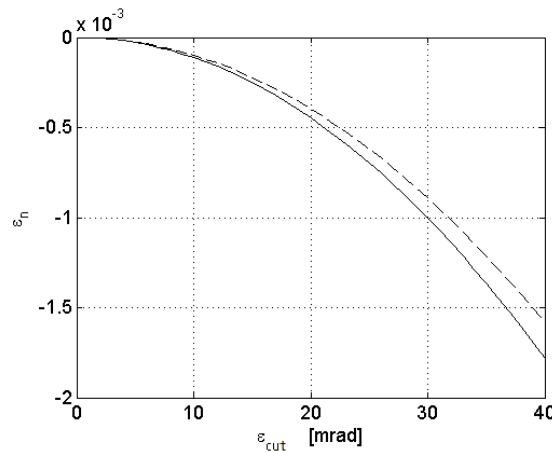


Figure 2.8 – Error on the measurement of the refractive index as a function of the cutting error; full line: for the measurement of  $n_g$ ; dashed line : on the measurement of  $n_p$  in KGdW at  $1.06 \mu\text{m}$ .

Equation 2.25 is obtained for a cutting error of the crystal corresponding to an angle of misalignment  $\epsilon_{cut}$  with respect to the X axis in the (X,

Z) plane. This error is small. We have  $\epsilon_{cut} \approx \sin \epsilon_{cut}$ . Thus using the same method than in the previous section 2.3.2, the incident polarization vector becomes  $[\epsilon_{cut}, 0, 1]$ . The cutting error is given by equation (2.26).

$$n^{-2} = \begin{pmatrix} \epsilon_{cut} & 0 & 1 \end{pmatrix} \begin{bmatrix} 1 \\ \epsilon_r \end{bmatrix} \begin{pmatrix} \epsilon_{cut} \\ 0 \\ 1 \end{pmatrix} = \epsilon_{cut}^2 n_p^{-2} + n_g^{-2} \quad (2.26)$$

Using a limited development of the first order, we obtain condition (2.25) with  $\epsilon_{n_g}$  being the maximal error tolerance. It results that in order to have an accuracy of  $10^{-3}$  the cutting angle error has to be less than 30 mrad. 9.5 mrad corresponding to an accuracy of  $10^{-4}$ .

### 2.3.3 Discussion

The measurement of the refractive index in monoclinic crystals is not an easy task. The precision of the cutting angle of the crystal is important if a high accuracy is required. Of course, in practice one needs to know the uncertainty of the angle measurement in order to obtain the total error. Furthermore, the prisms are often cut with the measured refractive index axis perpendicular to one of the prism facets and the angle measured is not the minimum deviation angle. However, this leads to the same error inserted by the cutting error.

The measurements of the refractive indices cited in publication [13] have been realized using three prisms cut along the dielectric axis. The orientations used are the same for all wavelengths. However, it is known that the dielectric frame may rotate [20]. So the refractive index measurements can not be performed for different wavelengths with the same accuracy. An error is added due to the crystal cut and the ellipsoid rotation. This measurement can not give an accuracy better than  $5 \times 10^{-3}$ , which is not sufficient in order to predict the optical axis dispersion.

In the publication [21], there is another problem. The crystal cut orientations are confused. It seems that the measurements were performed in the same way than in the publication [13].

It exists some other publications where the refractive indices of monoclinic double tungstates are given [19, 22] with probably the same method. The values published in the two last articles are, from the experience gained within this thesis, the ones that predict the orientation of the optic axis with the best accuracy (within  $1^\circ$ ).

## 2.4 OPTICAL PROPERTIES

In this section the optical properties of the KREW are given. The basic properties of the crystal used in the experiments are provided. The refractive index is taken from literature as well as the absorption and emission properties in case of the Holmium-doped KYW and Neodymium-doped KGW crystals.

### 2.4.1 Refractive indices

The refractive index is the most important parameter needed to describe the light propagation inside a medium. In case of the monoclinic double tungstate, in the previous section it has been demonstrated that due to the symmetry of these crystals one needs to have three different refractive indices in order to describe all the possible orientations. In the next chapter, the conical refraction effect which is strongly sensitive to the refractive index will be discussed. In fact, to be able to predict the orientation of the optic axis within  $\pm 0.2^\circ$  the refractive indices have to be known with an accuracy on the order of  $10^{-4}$ . Unfortunately, as it has been discussed in the previous section, most of the measurements are not accurate enough to well predict the orientation of the optic axis, especially around  $2 \mu\text{m}$ .

In the precedent section a thorough description of the refractive index measurement shows the difficulty to obtain good refractive index measurements available for a wide wavelength range. In fact, the rotation of the ellipsoid with the wavelength is never taken into account. This leads to an error and thus to a higher inaccuracy of the refractive index measurement for wavelengths far away from the wavelength used to measure the dielectric frame orientation (mainly 633 nm and 1064 nm).

#### Literature reviews

The refractive index values available in literature for the monoclinic double tungstates will be first described. Those refractive index measurements are always linked to a dielectric frame. In the case of monoclinic double tungstates the dielectric frame is fixed by the value of the angle  $\phi_c$  between the crystallographic c-axis and the  $N_g$  axis of the dielectric frame. The Sellmeier equations used in literature differ to authors. It exists three types of equations with two of them which are very similar. The parameters of those different equations are listed in Table 2.4 with their Sellmeier equations given below the crystal name in the table.

Crystal		$A_i$	$B_i$	$C_i$ [nm]	$D_i$ [ $\times 10^{-9} \text{nm}^{-2}$ ]	Range [ $\mu\text{m}$ ]	$\phi_c$ [ $^\circ$ ]	Ref.
KGW:Er <sup>3+</sup> (2.27)	$n_g$	1.3867	0.6573	170.02	0.2913	0.4–1.5	21.5 $\pm$ 1	[13]
	$n_m$	1.5437	0.4541	188.91	2.1567			
	$n_p$	1.5344	0.4360	186.18	2.0999			
KGW:Nd <sup>3+</sup> (2.27)	$n_g$	1.28065	0.75436	159.499	1.94	0.44–0.64	-	[21]
	$n_m$	1.04111	0.95487	140.9584	0.5			
	$n_p$	1.08690	0.88137	140.2105	0.6			
Crystal		$A_i$	$B_i$	$C_i$ [ $\mu\text{m}$ ]	$D_i$ [ $\times 10^{39} \mu\text{m}^{-2}$ ]	Range [ $\mu\text{m}$ ]	$\phi_c$ [ $^\circ$ ]	Ref.
KYW (2.28)	$n_g$	3.55544	0.46438	0.15213	-34.08	0.45–1.5	18.5	[17]
	$n_m$	3.57271	0.30991	0.17484	-34.01			
	$n_p$	3.50441	0.24431	0.18268	-30.22			
KYW (2.28)	$n_g$	2.39921	1.75636	0.20075	13.263	0.45–1.5	18.5	[22]
	$n_m$	2.52932	1.46328	0.20629	20.927			
	$n_p$	2.69161	1.15780	0.21270	18.815			
Crystal		$A_i$	$B_i$			Range [ $\mu\text{m}$ ]	$\phi_c$ [ $^\circ$ ]	Ref.
KYW (2.29)	$n_g$	3.1278346	0.161512			0.4–1	17.5 $\pm$ 0.5	[19]
	$n_m$	2.9568303	0.1591855					
	$n_p$	2.8124935	0.1529056					

Table 2.4 – Sellmeier parameters of KREW from literature.

$$n_i = A_i + \frac{B_i}{1 - \left(\frac{C_i}{\lambda}\right)^2} - D_i \lambda^2 \quad (2.27)$$

$$n_i^2 = A_i + \frac{B_i}{1 - \left(\frac{C_i}{\lambda}\right)^2} - D_i \lambda^2 \quad (2.28)$$

$$n_i^2 - 1 = \frac{A_i \lambda^2}{\lambda - B_i^2} \quad (2.29)$$

The Sellmeier equations are very useful to describe the dispersion of the refractive indices. However, as it is not easy to compare the different values obtained in the literature by simply reading those parameters, the different values of the refractive indices are represented on Figure 2.9.

The difference between each publication is significant. The main issue is often the small number of points used to perform the Sellmeier fits. This reduces drastically the accuracy of the refractive indices and does not allow to extend the range too far from the last measurement point. The measurements provided by [19, 22] are accurate enough in order to predict the orientation of the optic axis with an uncertainty of 1 $^\circ$ .

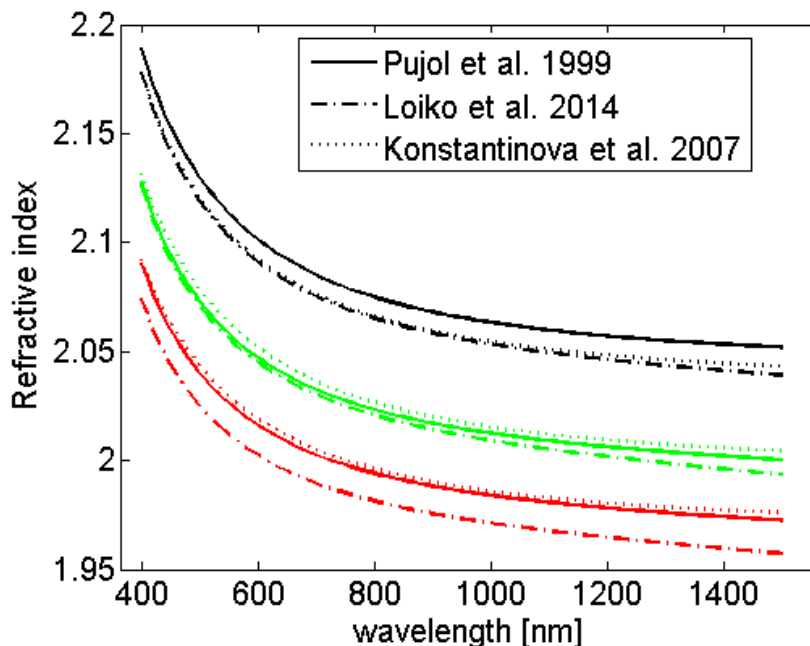


Figure 2.9 – Dispersion of the refractive indices of KREW taken from several references.  $N_g$  (black),  $N_m$  (green),  $N_p$  (red).

#### 2.4.2 Absorption/Emission along the dielectric axes

In this section the absorption spectra available in literature will be given additionally. The different KREW matrices are represented. However, due to similar crystal fields the absorption does not differ from one matrix to another one when the doping ion is the same.

##### Holmium-doped KREW

The absorption, for all experiments in this thesis, is given for the  $^5I_8 \rightarrow ^5I_7$  transition around  $2 \mu\text{m}$ . The emission is also between those two energy levels  $^5I_7 \rightarrow ^5I_8$  for  $2 \mu\text{m}$  radiation. The  $\text{Ho}^{3+}$  ion can also be used at the  $^5I_6 \rightarrow ^5I_7$  transition for light emission around  $3 \mu\text{m}$ . The complete energy diagram of Holmium in KGW is depicted on Figure 2.10.

The absorption suffers from the same complexity like the other parameters in KREW, leading to unclear results obtained in some publications. In the next paragraph, a small description of the classical measurement performed in order to obtain the absorption of this crystal will be given. This will facilitate the interpretation of the results published by other groups.

The measurement of the absorption is always performed along the main directions of the dielectric frame. It has already been discussed in

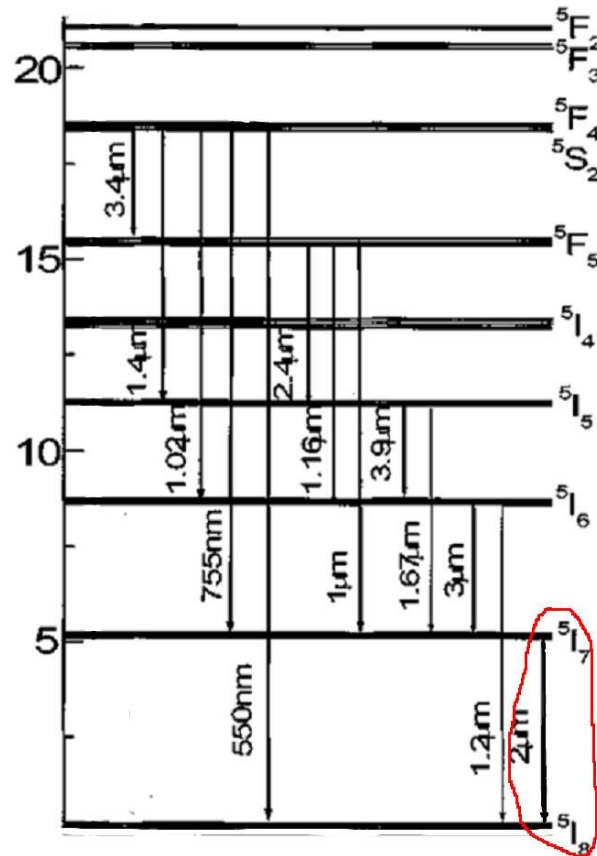


Figure 2.10 – Energy diagram of Holmium in KGW, taken from [23]. The energy is in  $10^3\text{cm}^{-1}$ .

the previous section that these directions may differ from one publication to another. This can cause slight differences in the measurements. However, there is one well-known orientation of the KREW, the  $N_p$  axis of the dielectric frame which is along the  $\mathbf{b}$ -crystallographic axis. In such an orientation the polarization spectra,  $E\|N_m$  and  $E\|N_g$  can be measured. In order to measure the absorption in the polarisation  $E\|N_p$ , another measurement is often performed with a crystal cut perpendicularly to  $N_g$ . Then the measurement of  $E\|N_m$  can be performed once more and should be the same than the one performed along the  $N_p$  cut crystal. The measurements in literature provide at maximum those three spectra,  $E\|N_p$ ,  $E\|N_m$  and  $E\|N_g$ . Of course, those measurements are enough for most of the applications. However, as it will be discussed in the next section, it has been proven that the eigen-frame of the absorption may differ from the dielectric frame [24]. In that case a fourth measurement is needed if one wants to fully describe the absorption in such crystals.

Nevertheless, in this section the measurements available from literature are reported in case of Holmium-doped-KREW. There is no spec-

transcopic difference between the KLuW, KYW and KGW when they are doped with the same ion [25]. On Figure 2.11, one can observe the typical absorption cross section of Holmium-doped KREW. The higher absorption cross section is always for the polarization  $E \parallel N_m$ . The lower one is the  $E \parallel N_g$  and therefore is often not reported. This is true even for other doping ions [26]. The maximum absorption peak occurs at 1960 nm for all Holmium-doped KREW. Under  $E \parallel N_m$  polarization the absorption cross section is estimated to be around  $1.5 \times 10^{-20} \text{ cm}^2$  [27]. This wavelength is the pumping wavelength used in the laser experiments in Chapter 5.

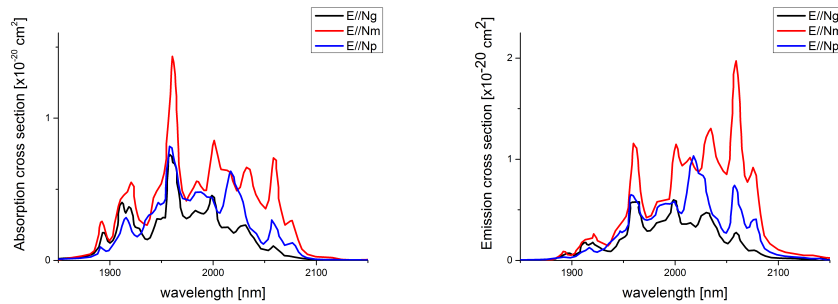


Figure 2.11 – Absorption (on the left) and emission (on the right) cross section of Holmium-doped KLuW, from [28].

### Neodymium-doped KREW

Since few experiments have been carried out with Neodymium ions as dopant, we succinctly provide here the absorption cross section of those ions in KREW. The behaviour is the same as described in the previous paragraph. The maximum absorption is for the  $E \parallel N_m$  and occurs around 810 nm. The absorption cross section is then around  $25 \times 10^{-20} \text{ cm}^2$  [29]. This is a very strong absorption line. The absorption transition moves the electron from the  $^4I_{9/2}$  to the  $^4F_{5/2}$  and allows lasing at 1067 nm [30]. In practice this wavelength is not used there to pump this crystal since the absorption is far too high. This is discussed in more detail in Chapter 5.

#### 2.4.3 Absorption along the optic axis

The absorption is typically measured along the main orientations of the dielectric frame. However, those orientations do not correspond to the optic axis. So, the question is, if it is possible to predict the absorption along the optic axis of a monoclinic double tungstate. The answer is, of course, yes. In this section, the simple model used to describe the absorption along the optic axis is described. Some equations are added in

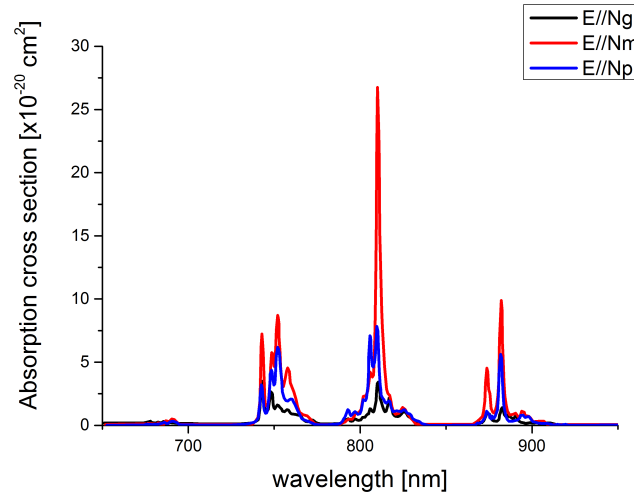


Figure 2.12 – Absorption cross section of Neodymium-doped KGW, from [29].

order to take into account the different polarization states near the optic axis.

### Model

In order to fully understand the measurements shown at the end of this section, we carried out some simulations. Considering the dielectric frame  $(X, Y, Z)$ , with  $n_x < n_y < n_z$ , the monoclinic axis is along the  $X$  axis (also labeled  $N_p$ ) of the dielectric frame in these double tungstate crystals [31]. Consequently, optical properties are free to rotate around this axis [32]. Therefore, the monoclinic specificity does not affect the angular distributions of absorption at the vicinity of the dielectric plane  $(X, Z)$  that contains the optic axes. Thus, the properties around these axes can locally be approximated as an orthorhombic biaxial distribution. In this case, the well-known double-layer surface of refractive indices [33] can be extended to complex optical indices, by introducing complex optical indices  $\bar{n}_j = n_j + i\kappa_j$ ,  $j=x, y, z$  in the dielectric frame, assuming the weak absorption hypothesis with  $\kappa_j \ll n_j$  [34]. Such an approach allows the analytical calculation of the refractive indices and absorption coefficients, from Equation (2.30).

$$\bar{n}^{\pm}(\theta, \phi) = \left[ \frac{2}{-\bar{B} \mp \sqrt{\bar{B}^2 - 4\bar{C}}} \right]^{1/2} \quad (2.30)$$

with  $\bar{B} = -u_x^2(\bar{n}_y^{-2} + \bar{n}_z^{-2}) - u_y^2(\bar{n}_x^{-2} + \bar{n}_z^{-2}) - u_z^2(\bar{n}_x^{-2} + \bar{n}_y^{-2})$ ,  $\bar{C} = u_x^2\bar{n}_y^{-2}\bar{n}_z^{-2} + u_y^2\bar{n}_x^{-2}\bar{n}_z^{-2} + u_z^2\bar{n}_x^{-2}\bar{n}_y^{-2}$  and  $u_x, u_y, u_z$  express the propagation

directions in spherical coordinates :  $u_x = \cos(\phi)\sin(\theta)$ ,  $u_y = \sin(\phi)\sin(\theta)$ ,  $u_z = \cos(\theta)$ , with  $\theta$  and  $\phi$  the spherical angles in the dielectric frame.

### Numerical simulation

For all the following simulations, the values given in Equation (2.31) have been used. This matrix representation of the complex optical index is given for the pump wavelength of  $1.96 \mu\text{m}$ . The  $\kappa_{xx}$  value comes from the polarized absorption measurement along the  $Z(N_g)$  axis for  $E//X(N_p)$ . The  $\kappa_{yy}$  is the mean between the polarized absorption measurement along the  $Z(N_g)$  axis for  $E//Y(N_m)$  and the one measured near the optic axis with the same polarization state.  $\kappa_{xx}$  and  $\kappa_{yy}$  are given with an uncertainty of  $0.2 \times 10^{-5} (\approx 0.1 \text{ cm}^{-1})$ . The  $\kappa_{zz}$  has not been directly measured. It has been adjusted in order to better fit the polarized absorption measurement point near the optic axis for the  $E \perp Y(N_m)$  polarization state. It results a higher uncertainty estimated at  $0.4 \times 10^{-5} (\approx 0.2 \text{ cm}^{-1})$ .

It has been proven by [24] that the eigen-frame of the imaginary part of the optical indices might not match with the one of the real part. This results in non-diagonal terms in the imaginary part of the matrix representation of the complex optical index. In the monoclinic  $\text{YCa}_4\text{O}(\text{BO}_3)_3$  (YCOB) crystal the non-diagonal terms are  $\kappa_{xz} = \kappa_{zx}$ , due to the fact that the plane of mirror symmetry corresponds to the dielectric plane that contains the optic axes  $(X,Z)$ , leading the  $Y$ -axis to be parallel to the monoclinic axis. In the case of KYW, it is the  $X$ -axis that is perpendicular to this mirror symmetry plane, so that  $\kappa_{yz} = \kappa_{zy}$  might be different from zero. In this case the solution of the imaginary part of  $\bar{n}^+$  in the  $YZ$ -plane in Figure 2.13 is expected to rotate around the  $X$ -axis, depending on such non-diagonal value. Since the measurements performed here are close to the  $XZ$ -plane (where the evolution of  $\bar{n}^\pm$  remains unchanged even if considering non-zero non-diagonal terms),  $\kappa_{yz}$  has been set to 0 in the following numerical simulations.

$$\bar{n} = \begin{pmatrix} 1.957 & 0 & 0 \\ 0 & 1.994 & 0 \\ 0 & 0 & 2.035 \end{pmatrix} + i \begin{pmatrix} 0.9 & 0 & 0 \\ 0 & 2.2 & \kappa_{yz} \\ 0 & \kappa_{zy} & 0.6 \end{pmatrix} \times 10^{-5} \quad (2.31)$$

Note that the relation between the imaginary part of the complex optical index and the linear absorption coefficient in  $\text{cm}^{-1}$  is  $\alpha = \frac{4\pi\kappa}{\lambda}$  (with  $\lambda$  corresponding to the wavelength in vacuum).

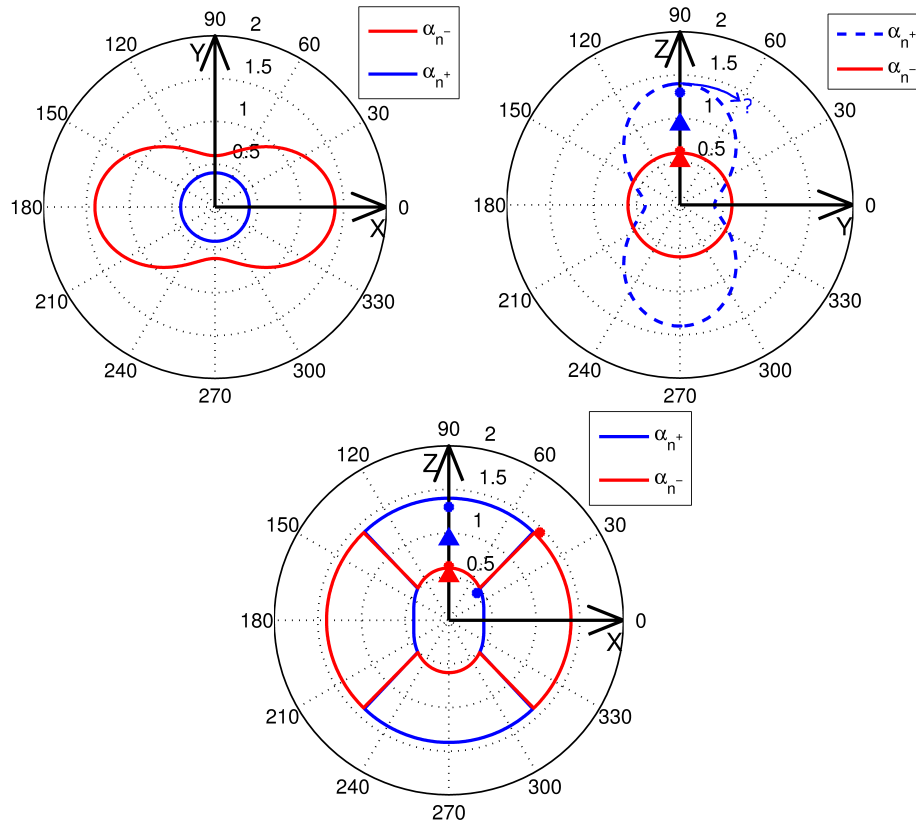


Figure 2.13 – Evolution of absorption coefficients in  $\text{cm}^{-1}$  for the principal dielectric plane of the Holmium-doped KYW(1%at.) crystal. Dots are measurement points of a Holmium-doped KYW crystal and triangles taken from Holmium-doped KLuW [28]. Note that the relative orientation of the bilobar distribution in the  $(Y,Z)$  plane is still to be determined, since  $\kappa_{yz}$  is not measured yet, which does not affect our study along the optic axes.

On Figure 2.14 are drawn the imaginary part of  $\bar{n}^{\pm}$  with the coordinates  $\Delta\theta = 0$  and  $\Delta\phi = 0$  corresponding to the optic axis. The angle  $\Delta\theta$  varies in the  $XZ$ -plane when the angle  $\Delta\phi$  is equal to zero. Figure 2.14 shows the discontinuity of the imaginary part of  $\bar{n}^{\pm}$  along the optic axis. The numerical simulations are performed by depicting internal and external layers of the imaginary index surface.

In order to take into account the polarization we introduce a new set of equations, valid only at the vicinity of the optic axis :

$$\begin{aligned}\bar{n}^{E\perp N_m} &= \bar{n}^+ \cos^2\left(\frac{\iota}{2}\right) + \bar{n}^- \sin^2\left(\frac{\iota}{2}\right) \\ \bar{n}^{E\parallel N_m} &= \bar{n}^+ \sin^2\left(\frac{\iota}{2}\right) + \bar{n}^- \cos^2\left(\frac{\iota}{2}\right)\end{aligned}\quad (2.32)$$

with the function  $\sin^2(\frac{\iota}{2})$  drawn on Figure 2.15. The parameter  $\iota$  simply consists in the angle between the  $XZ$ -plane and the direction of wave propagation, which can vary from 0 to  $2\pi$  while considering the optic axis as the origin. This approach, in agreement with our experimental observa-

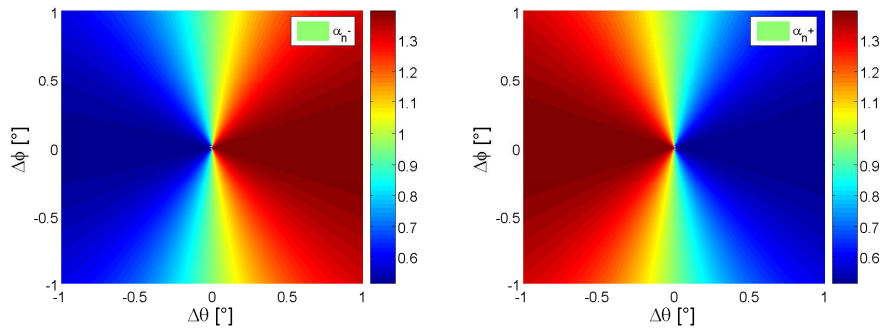


Figure 2.14 – Simulated absorption profiles in  $\text{cm}^{-1}$  corresponding to the imaginary part of  $\bar{n}^{\pm}$  near the optic axis of Holmium-doped KYW(1%at.) with a numerical resolution of 0.1 mrad.

tions as will be shown in Chapter 4, continuously extends the polarization distribution for propagation at the optic axis to those at the vicinity of such optical singularity. Those equations express the fact that on Figure 2.13, in the XZ-plane, the section of the external layer of the imaginary part corresponds to  $E \parallel N_m$ . They represent the contribution of each polarization eigen state. The imaginary part gives the absorption coefficient for one specific polarization. In the case of the real part, those sums do not give a relevant information, but only a weighted average of the refractive index value.

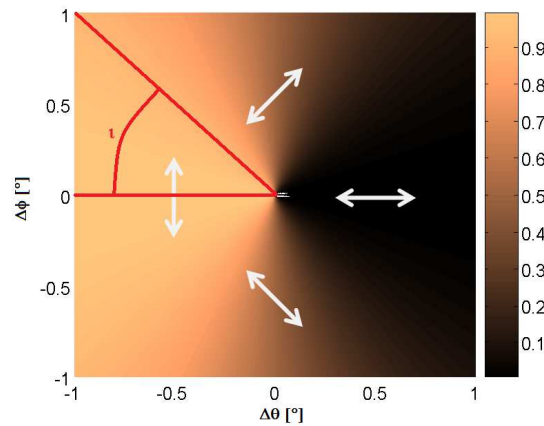


Figure 2.15 – Variation of the value  $\sin^2(\frac{\theta}{2})$  near the optic axis. The arrows show the incident polarization to obtain only one refracted spot.

The computation of Equation (2.32) is given on Figure 2.16. A good agreement with the measurements performed at ISL (see Figure 4.9 in Chapter 4) is obtained using the values given in Equation (2.31). The evolution of the absorption is identical on both, measurements and numerical simulations.

Those calculations give a thorough understanding of the absorption at

the vicinity of the optic axis. It results that the absorption properties must be the same for both optic axes since they lie in the XZ-plane perpendicular to the mirror plane of the monoclinic symmetry. It is important to note that all those simulations are only valid for the wavelength of  $1.96 \mu\text{m}$ . Indeed, the shape of the absorption profile will completely change for another resonant wavelength since the maxima and minima of absorption for each wavelength along the dielectric axes are different [32].

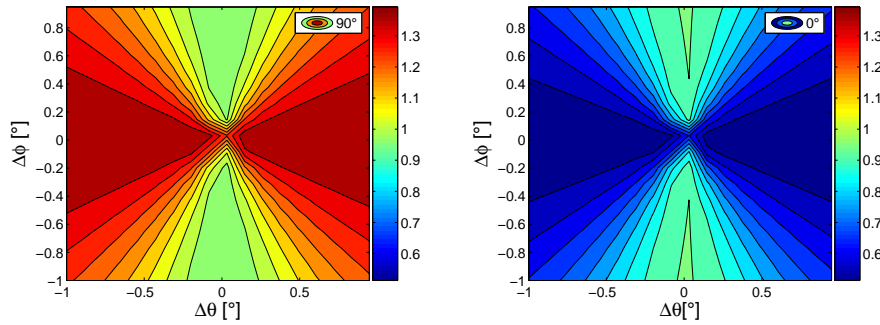


Figure 2.16 – Simulated absorption profiles in  $\text{cm}^{-1}$  near the optic axis of Holmium-doped KYW(1%at.) with a resolution of 2 mrad (corresponding to our measurements at the vicinity of the optic axis).  $90^\circ$  and  $0^\circ$  correspond to  $E \parallel N_m$  and  $E \perp N_m$ , respectively.

Using the same equations it is possible to deduce the emission cross sections near the optic axis. In Figure 2.17 the emission cross section profiles corresponding to the maximum emission line near 2076 nm of Holmium-doped KLuW are shown (value taken from [28]). The profiles for both polarizations are similar with the absorption profiles. The measurement of the emission cross sections along the optic axis can not be easily performed. Those simulations are the only way to estimate the values of emission cross sections near the optic axis.

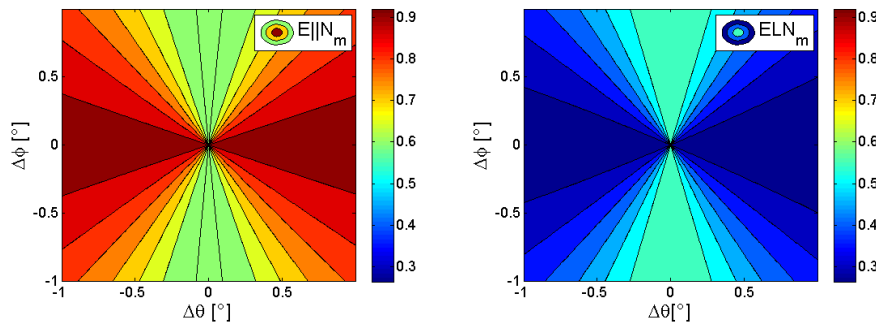


Figure 2.17 – Simulated emission cross section in  $\times 10^{-20} \text{cm}^2$  near the optic axis of Holmium-doped KLuW.

## 2.5 THERMAL PROPERTIES

This section is devoted to the thermal properties of the monoclinic double tungstate crystals. As all those properties also depend on the orientation it is very delicate to determine the 'true' value for one specific orientation. Furthermore, the different values obtained in literature add some confusion. For some of those parameters even the measurement methods used are unclear. The reader should be aware that as for the refractive indices is it very difficult to predict the value of those parameters. However, it is possible to get an order of magnitude of those parameters. This is enough to compare those materials with other ones, or along different orientations.

### 2.5.1 Thermal conductivity

In Table 2.5 all parameters of the thermal conductivity for the KREW are listed. For information, the dependency of the thermal conductivity with respect to the temperature is given in Figure 2.18. In this Figure, the monoclinic double tungstate crystals have the same behavior than most of the laser crystals. The thermal conductivity increases for lower temperature. That means more heat can be removed at lower temperature. In practice, this is not interesting for laser setups which should be able to work at room temperature.

Crystal	system	a	b	c	Ref.
KGW	I <sub>2</sub> /a	2.6	3.8	3.4	[7]
KGW	C <sub>2</sub> /c	-	2.6	3.4	[35]
KYW	C <sub>2</sub> /c	-	2.7	-	[35]
KLuW	C <sub>2</sub> /c	3.06	2.36	3.9	[36]

Table 2.5 – Thermal conductivity of monoclinic double tungstates along the crystallographic axis in  $W.m^{-1}.K^{-1}$ .

### 2.5.2 Thermal expansion

Under heating, the crystal will tend to expand. This changes the lattice parameter. The thermal expansion coefficient  $\alpha_T$  can be expressed in a similar way like the optical properties of the refractive indices. In the general case it is represented by a matrix (2.33). The thermal expansion is expressed in  $K^{-1}$ .

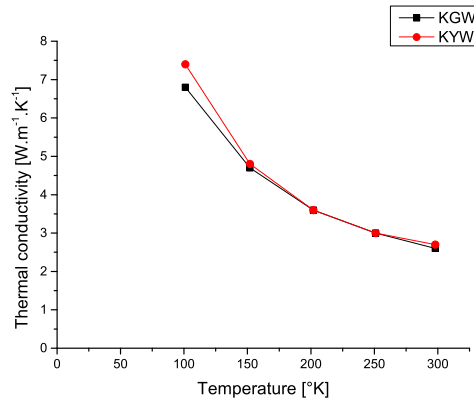


Figure 2.18 – Thermal conductivity vs temperature along the b-axis, from [35].

$$\alpha_T = \begin{bmatrix} \alpha_{11} & \alpha_{12} & \alpha_{13} \\ \alpha_{12} & \alpha_{22} & \alpha_{23} \\ \alpha_{13} & \alpha_{23} & \alpha_{33} \end{bmatrix} \quad (2.33)$$

### 2.5.3 Temperature dependence of the refractive index

The modification of the temperature influences also the refractive index of a crystal. It is a parameter called  $\frac{dn}{dT}$ . This parameter has only taken into account the temperature elevation inside the crystal. As it will be described later the measurement of this parameter has to be performed with a crystal free to expand. Otherwise the refractive index change will also have a contribution to the stress inside the medium.

The measurements of this parameter in monoclinic double tungstates have been widely studied. However, the difficulty to measure accurately this value and to be sure of the different contributions leads to a wide spreading of the results given in literature about those parameters.

The different methods used to measure this parameter are quickly described.

The first method consists in simply measuring the refractive index of the material at different temperatures. In monoclinic crystals, at least two crystals with a prism shape are needed. The refractive indices can then be measured for different temperatures when the prism is inside an oven. This measurement has the same uncertainty like in the refractive indices measurement. Since the variation of the refractive indices with respect to the temperature is small (on the order of  $10^{-6}\text{K}^{-1}$ ), the variation of the temperature has to be important in order to be able to observe any difference in the measurement, the sensibility of the measurement being

Crystal	$\lambda$ [nm]	$N_p$			$N_m$			$N_g$			Ref.
		$E \parallel N_m$	?	$E \parallel N_g$	$E \parallel N_p$	?	$E \parallel N_g$	$E \parallel N_p$	?	$E \parallel N_m$	
KGW	633		11			65			-182		[37]
KGW	633		-80			67			-141		[37]
KGW:Nd <sup>3+</sup>	1064	-116.4		-193.1	-164.6		-196.7	-150.2		-119.9	[38]
KGW	1064	-120.2		-172.0	-161.1		-181.2	-157.5		-129.3	[38]
KGW	1064		-157			-118			-173		[39]
KLuW	1064		-146			-66			-100		[39]
KGW	1064	-118		-173	-157						[40]
KYW	1064	-89		-124	-146						[40]
KLuW	1064	-66		-100	-146						[40]

Table 2.6 –  $\frac{\delta n}{\delta T}$  of monoclinic double tungstate. Values given in  $\times 10^{-7} K^{-1}$

in the order of  $10^{-4}$ . Furthermore, the possible rotation of the dielectric frame with the temperature is always neglected.

Another method, which is more relevant for such a small variation is to use interferometric methods in order to measure the phase shift and then be able to define the refractive index difference. With such an interferometric approach, it is possible to measure the variation of the refractive indices. The crystal can then be heated using a laser pulse [7]. The variation of the temperature has then to be estimated, and depends on the laser and the crystal parameters. This estimation strongly degrades the accuracy of the measurement since most of the parameters depending on the temperature are roughly estimated.

It results from the measurements of the article [38], that the factor  $\frac{\delta n}{\delta T}$  is mainly determined by the polarization state along the dielectric axis more than by the propagation direction.

# CONICAL REFRACTION

# 3

## INTRODUCTION

In this chapter, the effect of conical refraction will be explained with all its facets. After a brief history about this unique effect, it is first explained using geometric optics. Furthermore, the practical aspect of the conical refraction is discussed. Finally, the full diffraction theory of conical refraction described by Belskii and Khapaliuk in 1978 [41] is presented. The origin and application of this effect is also given at the end of this chapter.

### 3.1 HISTORY OF CONICAL REFRACTION

The conical refraction is a very old phenomenon. It has been first predicted by Hamilton in 1832. He was studying the propagation of light through biaxial media using Fresnel's wave approach. Even if Fresnel was aware of the optic axes, he did not notice the singularity of this orientation in biaxial crystals. Drawing the surface of a biaxial medium, Hamilton wrote the equations describing the propagation along the optic axis of a biaxial medium. He predicted that the light going out from biaxial crystals in such an orientation has to be a cone. He called this phenomenon Conical Refraction. He described two kinds of conical refraction, an internal and an external one. The detailed structures of both of these phenomena are described in the next section. Few months later, Lloyd [42] experimentally observed this effect using a natural aragonite crystal. After its discovery this phenomenon has not attracted any interest from the research community. Only few works are reported over 100 years.

In 1839 Poggendorf [43] found out that the conical refraction is composed of a dark ring surrounded by two bright rings. This discovery had not been predicted by Hamilton. The presence of this dark ring resulting from the singularity will be intensively discussed in the following section since even nowadays its origin is studied in a recent paper [44].

In 1905, Voigt was interested by this effect in optically active materials.

In 1946, Raman [45] experimented this phenomenon in Naphthalene. This material was able to generate very large cone angles of light due to a high refractive index difference.

In 1969, Portigal [46] rewrote the solution of the conical refraction, using similar work on acoustic waves. Bloembergen investigated the second harmonic generation effect along the conical refraction [47, 48].

In 1970, Lalor [49] started to write down the theory of conical refraction.

But it is Belskii and Khapaliuk, in 1978, who published the equations which are able to predict the intensity profile. They applied the diffraction theory for propagation along the optic axis and found out the integral description of the propagation of the conical refraction. The same year, Schell and Bloembergen [50] performed experiments on optically active materials.

In 1994, Fève and Boulanger studied the conical refraction in the KTP crystal [51] and compared it with other materials [52] in 1997.

The theory was rewritten by Berry in 2004 [53], with respect to previous work [54, 55]. In the following years the thesis of Jeffrey [56] was about the mathematical studies of this singularity.

All those publications were mainly about either the theory of conical refraction, either some basic experiment describing the rings' profile. No real applications were studied using this effect before the last decade. This is due to the complexity of this phenomenon. Since this effect is not easy to understand, it is difficult to take advantage of it. A good example is a note published in 1964 [57] that proposed to use the conical refraction for laser beam steering. The authors propose to produce a spot able to move circularly by switching the polarization of the beam passing through a biaxial crystal. In practice this cannot work since at the output of the biaxial crystal one would observe a crescent-shaped beam, not a spot.

Within the last 5 years the number of publications about conical refraction increased. This is mainly due to the availability of long biaxial crystals with good optical quality. Most of them are about the description of conical refraction [58, 59, 60, 61, 62, 63, 64, 65, 66, 67, 68, 69] and beam shaping [70, 71, 72, 73, 74, 75].

Some laser experiments have been performed using this effect. The first one was realised by Hellström [76]. In this work an athermal orientation of an Ytterbium-doped KYW laser proposed in a previous publication [10] was investigated. They thought this orientation was close to the optic axis. During their experiments they discovered that they were able to modify the output polarization of their laser by moving the output coupler. Two other publications [77, 78] report laser operation along the optic axis. However, as it will be discussed in this thesis these results seem to be false. A comparison with the results published at a conference [79], give rise to some doubt about the veracity of these publications.

There are other fields under investigation as microscopy [80, 81], optical tweezers [82, 83, 84], second harmonic generation [48, 85, 86, 87, 88] and demonstration of the Orbital Angular Momentum (OAM) of light [89].

It seems that for some researchers the conical refraction is not enough complicated since, recently, they investigated this effect with metamaterials [90].

This short history of the conical refraction demonstrates that it needs time and tools to investigate this rather complex phenomenon. At the beginning there were no lasers to investigate this effect. As soon as lasers were available the investigation on conical refraction revived but with limited experiments due to the poor quality of the crystals available. Nowa-

days, with the monoclinic double tungstates good crystals are available in order to study the conical refraction. This results in a strong increase of publications about the conical refraction during the last decade. For readers interested in the historical aspects of the conical refraction, they should refer to the chapter about the history of the conical refraction in the thesis of Jeffrey [56].

## 3.2 DESCRIPTION OF THE CONICAL REFRACTION

Before starting to confuse the reader with complicated equations giving the perfect solution of the conical refraction pattern, a practical description of the conical refraction phenomenon will be performed in this section. Several patterns of conical refraction are shown and practical information about the crystal orientation are given.

### 3.2.1 Origin

The conical refraction comes from a singularity point appearing in the refractive index surface of biaxial crystals. The construction of this surface will be detailed later. In this section only intuitive aspects are discussed. For a biaxial medium, this surface is a double-layered surface, one surface for each polarization. When those surfaces cross each other, the refractive indices are equal for both polarizations. This particular orientation is called the optic axis and corresponds to an orientation where both polarizations should be refracted with the same angle. This surface is drawn for a biaxial crystal on Figure 3.1 with  $X$ ,  $Y$ ,  $Z$  the dielectric axes. The optic axes lay in the plane  $XZ$ . Usually, the incident beam perpendicular to the entrance facet is refracted along the normal of the wave surface. As there are two surfaces for the two orthogonal polarizations the refracted beam of a biaxial crystal is usually composed of two spots. The green curve in Figure 3.1 represents the surface corresponding to the  $E \parallel Y(N_m)$  polarization for a beam propagating in the  $XZ$  plane. The red curve in the  $XZ$  plane corresponds to the surface of the  $E \perp Y(N_m)$  polarization.

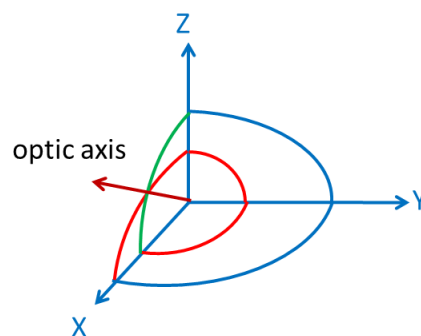


Figure 3.1 – One octant of the refractive index surfaces of a biaxial crystal.

Now let us think about a single ray passing along a biaxial crystal. If we consider the case drawn on Figure 3.2, one single ray will have an infinity of possible propagation directions inside the crystal. This is the internal conical refraction (ICR). For the sake of simplicity, on Figure 3.2

only two of those solutions are drawn. In fact, when observing this surface in 3 dimensions the propagation of this ray is a cone composed by an infinite number of rays. This is the Hamilton's vision of the conical refraction.

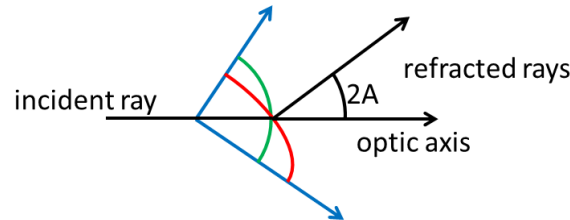


Figure 3.2 – Scheme of a single ray refracted along the optic axis of a biaxial crystal.

However, this is an idealistic case assuming it is possible to send only one optic ray through the optic axis of the crystal. In practice, the beam has always a certain radial extension within the crystal. In this case, the singularity point is surrounded by the light. As it is a singularity, the point of equal refractive index for both polarizations is infinitesimal. In other words, none of the light can reach this point. This was already pointed out by Portugal and Burstein in 1969 [46]. In this case, drawn on Figure 3.3, the unpolarized beam is split depending on the polarization and the 'position' with respect to the optic axis. The thickness of the beam leads to a refraction around the singularity. This case is described in the next section.

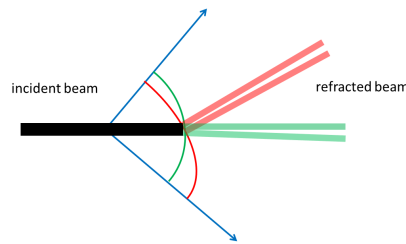


Figure 3.3 – Scheme of a beam passing through a biaxial crystal.

From this basic figure we can conclude that the waist of the incident beam influences the thickness of the annular section of the cone. This will lead to a condition needed to observe the conical refraction on the length of the crystal and the incident beam radius.

The 3D representation of this effect is given on Figure 3.4. On this Figure the cone of conical refraction can be easily observed.

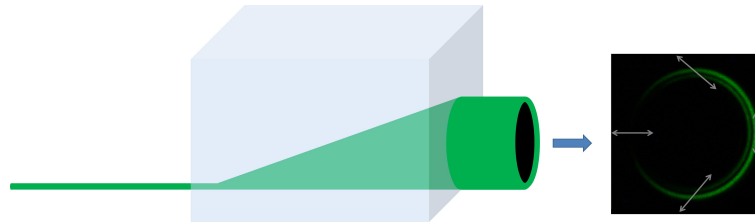


Figure 3.4 – Scheme of a beam passing through a biaxial crystal, with a photograph of the typical crescent shaped profile of a polarized refracted beam.

### 3.2.2 Practical aspects

#### Crystal orientation

In this section some hints are provided in order to rapidly find out the crystal orientation. Observing the conical refraction nowadays is very simple. One just needs a biaxial crystal cut perpendicularly to one of the optic axes, and focus a laser beam into this crystal. The ring pattern will be visible near the focal plane of a lens positioned in front of the crystal. If the crystal is too short or has a low cone angle a second lens can be used after the crystal in order to magnify the ring.

Using polarized light, the orientation of the crystal can be determined by the orientation of the crescent of the polarized conical refraction (CR) pattern. Figure 3.5 shows those patterns for several orientations with a fixed polarization. The axes  $X$ ,  $Y$ ,  $Z$ , correspond to the dielectric frame corresponding to the refractive indices  $n_x < n_y < n_z$ , respectively.

The orientation of the dark part of the ring gives an information of the dielectric frame. It is important to note that all the patterns described in this section are those directly observable at the focal point. If a lens is used to image the ring those patterns will be reversed.

The first remarkable thing about this crescent shaped phenomenon is that when one turns the crystal clockwise, the crescent turns counter-clockwise. This is due to the complex polarization dependency of the conical refraction. In fact, if you consider a fixed polarization, by turning the crystal you will go from one eigen-polarization state (e.g  $E \perp Y$ ) to the other one (e.g  $E \parallel Y$ ).

This polarization dependency can be used in order to determine the orientation of the crystal. The polarization  $E \parallel Y$  is affected by the ordinary refractive index. So, for an incident beam perpendicular to the crystal surface, the beam is not deviated. Observing the part of the cone which is not deviated inside the crystal and turning the incident polarization to

know the corresponding polarization allows to predict the orientation of the dielectric frame, referring to Figure 3.5.

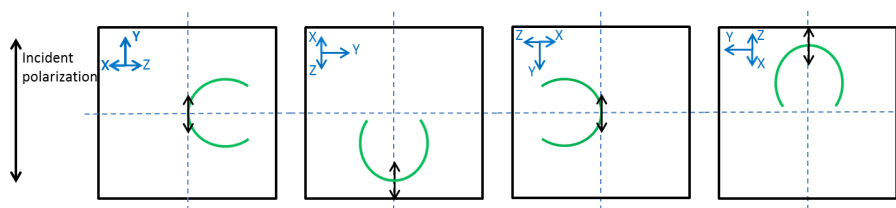


Figure 3.5 – Representation of the output beam (on a screen directly after the crystal) passing along one optic axis of a biaxial crystal for a polarized incident beam.

In practice, it might be difficult to observe the un-deviated side of the cone when the crystal is short or is not well cut for the wavelength used. In fact, when the crystal is tilted, the incident beam is no more perpendicular to the crystal face leading to a shift of the exit beam. The crescent shaped pattern can be used to orient a crystal with a square cross section having one side perpendicular to the Y axis. Furthermore, this method is very practical to orient several crystals in order to obtain cascaded conical refraction [65, 60, 91, 69]. When the crescent shape is tangent with the incident polarization (case of the first and third pictures on Figure 3.5), the plane XZ ( $N_p N_g$ ) is perpendicular to the incident polarization. And when the crescent shape is 'perpendicular' to the incident polarization (case of the second and fourth pictures on Figure 3.5), the XZ ( $N_p N_g$ ) is then tangent to the incident polarization. It is then possible to even know in which orientation is the Z-axis by observing the dark side of the rings. In the first case, the Z-axis is pointing on the side of the dark rings. In the second case, it is pointing on the opposite side of the dark rings.

In the case of a conical refraction laser, it is more important to know how is oriented the XZ plane in order to use the polarization of maximum absorption. The second information on the orientation of the Z-axis is useful for cascaded conical refraction. This orientation corresponds to the side in which the cone expands.

### External Conical Refraction - ECR

The internal conical refraction (ICR) showed before is the easiest to observe since a laser beam passing through a biaxial crystal is sufficient to observe this effect. However, the laws of refraction are similar for both interfaces air-crystal and crystal-air. In other words, the cone of conical refraction can be generated in air at the exit face of the crystal. The propagation direction inside the crystal is different than for the case of internal

conical refraction. In fact, it is along the biradial axis that the light should propagate to give rise to external conical refraction (ECR).

In practice, this effect can be observed by adding an aperture at the exit face of the crystal. The aperture filters the light passing through the biradial axis giving rise to ECR. In the case of several biaxial crystals, one can observe this phenomenon by sending a conically refracted beam through the biaxial crystal. When the crystal is aligned along the biradial axis, the beam will follow this axis. On Figure 3.6 a scheme of this effect is drawn. The picture represents an ECR propagation inside the crystal when the focal point of the incident beam is shifted inside the crystal. In that case we observe a tube of light propagating along the biradial axis.

This effect has not been deeply studied yet and has been demonstrated in a few publications [58], like the ICR, no practical applications have been found up to now.

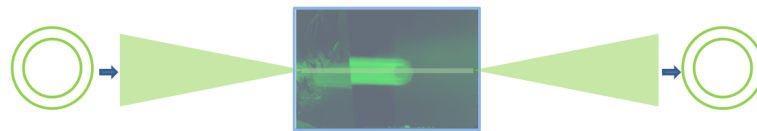


Figure 3.6 – Schematic of the external conical refraction (ECR).

### 3.2.3 Index and wave surfaces and conical refraction

The index and wave surfaces have already been described in the previous chapter for the description of the absorption near the optic axis in biaxial crystals. In this section, we will focus on the dependency of the conical refraction with respect to these surfaces. The directions and the angles of the cones of ICR and ECR are related to the index and wave surfaces, respectively.

#### Index surfaces

The index surfaces are described by the refractive index of the material. In the previous chapter, the imaginary part of these surfaces using equation (2.30) from [33] has already been drawn. This equation is valid for orthorhombic crystals. It can be used for lower symmetry crystals only if the dielectric tensor is expressed using the dielectric frame (i.e. the frame of the diagonalized matrix). As it was mentioned in the previous chapter, this eigenframe of the real part of this matrix may differ from the imaginary part [24] in the case of monoclinic crystals. Here is given the general equation valid whatever the crystal symmetry or the frame used.

In order to describe the index surface, the 'index equation' is used. This equation can be found in optics books [92]. This equation is, in most of the cases, written using the dielectric eigen frame. This is equation (3.1), where  $k_i$  (with  $i = x, y, z$ ) represents the propagation direction ( $\sum_i k_i^2 = 0$ ). This equation in  $n^2$  has four solutions. In physics, we retain only the positive solutions. Then we obtain two solutions  $n^+$  for the external index surface and  $n^-$  for the inner surface. When drawing those two surfaces in the dielectric plane, they simply result in a circular and an elliptical surface.

$$\frac{n_x k_x}{n^2 - n_x^2} + \frac{n_y k_y}{n^2 - n_y^2} + \frac{n_z k_z}{n^2 - n_z^2} = 0 \quad (3.1)$$

Or in a more compact way :

$$\sum_i \frac{n_i k_i}{n^2 - n_i^2} = 0 \quad (3.2)$$

The solutions of this equation are the same as for in the equation (2.30) of the previous chapter.

### Wave surface

The wave surface is expressed by the same equation than the refractive index surface just by replacing the  $n_i$  by  $\frac{1}{n_i}$  with  $i=x,y,z$ . This surface represents the equivalent surface for external conical refraction. It also contains the ray path of the beam.

### 3.2.4 Influence of those two surfaces on conical refraction

In this section some ray tracing simulations of rays passing along the optic axis are provided. This is performed in order to understand the influence of each surface on the conical refraction pattern. After describing the simulation, one case considering an unpolarized beam, and another one considering the polarization will be presented.

#### Description of the computation

In order to fully understand the influence of each surface on the conical pattern, a very simple simulation is proposed here. It consists in having a collimated beam being refracted by the refractive index surfaces along the optic axis. In this simple case, the refracted rays propagate to the normal of these surfaces. The surfaces are generated using the equations

of the previous section. The incident beam is represented by a perfectly collimated Gaussian beam, with the profile stored in a matrix. This beam is then refracted on the refractive index surface. The deviation of the beam is then stored in another matrix. This last matrix can be used to determine the beam profile after propagation.

This computation of ray tracing has a fixed number of rays determined by the incident beam matrix. The resolution of this simulation is then determined by the size of this matrix. In the following the output will have some artefact coming from the choice of using a fixed matrix as input. However, it is sufficient in order to understand more deeply the conical refraction phenomenon and to observe the impact of both surfaces.

In the last part of this section the polarization of the light is taken into account. In this case we used two incident matrices each one having one state of polarization. They are both refracted on the surfaces taking into account the influence of the polarization as it was described in the previous chapter. Then both matrices can be summed in order to obtain the pattern of unpolarized light.

It is important to note that ray tracing does not allow to observe the exact double rings shaped beam of conical refraction since interference is not taken into account.

### **Unpolarized beam**

When the light is unpolarized, it is a very simple case. We just have to assume, wherever the beam is, it is equally refracted by both surfaces. This has already been done for example in the thesis of Sluijter [93]. In this case he has even taken into account the solid angle of the incident beam. In this case he demonstrated that the ring of the conical refraction gets broader when the solid angle increases.

The contribution of the inner and the outer refractive index surfaces is simulated on Figure 3.7. This simulation helps us to understand this phenomenon in more detail. The inner surface seems to be responsible of the internal part of the cone, and the outer surface generated the outer part of the cone. This information seems, at first sight, not really important. However, this is of drastic importance in the case of polarized light as it is shown in the following.

The ray tracing simulation allows also to simulate misalignment of the conical refraction. The transition from classical double refraction to conical refraction is depicted on Figure 3.8. This simulation is realistic.

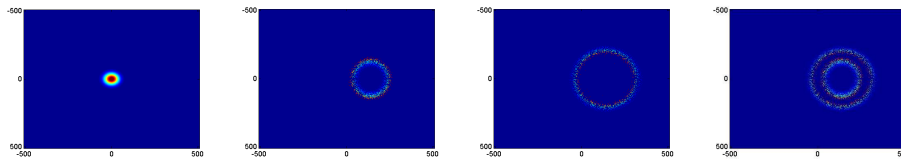


Figure 3.7 – Simulation of conical refraction showing the contribution of the inner and the outer refractive index surfaces. From left to right, incident beam, refraction on the inner surface, refraction on the outer surface, refraction on both surfaces.

It is exactly what happens in the lab when the crystal is tilted. During this transition one of the double refracted spots changes its shape from a circular one to a crescent-shaped and then a ring-shaped. The other spot is lengthened horizontally, before having the crescent-shape and then a ring-shape. In practice, the second spot is not so thin when it is stretched. The divergence will produce broader patterns.

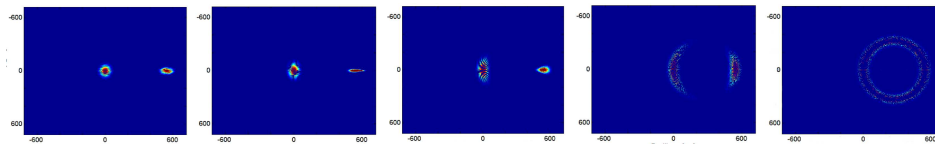


Figure 3.8 – Simulation of the transition from double refraction to conical refraction.

With those two simulations, the visible part of the conical refraction is described. However, it is also important to know what happens inside the crystal and how this double ring-shaped beam appears. The evolution of the incident beam with respect to the propagation length inside the crystal is depicted on Figure 3.9. The true evolution inside the crystal can only be described by using ray tracing simulation. In fact, the usual equation used to describe conical refraction shown in the next section describes the evolution in the Fourier plane, in other words, the evolution of the beam shape at the focal point of a lens after the refraction has occurred. The light rapidly diverges after the crystal entrance and after few millimeters the rings can be observed (with a  $40\ \mu\text{m}$  incident beam and a KGW crystal used in this simulation).

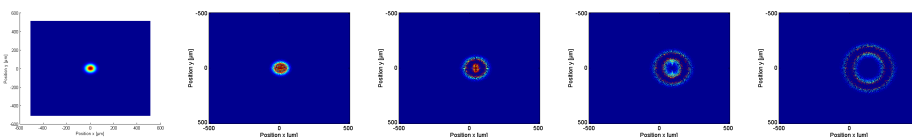


Figure 3.9 – Simulation of the propagation of the beam inside the crystal, from left to right at, 0 mm, 1 mm, 5 mm, 10 mm, 15 mm, respectively.

### Polarized beam

The case of a polarized beam is more tricky. The link between polarizations and refraction surfaces is not trivial when going away from the principal planes of the dielectric frame. The link between the orientation and the polarization has already been discussed in the previous chapter. The same equations (2.32) are used here in order to know the part of the beam that is refracted on each surface. The transformation from the double to the conical refraction is illustrated on Figure 3.10 for a polarized incident beam. The polarization was set to  $E \perp Y(N_m)$ , and the surfaces were tilted within the XZ plane. In this case, there is only one refracted spot when the crystal is tilted away from the optic axis. Then, when the beam is close to the optic axis it is refracted by both surfaces, and the crescent-shaped beam appears. It is interesting to observe that the propagation of the different polarizations leads to have orthogonal polarization for each opposite side of the cone.

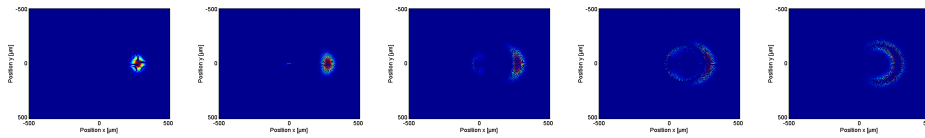


Figure 3.10 – Simulation of the transition from double refraction to conical refraction in the case of a polarized incident beam. The misalignment angles are, from left to right, 2 mrad, 1 mrad, 0.4 mrad, 0.2 mrad, 0 mrad, respectively.

In this section, the surface and polarization dependency for conical refraction have been discussed. Those simulations give a thorough understanding of how the beam is refracted along the optic axis.

### 3.3 MATHEMATICAL THEORY OF CONICAL REFRACTION

In this section the mathematical description of the conical refraction is given. The first equations were derived by Hamilton [94]. Several authors proposed some equations based on Fresnel's waves approach aspect to describe the conical refraction [46, 49]. Here, we will use the same equations as the ones provided by Berry [53] based on the diffraction theory under paraxial approximation. They are derived from the theory of Belskii and Khapalyuk [41], but written in a more practical form. Those equations are able to predict the double ring-shaped beam of conical refraction and allow to predict the space profile evolution of a conically refracted beam.

#### 3.3.1 Parameters of conical refraction

The description of some parameters needed to fully understand the conical refraction equation will be provided in this section. The ring radius of a conically refracted beam will depend of the cone angle and the length of the crystal. The cone angle is related to the refractive index difference. This is completely dependent of the crystal. Thus, there are only two ways to modify the conical refraction ring radius, either by modifying the length of the crystal, or by changing the crystal. The conical refraction angles  $A$  of several media are given in Table 3.1.

##### Angle $A$

The calculation of the angle  $A$  is performed using the refractive index surfaces of a biaxial crystal. The calculation gives the semi-angle  $A$  of the cone as represented on Figure 3.11.

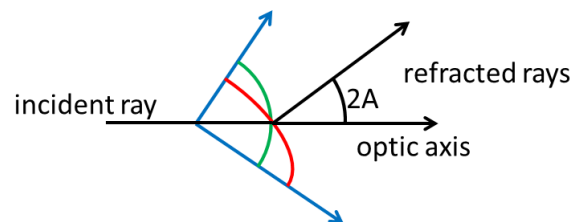


Figure 3.11 – Scheme showing the semi-angle  $A$  of the conical refraction.

Using a geometrical approach, the semi-angle  $A$  can be determined. This expression takes several forms in the literature.

This angle only depends on the crystal's refractive indices and is given by equation (3.3).

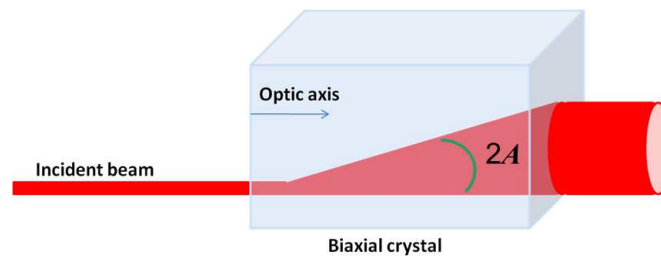
Table 3.1 shows these values for some different crystals.

Matrices	$n_p$	$n_m$	$n_g$	$A[^\circ]$	Ref.
KY(WO <sub>4</sub> ) <sub>2</sub>	2.021(39)	2.064(94)	2.111(75)	1.25(28)	[95]
Nd:KGd(WO <sub>4</sub> ) <sub>2</sub>	1.937	1.986	2.033	1.38(45)	[7]
Er:KGd(WO <sub>4</sub> ) <sub>2</sub>	1.981(9)	2.010(3)	2.061(0)	1.08(15)	[13]
KLu(WO <sub>4</sub> ) <sub>2</sub>	?	?	2.113	?	[16]
BaY <sub>2</sub> F <sub>8</sub>	1.573(6)	1.575(8)	1.581(4)	0.12(74)	[96]
Er:Li <sub>6</sub> Y(BO <sub>3</sub> ) <sub>3</sub>	1.570(7)	1.570(8)	1.624(7)	0.08(47)	[97]
Naphtalen	1.525	1.722	1.945	6.97(39)	[95]
KTP	1.738	1.747	1.833	0.91(24)	[33]
BiBO	1.7585	1.7854	1.9190	1.92(38)	[98]

Table 3.1 – Refractive indices and angle  $A$  for several biaxial crystals at 1060 nm.

$$A = \frac{1}{n_m} \sqrt{(n_m - n_p)(n_g - n_m)} \quad (3.3)$$

### 3.3.2 Conical refraction equations

Figure 3.12 – Semi-angle  $A$ .

The parameter  $\rho_0$  simply consists in the multiplication of the semi-angle  $A$  (see Figure 3.12) and the length of the crystal divided by the incident beam waist radius  $w$  to obtain a parameter comparable for different crystals and incident beam waist.

$$\rho_0 \equiv \frac{Al}{w} \quad (3.4)$$

In order to express the radius of the beam we use the parameter  $\rho$ , where  $r$  represents the radial position.

$$\rho \equiv \frac{r}{w} \quad (3.5)$$

The  $\zeta$  parameter corresponds to the propagation distance inside the crystal and is given by equation (3.6). With  $Z$  between 0 and  $l$  the crystal length corresponding to the propagation taking into account the refractive index of the crystal. The real propagation  $z$  is equal to,  $z = l(1 - \frac{1}{n_m})$ ,

for  $Z = 0$ . At the exit of the crystal both are equal to 1 [53] and  $k$  the wavenumber.

$$\zeta \equiv \frac{Z}{kw^2} \quad (3.6)$$

### 3.3.3 Diffraction equations

Now all parameters have been introduced, the equation of the diffraction theory is provided. The origin of those equations will not be described in this thesis. The reader is referred to the original work of Belskii and Khapalyuk [41], as well as Berry [53], and the thesis of Jeffrey [56] for more details.

#### Incident beam

Here only the classical Gaussian beam (see Figure 3.13) is taken into account as incident beam. Various incident beams can be investigated. In fact, each kind of beam refracting on the surface will exert a specific beam profile. Some authors have investigated super-gaussian beams [64], top-hat beams [62], Laguerre-Gauss beams [71, 67], elliptical beams [63] and of course conically refracted beams [69, 65, 91]. For most of those beams the refracted patterns are still rings, with different number and spacing. For the experiment presented in this thesis the Gaussian case is the most relevant one, since the pumping laser source has a good beam quality. Furthermore, the classical solutions of the resonating modes inside a laser cavity are Gaussian.

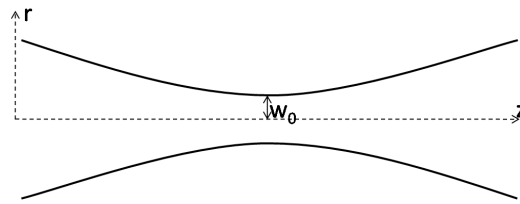


Figure 3.13 – Representation of a Gaussian beam.

A Gaussian beam is expressed by the following equation, with  $w$  the beam waist radius, and  $r$  the radius position (along the propagation axis).

$$E \propto \exp\left(-\frac{r^2}{2w^2}\right) \quad (3.7)$$

### Berry's equations

For circularly polarized light the intensity pattern of the beam can be expressed with the following equation :

$$I(\rho, \zeta, \rho_0) = \frac{1}{1 + \zeta^2} \left| C_0\left(\frac{\rho}{\sqrt{1 + i\zeta}}, \frac{\rho_0}{\sqrt{1 + i\zeta}}\right) \right|^2 + \left| C_1\left(\frac{\rho}{\sqrt{1 + i\zeta}}, \frac{\rho_0}{\sqrt{1 + i\zeta}}\right) \right|^2 \quad (3.8)$$

with,

$$\begin{aligned} C_0(u, u_0) &= \int_0^\infty q \exp\left(-\frac{q^2}{2} \cos(u_0 q)\right) J_0(uq) dq, \\ C_1(u, u_0) &= \int_0^\infty q \exp\left(-\frac{q^2}{2} \sin(u_0 q)\right) J_1(uq) dq, \end{aligned} \quad (3.9)$$

The intensity profile after the conical refraction can be used using this equation (3.8). This equation can be found in literature under various forms, but it is always an integral with a Bessel function, a cosine or a sine, and a function depending on the incident beam. It is possible under some conditions to use approximations instead of those integrals as it has been done in [53]. However, in that case one is losing in generality, and different equations have to be used depending of the position.

The integration of the equation 3.9 is not an easy task. In fact, it is an integration to the infinite with strongly oscillating terms inside this integral. Numerically, the infinite cannot be reached. Furthermore, depending on the integration method it might be possible or not to calculate it. It is important to point out that there is a lack of information in most of the publications considering those integrations. As it is always calculated numerically, the result is an approximation of the real value. The integration method used and the different parameters should be known but this is not specified in most of the publications. Only publication [59] explicits the upper limit of the integral used.

Figure 3.14 shows the result of this equation for  $\rho_0 = 60$  and  $\zeta = 0$  using an upper limit of 2 and the Simpson algorithm to calculate the integral. The calculations have been done for  $\rho = 0$  up to  $\rho = 80$ . Figure 3.14 shows the profile of the inner and the outer rings.

It is also possible to calculate the profile along the propagation direction  $\zeta$ . This case is drawn on Figure 3.15. The parameter  $\zeta$  is varying horizontally and the parameter  $\rho$  vertically. In the middle of the figure one can observe the classical double ring-shaped beam resulting from conical refraction with the Poggendorff's dark ring. At the edge of the figure the so-called Raman spot is present with the highest intensity.

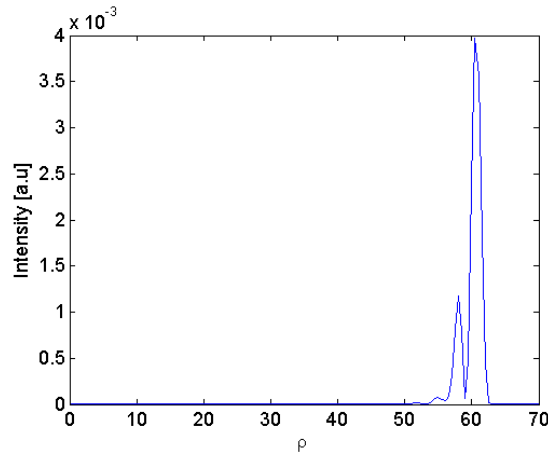


Figure 3.14 – Intensity profile for  $\rho_0 = 60$  and  $\zeta = 0$ , with the upper limit of the integral fixed at 2.

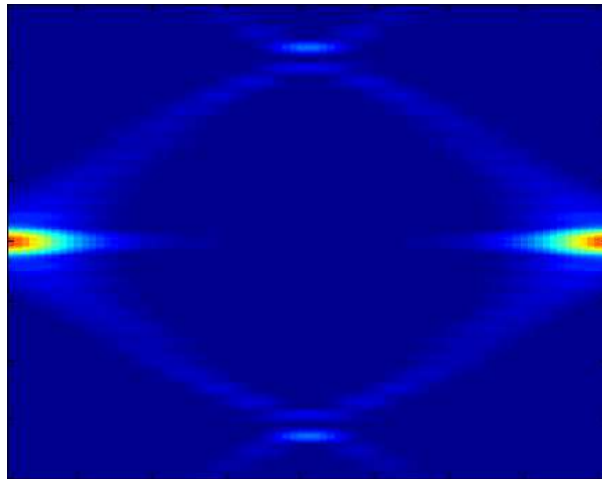


Figure 3.15 – Intensity profile for  $\rho_0 = 60$  and  $\zeta$  from  $-20$  to  $20$ , with the upper limit of the integral fixed at 2 for  $\rho_0 = 2$ .

### 3.4 DIFFERENT BEAM PROFILES RESULTING FROM CR

In the previous section the main pattern of conical refraction has been given with the classical double-ring shape of conical refraction. In this section, the different patterns that can be observed from different conical refractions are presented using a biaxial crystal cut perpendicularly to the optic axis. Those patterns are given in order to provide the possibility to every experimentator to rapidly find out what one is observing. As it is shown in this section a lot of patterns can result from conical refraction. This section is strongly inspired by the publication of Peet [66].

Let's first of all explain the different terminology used in order to describe those patterns. In order to observe the conical refraction, we used a classical 2f system. This simply consists in a two-lens system, as it is used in order to observe the diffraction pattern of a pinhole. In our case the bi-

axial crystal does not need to be exactly at the focal point of the first lens in order to observe the conical refraction. It can be positioned wherever between the two lenses, when the distance between the two lenses is equal to the sum of both focal lengths plus a small distance  $z_0$  taking into account the refractive index of the crystal. With such a system the second lens is just an imaging lens. When the distance of those two lenses is equal to the sum of both focal lengths plus the  $z_0$  terms, the image produced on a screen or a camera at the infinite is the near field. This near field coincides with the double ring-shaped beam of conical refraction. When the second lens is removed we will observe the far field of the conical refraction.

### 3.4.1 Near field

The incident beam polarization is important as it can be linearly, circularly or unpolarized. Furthermore, we can put an analyzer just before the camera in order to separate two linearly polarized components.

These are the simplest cases that one can observe with conical refraction. The pictures have been computed using the integrals shown in the previous section. The simulations of the CR beam pattern have been performed using  $2 \mu\text{m}$  wavelength and a relatively large input beam ( $100 \mu\text{m}$ ) in the case of a KGW crystal. This leads to have a parameter  $\rho_0$  small. Therefore, the CR pattern is thick and the inner ring is barely visible. Those patterns are very similar as the ones we obtained during the laser experiment at  $2 \mu\text{m}$ . In Figure 3.16 are represented those different patterns for different incident polarizations and analyzer orientations (linear polarizer set before the screen).

The different polarization patterns are obtained using the azimuthal angle  $\iota$  as it has been performed in the previous section and in publication [66]. The intensity is normalized for each picture with respect to its maximum. The images are given with a linear scale of the intensity.

The classical double ring-shaped patterns of conical refraction can be observed for unpolarized or circularly polarized incident light. In the case of polarized light the crescent-shaped patterns are observed using polarized incident beam and analyzer. By crossing the incident polarization and the analyzer two opposite parts of the rings can be observed.

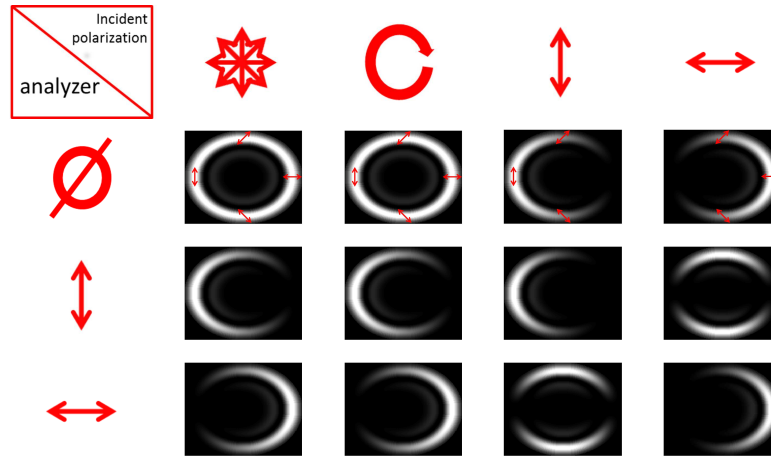


Figure 3.16 – Near field profiles of conical refraction, for  $\lambda = 2 \mu\text{m}$ ,  $w_0 = 100 \mu\text{m}$  and  $A = 20 \text{ mrad}$ .

### 3.4.2 Far field

The near field patterns, shown on Figure 3.16 are well-known and are constituted of the double ring-shaped beam, simply transforming into crescent-shaped beams depending on the polarization.

It is interesting to investigate the far field profiles, since this is the mode that we observed when there is no second lens or this one is not at the right position. This case is shown in Figure 3.17. For an unpolarized beam without any analyzer the beam almost looks like a Gaussian beam. If it is well aligned this Gaussian beam looks circular. A brighter dot in the center of this Gaussian profile can be observed when the beam profile is taken in between the near and far fields. This results from the so-called Raman spot.

All the polarized components can be calculated using the diffraction theory described in the previous section. The terms  $B_0$  and  $B_1$  represent the solution for both circular polarizations (right and left). In case of circularly polarized light the far field beam is a Bessel-Gauss beam defined by the  $B_0$  and  $B_1$  components. The pattern is then a Bessel-Gauss beam of order 0 (with maximum intensity in the center of the beam) and order 1 (with minimum intensity in the center of the beam). Using the azimuth angle  $\iota$  described in the previous section it is possible to deduce the case using an analyzer for  $E_{\parallel N_m}$  and  $E_{\perp N_m}$  using the equations (3.10) and (3.11) provided in [66].

$$I_{E_{\parallel N_m}} \propto |B_1 \cos \iota|^2 \quad (3.10)$$

$$I_{E_{\perp N_m}} \propto |B_0 + B_1 \sin \iota|^2 \quad (3.11)$$

The patterns resulting from polarized light are less intuitive than the ones observed in the near field. In Figure 3.17 are represented the far field beam profiles for conically refracted beams with  $\rho = 1.5$ . Those profiles are observed in the conical refraction laser presented in the last chapter.

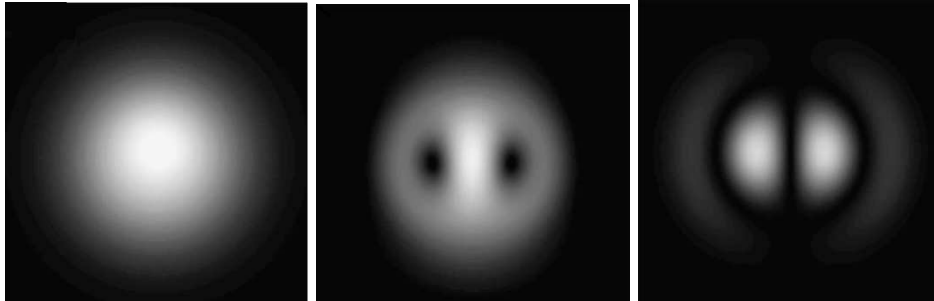


Figure 3.17 – Far field profiles of conical refraction,  $\rho = 1.5$ . From left to right, unpolarized, with analyzer parallel to  $N_m$ , with analyzer perpendicular to  $N_m$ .

### 3.4.3 Raman spot

The transition between the near field and the far field pattern of conical refraction exerts the so-called Raman spot of conical refraction. This pattern described by Raman [45] shows a bright spot in the center of the pattern. This spot appears when the distance is long enough to observe the convergence of the inner ring. The central spot intensity decreases during the propagation. At the far field (in the case of unpolarized light) a Gaussian profile of the beam can be observed. The intensity profile of this Raman spot is simply a brighter spot in the middle of the Gaussian envelop appearing in the middle field.

This phenomenon can be used to align the crystal for conical refraction. In practice, this spot is centered when the light propagates along the optic axis. However, in the case of misalignment this spot is no more centered. A simple way to align the crystal is then to move this bright spot in the center of the pattern. This is useful when one uses a highly divergent beam, e.g fiber coupled pump diode beam with high numerical aperture. With such a beam, it is not possible to observe the double ring-shaped beam, but the Raman spot can be observed.



# DISPERSION AND ABSORPTION MEASUREMENT

## INTRODUCTION

In this chapter the measurements on the dispersion of the optic axis and the absorption measurement of the Holmium-doped KYW are described. Those measurements have been carried out in order to know if this dispersion is significant. The dispersion measurements have been performed at LOMA in the University of Bordeaux. The absorption measurements were carried out at ISL. Those latter are in agreement with the study performed in Chapter 2 about monoclinic crystal absorption along the optic axis.

#### 4.1 DISPERSION OF THE OPTIC AXIS

In our CR experiments the propagation direction is along the optic axis of the monoclinic crystal, which offers an easy way to measure the dispersion of this optic axis. Moreover, the measurement of the wavelength dispersion of the optic axis permits to check the validity of the Sellmeier equations given in literature. In fact, when calculating the dispersion with these equations, these measurements are not accurate enough to predict the orientation for a large wavelength range as pointed out in Chapter 2. The angle  $V$  giving the dispersion, between the  $n_z$  (Z) axis and the optic axis in the X-Z plane, can be easily calculated using equation 4.1 [92] given without any approximation.

$$\tan^2(V) = \frac{n_z^2(n_y^2 - n_x^2)}{n_x^2(n_z^2 - n_y^2)} \quad (4.1)$$

For example, the dispersion resulting from the different measurements provided by the literature has been calculated and is shown on Figure 4.1. The absolute value and the shape of the dispersion are completely different for the dispersion calculations. The flat asymptote at higher wavelength is visible. The difference observed between all those measurements cannot be explained by the difference in doping. In fact, these matrices are similar and should not have such a big difference. The dispersion should be similar to the evolution of the refractive indices: an important increase to short wavelengths, a plateau for the wavelength in the transparency region and another strong variation at the end of the transparency region near  $5 \mu\text{m}$ .

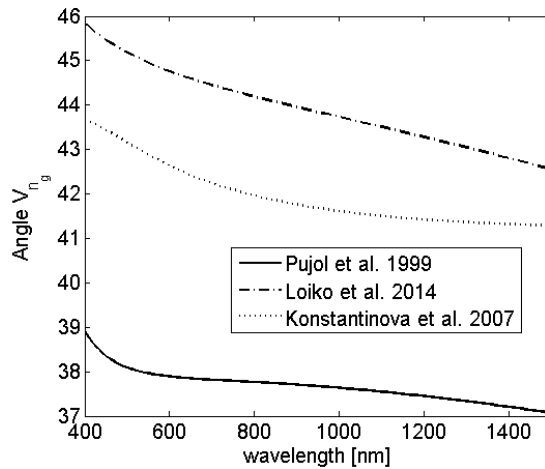


Figure 4.1 – Dispersion of the optic axis in KREW.

#### 4.1.1 X-ray diffraction measurements

The X-ray diffraction measurements of KGW samples have been performed at the ICMCB, University of Bordeaux. It consists in an X-ray beam passing through the crystal. The diffracted beam is recorded behind the crystal. The diffraction pattern can then be used to obtain the crystallographic orientation of the sample. The picture resulting from such experiment is shown in Figure 4.2. This picture has been taken with one of the Neodymium-doped KGW samples cut perpendicularly to the optic axis for a wavelength of 633 nm.

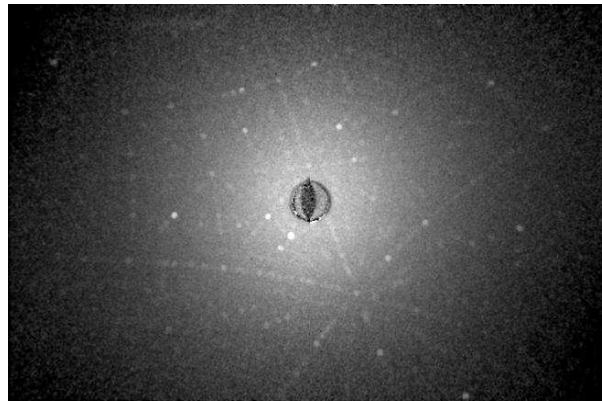


Figure 4.2 – X-ray diffraction pattern of Neodymium-doped KGW sample cut perpendicularly to the optic axis for a wavelength of 633 nm.

The software OrientExpress is used to find the orientation of the sample. The lattice parameters of the material have to be known. The lattice parameters from Pujol *et al.* [13] have been used to find the orientation. In Figure 4.3 is shown the stereo visualization of the crystal orientation obtained. The lattice parameters used are given in this figure. A schematic representation of the crystal is also presented with the orientation of the dielectric frame. The angle of  $35^\circ$  corresponds to the dispersion plane observed. The orientation of the crystallographic **b**-axis has also this angle. This orientation corresponds to an angle  $V$  of  $43.3^\circ$  for the Neodymium-doped KGW.

It is important to note that the samples are mechanically aligned inside the X-Ray beam. The crystal facet might not be perfectly perpendicular to the X-ray beam. This results in an angle uncertainty of  $1^\circ$ .

#### 4.1.2 Experimental setup

The measurements of the angular variation of the optic axis orientation with wavelength were performed at LOMA in Bordeaux. The range from

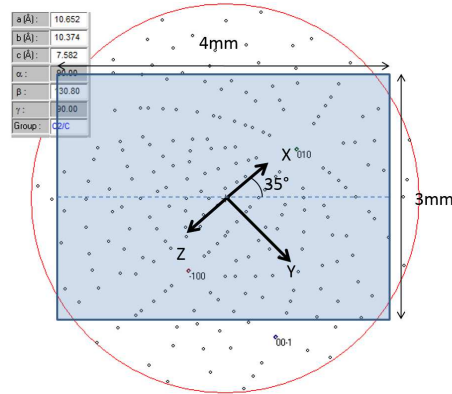


Figure 4.3 – Orientation of  $\text{Nd}^{3+}:\text{KGW}$  calculated using the software OrientExpress.

430 nm up to 1580 nm could be covered using a Ti:Sapphire laser, a compact OPO (Chameleon/Coherent) and optional frequency doubling with a BBO crystal. The wavelength of the primary Ti:Sapphire source is tunable from 680 nm to 1080 nm. With the OPO it is possible to reach the wavelength range from 1040 nm up to 1580 nm. By doubling the Ti:Sa laser, the wavelengths from 430 nm to 530 nm, and by frequency doubling of the output beam after the OPO, 520 nm to 670 nm were obtained. To ensure very precise alignment of the incident beam on the crystals for all wavelengths, the beam of the selected wavelength was injected into a single-mode optic fiber. Two different fibers have been used for the visible and the infrared range, Thorlabs P1-460A-FC-2 and P1-630A-FC-2, respectively. A collimated output FC connector was used to ensure that the output beam will point exactly in the same direction even when the fibers are switched. A lens ( $f=125$  mm) was used to focus the light inside the crystals, another one ( $f=125$  mm) was used to more or less collimate the beam after the crystal, and a last one of short focal length ( $f=40$  mm) was used to magnify the rings for better observation, and to correct the focal variation with wavelength. Figure 4.4 shows a schematic drawing of the experimental setup. The two Nd-doped (at 3 at%) KGW samples with dimensions  $3 \times 4 \times 11$  mm, and an undoped KGW crystal with the dimensions  $3 \times 3 \times 10$  mm were used. Each of the samples was fixed on a crystal mount which was positioned on a goniometer driven by a microcontroller with an angular step of  $10^{-3}$  degrees.

The sample mount was very accurately fixed in the center of the goniometer. The doped crystals were cut for internal conical refraction (ICR) at 633 nm with a misalignment of 1.25 mrad. Therefore, the first alignment for ICR was performed at this wavelength for one of the doped crystals by turning the goniometer until the CR rings appeared.

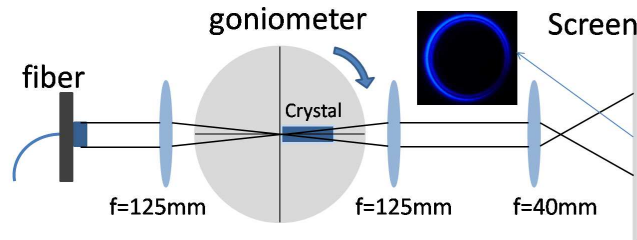


Figure 4.4 – Scheme of the experimental setup.

To ensure that the plane of variation of the optic axis was perpendicular to the rotation axis of the goniometer, a simple and efficient alignment procedure was applied. The wavelength was changed and the goniometer was turned until the ICR was aligned in the vertical rotation axis. Instead of tilting the crystal with the horizontal rotation axis to have correct alignment, the crystal was rotated with respect to the propagation axis. To check the alignment, an upper and a lower wavelength several hundred nanometers apart were set successively and verification has been done to ensure that only the goniometer has to be turned to re-obtain the rings for both wavelengths. Figure 4.5 shows the intensity profile when the crystal is aligned and misaligned for conical refraction. With this method, the horizontal plane of the crystal is well aligned in its dispersion plane.

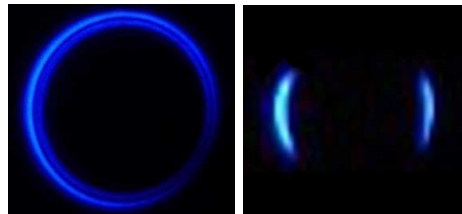


Figure 4.5 – Intensity profile when the crystal is aligned for conical refraction (left), and misaligned (right).

The second Nd-doped crystal was then aligned with back reflection, whereas the undoped KGW was the most difficult to align in the right plane due to its large cutting imprecision which leads to a deviation of 70 mrad. This difference can be explained by the fact that the crystals were bought from different companies.

As not all wavelengths were available simultaneously because of the switching from the Ti:Sapphire laser to the OPO, realignment of the fiber injection was necessary. Correct reproducibility was ensured by checking the overlap for some wavelengths accessible with the different sources.

### 4.1.3 Results

The angular variation obtained with this measurement system for KGW and Nd-doped KGW is shown in Figure 4.6 with a comparison to the calculated optic axis angle from the refractive indices of Er-doped KGW and Nd-doped KGW using equation 4.1. It is important to note that the measurements performed with this method only give the relative variation of the angle. In order to compare the result with calculated values, the reference angle of  $43.3^\circ$  and  $42.1^\circ$  at 630 nm has been chosen to scale the experimental values of Nd-doped KGW and undoped KGW, respectively. Those reference angles have been determined using X-ray measurements of the crystals. The measured variation angles of the goniometer scale have been divided by  $n_y$ , to take into account the refraction at the entrance surface.

A variation of the optic axis is observed becoming asymptotic in the infrared region. The variation within the range of 430 nm to 1580 nm is about  $2.4^\circ$ . No significant difference of the curve shape is observed between the doped and undoped double tungstates. Some measurement points could not be taken for the doped KGW crystals, because of the absorption in the visible region of these samples. For example at 600 nm, one should consider if those absorption bands could lead to a change of the birefringence and thus influence the dispersion. However, the highest variation of the birefringence due to absorption reported in [21] is about  $10^{-6}$  and located at 600 nm. This is far too low to have a significant impact on the optic axis orientation and can thus be neglected.

During the measurement process only a single screw was used to align successively each wavelength for ICR. The orientation changes observed in KGW therefore can only occur in one plane within our wavelength measurement range and within the mechanical accuracy. A rotation in the other plane may exist on a very small level or for an extended measurement range.

The measurements were reproducible with an uncertainty of around  $0.1^\circ$  in relative measurements. The uncertainty of the reference used is much higher, and was determined by the X-ray diffraction measurement to approximately  $1.5^\circ$  (indicated by the error bars in Figure 4.6). For some points the relative uncertainty is slightly higher, due to the difficulty to align for ICR with low intensity. This problem occurs beyond 1500 nm, and for some absorption regions of the Nd-doped samples in the visible range. However, one can observe that the shapes of the measured and the

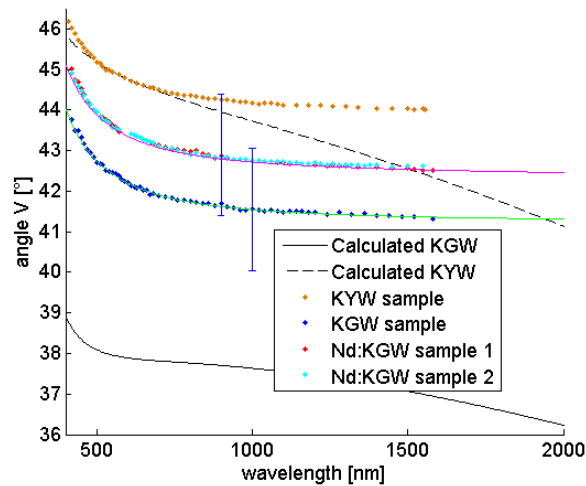


Figure 4.6 – Angle  $V$  as a function of the wavelength (calculated KGW and KYW: obtained using Sellmeier equations from Pujol *et al.* [13] and from Loiko *et al.* [22], respectively, measurement of the angle  $V$  variation is referenced at  $43.3^\circ$  and  $42.1^\circ$  at  $630\text{ nm}$  for Nd-doped KGW and undoped KGW, respectively; green and pink curves are calculated using the modified  $n_z$  refractive index).

theoretical curves are significantly different in the infrared region. This arises from the extreme sensitivity of the angle  $V$  on the refractive index value differences. In fact, a slight change of only one of the three refractive indices values changes the shape of the calculated graph and allows for a good agreement in the two curves. In the next paragraph such a correction of the refraction index is shown. As can be seen in Figure 4.6 the prediction calculated from the indices of reference [21] does not match our experimental result at all. This is probably due to Sellmeier fitting performed over a limited wavelength range with a limited number of data points only.

#### 4.1.4 Modification of the refractive index " $n_z$ "

In this part a correction will be applied to the refractive index of Pujol *et al.* [13] in order to bring the calculated values into agreement with the measured ones. This kind of correction cannot be applied on Konstantinova *et al.*'s refractive indices [21] due to the limited measurement range which does not allow to determine an evolution of one refractive index. Using equation 4.1, it is possible to define one refractive index as a function of the angle  $V$  and of the two other refractive indices. This will be used to recalculate one of the 3 refractive indices with the means of the measured angle  $V$ . The  $n_z$  refractive index is the one that will be corrected for two reasons. The first one is that as shown in Figure 2.9 from Pujol *et*

*al.*,  $n_x$  and  $n_y$  seem to be equal for differently doped KGW matrices. The second reason is illustrated in Figure 4.7. In fact, looking at the derivatives  $\frac{dn}{d\lambda}$  of the indices of Pujol show that  $n_z$  does not follow the same variation as  $n_x$  and  $n_y$ . It is this difference that leads to the variation of the calculated angle V in Figure 4.6. This perturbed derivative evolution could be linked to the last measurement point of  $n_z$  near 1500 nm in Pujol *et al.* which is not well matched by the Sellmeier fit [13].

In Figure 4.7, the modified  $n_z$  values with respect to the original ones from Pujol *et al.* are shown for comparison. The difference between Pujol *et al.*  $n_z$  refractive indices and the refined ones is about 0.014 and 0.018 for undoped KGW and Nd-doped KGW, respectively. Therefore, a small correction of the refractive index  $n_z$  can be derived from our experimental results. The index is given by equation 2.27.

With this new refractive index the angle V can be recalculated. Indeed, the angle V calculation is very sensitive to the refractive index, for a variation of the refractive index of 0.0005, the angle may vary by  $0.15^\circ$ . With the Sellmeier fit employed it is not possible to be more precise than this value.

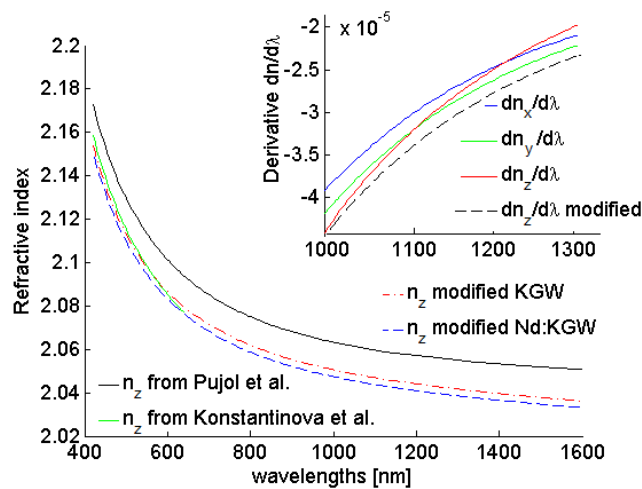


Figure 4.7 – Derivative of Pujol *et al.*'s refractive index and the modified one (insert, top right) and comparison between  $n_z$  from Pujol *et al.* and the modified ones (see text).

#### 4.1.5 Dispersion of Holmium-doped KYW

The dispersion of a Holmium-doped KYW sample has also been measured. The orientation of the sample was known. Thus, the measurement points in Figure 4.8 are directly given in absolute values.

The measured dispersion is in good agreement with the calculation performed using the refractive indices provided by Kaminskii *et al.* [19].

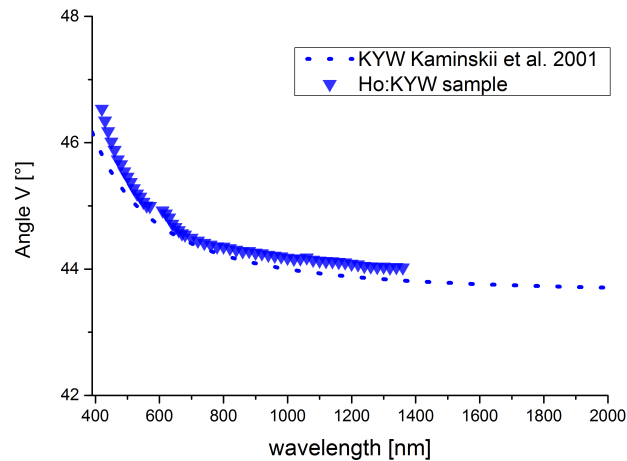


Figure 4.8 – Optic axis dispersion of  $Ho^{3+}$ :KYW.

#### 4.1.6 Conclusion

In order to predict the evolution of the optic axis with wavelength, the three refractive index values have to be known to better than  $10^{-3}$ . The variation of the angle  $V$  has been measured over the range from 430 nm to 1580 nm and a correction of the  $n_z$  refractive index taken from literature has been performed but should not be taken as "true" value. Over the measurement range a variation of  $2.4^\circ$  has been measured. No significant difference of the variation has been observed between doped and undoped KGW materials. This kind of measurement can be used to check the precision of the refractive index at the  $10^{-4}$  level with respect to an angular accuracy of the optic axis of  $0.01^\circ$ . A rotation of the ellipsoid around the  $\mathbf{b}$ -axis has not been observed here. The measurements of the refractive index should be performed with a better accuracy as described in the second chapter. Such measurements could eliminate every doubt on the measured values. In the case of KYW the refractive index values given in [19] are in good agreement with the measurements provided at this end of this section.

## 4.2 ABSORPTION MEASUREMENTS NEAR THE OPTIC AXIS OF $\text{Ho}^{3+}:\text{KYW}$

In this section, the absorption profile of the Holmium-doped KYW crystal near the optic axis will be shown. Those measurements are important in order to understand all different laser curves presented in the following chapter.

As KYW is a monoclinic crystal, all its properties (refractive indices, thermal expansion, absorption and emission cross sections...) depend on the considered crystal orientation [13, 15, 38, 99, 100, 23]. Furthermore, each property can be optimally described in its own eigen-frame, all these frames having in common the axis that corresponds to the direction of the monoclinic axis (**b**-axis). This is a particularity of low symmetry crystals as monoclinic crystals. That was recently extended also to the linear spectroscopic properties of absorption or emission [32]. For example, the spectroscopic properties and the associated angular distributions in polarized light have already been experimentally and fundamentally characterized in the YCOB crystal doped with Neodymium ions [101]. Such measurements are not yet available for double tungstate crystals, KYW, KLuW or KGW. Moreover, in the case of double tungstate crystals, the monoclinic axis - as discussed in Chapter 2 - is perpendicular to the plane that contains the  $N_m N_g$  plane [31]. Thus, the two optic axes are equivalent with respect to their spectroscopic properties. We performed measurements of angular distributions of absorption in polarized light near one optic axis, as well as characterization of the related laser emission (see Chapter 5), these remarkable directions showing a very high propagation and polarization sensitivity.

### 4.2.1 Experimental setup

The measurements of the absorption have been performed using a 16 mm long Holmium doped KYW crystal (1%at). A polarized home-made Thulium fiber laser was used both as a probe and pump beam at a wavelength of 1960 nm. In order to limit the impact of the CR transformation inside the crystal, a beam radius of 400  $\mu\text{m}$  was used inside the crystal. With such a big radius the pattern of conical refraction can not be observed, due to the overlapping of the conical refraction from each point of the laser beam (see Chapter 3). The crystal was cut perpendicularly to one of the optic axes. The absorption measurements have been carried out

for several orientations and polarizations in order to obtain the absorption distribution near this optic axis. The different orientations were measured by tilting the crystal in the plane corresponding to the  $N_p$ - $N_g$  plane ( $\theta$  angle), and perpendicularly ( $\phi$  angle).  $\theta$  and  $\phi$  are the angles in spherical coordinates, referring to the dielectric frame (X, Y, Z). In agreement with different denominations in literature, the dielectric axes are equivalently labelled (X, Y, Z) or ( $N_p$ ,  $N_m$ ,  $N_g$ ), respectively. Thus, principal refractive indices are equivalently labelled ( $n_x$ ,  $n_y$ ,  $n_z$ ) or ( $n_p$ ,  $n_m$ ,  $n_g$ ), respectively. In this case, these indices undergo the following relations  $n_x < n_y < n_z$  and  $n_p < n_m < n_g$ .

#### 4.2.2 Results

Figure 4.9 depicts the measurements obtained along the optic axis for two eigen polarization modes, with  $E \parallel N_m$  corresponding to the maximum of absorption and  $E \perp N_m$  the orthogonal polarization with the minimum of absorption. In Figure 4.10, more incident polarizations are shown in order to confirm that  $E \parallel N_m$  ( $E \perp N_m$ ) correspond to polarization eigen modes and thus to the maximum (minimum) of absorption. The complex absorption profile clearly shows the orientation of the optic axis (at coordinates  $\Delta\theta = 0$  and  $\Delta\phi = 0$ ,  $\Delta\theta$  and  $\Delta\phi$  being a small variation of angle  $\theta$  and  $\phi$  around the optic axis). The absorption strongly depends on the polarization and the orientation near this optic axis. The linear absorption coefficient varies from  $0.4 \text{ cm}^{-1}$  up to  $1.5 \text{ cm}^{-1}$  by changing the polarization. In similar matrices for 'classical' orientation along dielectric axes  $N_p$  (X) or  $N_g$  (Z) the polarization  $E \parallel N_m$  always exhibits higher absorption [28, 27]. It is in agreement with the measurement presented here.

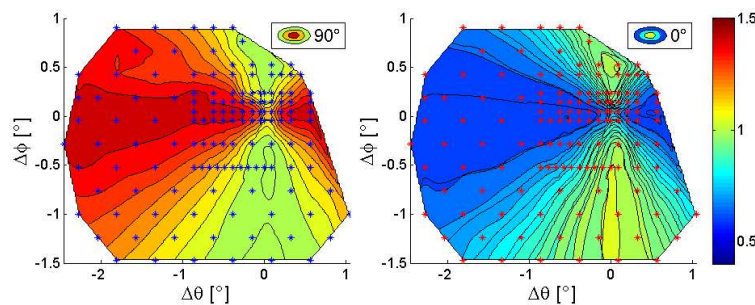


Figure 4.9 – Absorption profiles in  $\text{cm}^{-1}$  near the optic axis of a 16 mm-long Holmium-doped KYW (1%at.) crystal with a beam radius of  $400 \mu\text{m}$ .  $90^\circ$  and  $0^\circ$  corresponds to  $E \parallel N_m$  and  $E \perp N_m$ , respectively. The angles  $\Delta\theta$  and  $\Delta\phi$  are internal angles (taking into account the refraction law at the crystal entrance interface) in spherical coordinates, with respect to the optic axis direction.

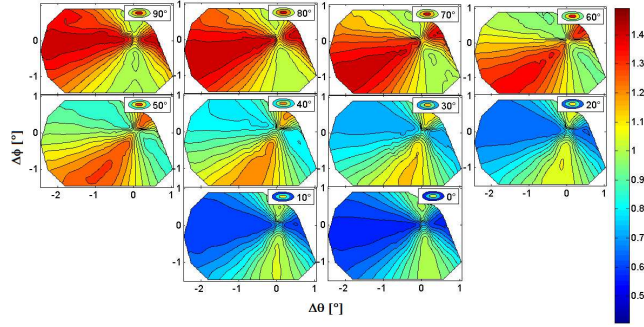


Figure 4.10 – Absorption profiles in  $\text{cm}^{-1}$  of Holmium-doped KYW (1%at.) of various incident polarizations.  $90^\circ$  and  $0^\circ$  correspond to  $E \parallel N_m$  and  $E \perp N_m$ , respectively.

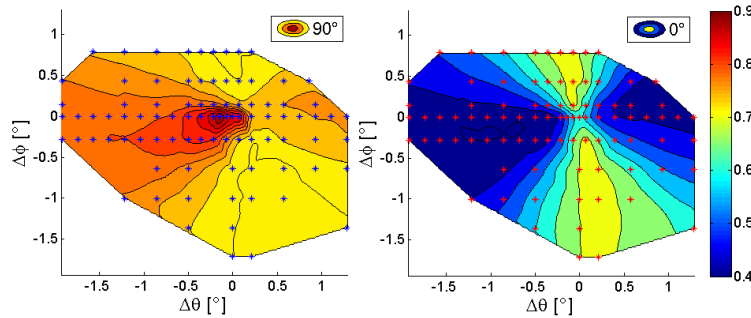


Figure 4.11 – Absorption profiles in  $\text{cm}^{-1}$  with a beam radius of  $200 \mu\text{m}$  in Holmium-doped KYW (1%at.). In this case the medium absorption transition was saturated, so the values do not directly reflect the true absorption cross sections.  $90^\circ$  and  $0^\circ$  correspond to  $E \parallel N_m$  and  $E \perp N_m$ , respectively.

The different orientations (1), (2), (3), (4) presented in Figure 4.11 correspond to directions where the laser emission has been operated, as described in the following Chapter. For positions (1) and (2), the absorption is three times higher for  $E \parallel N_m$  than for  $E \perp N_m$ . So the laser emission threshold will be much higher for  $E \perp N_m$ . In (3) and (4) the behaviour should be similar for both polarizations, whatever the polarization of the laser emission. In Figure 4.11, the medium absorption is saturated (with an incident beam radius of  $200 \mu\text{m}$ ). In this case a maximum of absorption appeared near the optic axis. This is due to the modification of the beam propagation inside the crystal caused by the conical refraction (CR) pattern. The total volume of excited region of the crystal is larger in that case. This results in a lower saturation and so in a higher absorption. This information is crucial for conical refraction lasers that always exhibit two times higher thresholds than classical lasers. This might be due to the fact that the conical mode inside the crystal has a larger area than the classical Gaussian mode.

# LASER EXPERIMENTS

# 5

## INTRODUCTION

In this chapter the laser experiments are presented, laser action along and near the optic axis. Two different crystals have been used. First, some experiments with a Neodymium-doped KGW crystal are presented. Those experiments were performed in order to check the reproductibility of the publications [77, 78]. In a second part, the case of Holmium-doped KYW crystal is presented. Finally, some new architectures are presented.

## 5.1 NEODYMIUM KGW - UNCOATED

In this section, the laser experiment performed with Neodymium-doped KGW crystals are reported. First, the crystal and the set-up are described. Secondly, the definitions of the system are performed.

### 5.1.1 Motivation

The motivation of those experiments is to check the results given in the publications [77, 78]. There, the authors report a Neodymium-doped KGW (3 at.% and 17 mm long) laser pumped with a fiber coupled diode at 808 nm with a core diameter of 100  $\mu\text{m}$ . The laser cavity is a plano-concave with a mirror having a radius of curvature of 75 mm. The cavity length was between 50 and 80 mm. Their cavity was aligned along the optic axis of the laser. They claim to have 74% slope efficiency with an output power up to 3 W for a maximum pump power of 5 W. Those impressive results have to be counterbalanced with their previous publication [79], where there had only 45% of slope efficiency with a similar set-up (and curves...). It is necessary to check those results to confirm the efficiency of such a system. Furthermore, our experiments provided know-how concerning the alignment and the sensitivity of conical refraction lasers. This know-how has been used to achieve very good performances with the Holmium-doped KYW laser presented in the next section.

### 5.1.2 Description of the experimental setup

The hemispheric cavity of the laser (see Figure 5.1) was used with several designs described in Table 5.1. These different configurations were used to modify the mode size of the laser cavity. In all those experiments, the fiber coupled pump diode was aligned with an Helium-Neon (HeNe) laser. Then the first mirror was aligned using the HeNe laser. The crystal is then aligned with the face perpendicular to the HeNe beam. Finally, the cavity was closed by aligning the back reflection of the HeNe laser. In order to obtain the laser emission, the pump power was increased and the end cavity mirror slightly adjusted. Small adjustments of the two mirrors were then performed to increase the output power. The fiber diameter of the laser pump was 400  $\mu\text{m}$  with a numerical aperture of 0.22 and the wavelength was 805 nm.

With such a method the pump beam and the laser beam are not per-

element/distance(mm)	d1	L1	d2	L2	d3	M1	d4	d5	M2
Configuration 1	30	F=30	55	F=60	20	RC=75	35	1	R=95%; RC=∞
Configuration 1b	30	F=30	55	F=60	20	RC=75	35	6	R=95%; RC=∞
Configuration 2	30	F=30	40	F=75	40	RC=1500	25	65	R=95%; RC=∞
Configuration 2b	30	F=30	40	F=75	40	RC=1500	25	165	R=95%; RC=∞

Table 5.1 – List of the different configurations used. RC=Radius of Curvature (mm), R = reflectivity, F=focal lens (mm), d = distance, L = lens and M= mirror.

fectly aligned for conical refraction. However, it was the only way to achieve laser emission with uncoated crystals.

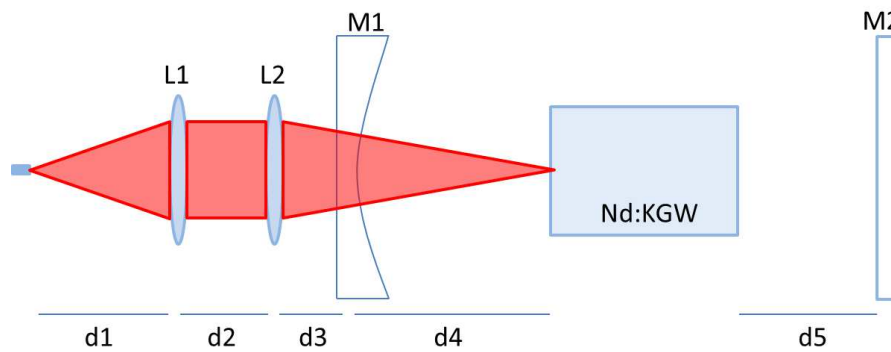


Figure 5.1 – Scheme showing the different distances within the laser setup.

### Crystals used

Two identical crystals were used for the experiments. The Neodymium-doped KGW crystals had the dimension of 4x3x11 mm. The doping concentration is unknown but we assume that it is at least 3at.% considering the absorption of the crystals. In those first experiments, the crystals did not have any anti-reflection coating. They were cut perpendicular to the optic axis for a wavelength of 633 nm with an uncertainty of 1.25 mrad. The absorption peak for the pump wavelength is at 811 nm. This corresponds to the transition  ${}^4I_{9/2} \rightarrow {}^4F_{5/2} + {}^2H_{9/2}$ . The maximum absorption is obtained for the polarization  $E \parallel N_m$  [102, 8]. The unpolarized absorption measurement of the crystal has been carried out using a Cary 5E spectrometer given in Figure 5.2. The strong absorption and the length of the samples forced to use a wide spectral aperture (5 nm) in order to collect enough light for the measurement.

The maximum emission peak of the Neodymium inside the KGW crystal is at 1067 nm. The emission cross section at this wavelength can reach  $34 \times 10^{-20} \text{ cm}^2$  [102, 8] for  $E \parallel N_m$  polarization.

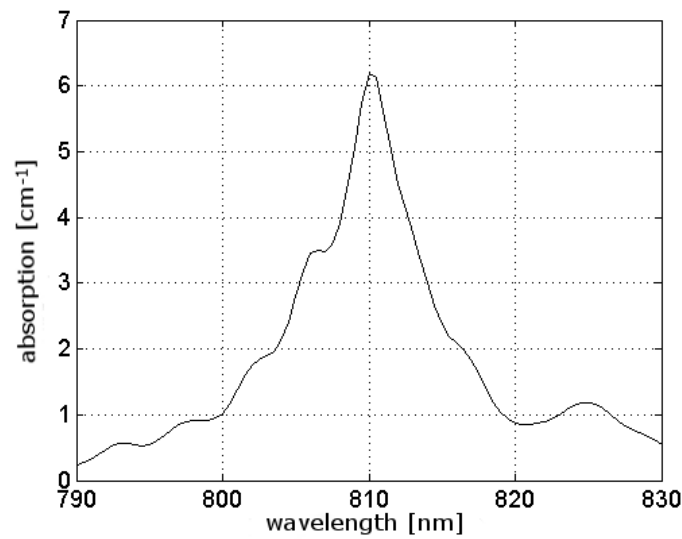


Figure 5.2 – Unpolarized linear absorption of Neodymium-doped KGW near the optic axis.

### 5.1.3 Result

The laser experiments were performed with a maximum incident pump power of 5 W. This limit has been chosen in order to avoid the fracture of the crystal. In the following section the fracture limit of this material is discussed.

The threshold and the slope efficiency for all the different configurations are given in Table 5.2. They do not exert specific behavior (higher efficiency) as published in [77] compared to classical Neodymium doped lasers using crystals cut perpendicularly to the dielectric axes.

Configuration	Threshold (W)	Slope efficiency (%)
1	1	28,0
1b	1	19,9
2	1,5	24,6
2b	1,8	16,5

Table 5.2 – Summary of the laser results for the uncoated Neodymium-doped KGW crystal. The slope efficiency is calculated with the launched pump power, which one is totally absorbed.

The low efficiency of those first experiments are due to the high loss inside the cavity since there is no anti-reflection coating on the crystals. However, it could be sufficient to check the parameters of these crystals.

The beam quality of the output beams in those different configurations

were not further investigated. They were elliptical, and so strongly multi-mode beams.

#### 5.1.4 Simulation

In order to estimate the different parameters of this material, the fitting of the laser curve has been realized using the software LASCAD. The values given with such a simulation are just an order of magnitude. This software also provides a finite elements analysis (FEA) function that allows to estimate the thermal lens parameters.

It is important to insist on the fact that those parameters are an estimation. It has been demonstrated in the previous section that most of them are not known accurately and strongly depend on the crystal orientation. Furthermore, some parameters as the pump and heating efficiency can not be measured. Those parameters can then compensate other ones.

##### Parameters used

The parameters used for those simulations are given in Table 5.3. The  $x$ ,  $y$ ,  $z$ , coordinates correspond here to the frame of the crystal cut with  $4(y) \times 3(x) \times 11(z)$  mm.

##### Simulations

The configuration 1 is simulated on Figure 5.3, experimental points are represented with triangles and the calculated ones with black circles. Two cases have been simulated. One with 20% of intra-cavity losses and the other one with the value set at 3.5%. The first one corresponds to the losses created by the reflection at the crystal face and the second one has been performed in order to fit the experimental results. The alignment method reduces the intra-cavity losses. If it is not possible to obtain laser action along the optic axis, it is just because the reflective losses are too high when the crystal is tilted inside the laser cavity (with refractive index of 2, it is almost 10% per interface). However, when the crystal is tilted for conical refraction no laser output was obtained even for 5 W of incident pump power. This can result either from wrong parameters or from the fact that the threshold of the CR laser is higher than for a classical laser [77]. In both cases, multi-modal outputs have been taken in consideration.

For the calculation of the configuration 1b presented on Figure 5.4, the intra-cavity losses have been fixed to 5%. With this calculation the comparison of the maximal possible output considering a monomode output

Pump beam		
Parameter	Value (x ; y ; z)	unity
Wavelength	805	nm
Waist radius	280	$\mu\text{m}$
Divergence	100	mrad
Super-Gaussian exponent	3	-
Cooling		
Side temperature	300	$^{\circ}\text{K}$
Initial temperature	300	$^{\circ}\text{K}$
Nd:KGW crystal CR-cut		
Thermal conductivity	2.8 ; 2.7 ; 2.9	$\times 10^{-3} \text{ W.mm}^{-1}.\text{K}^{-1}$
Expansion coefficient	5 ; 4 ; 6	$\times 10^{-6} \text{ K}^{-1}$
Elasticity module	300000	$\text{N.mm}^{-2}$
Refractive index	2.000 ; 1.986 ; 1.985	-
$\frac{dn}{dT}$	0.4 ; 0.4 ; 0.4	$\times 10^{-6} \text{ K}^{-1}$
Absorption coefficient	0.35	$\text{mm}^{-1}$
Heating efficiency	0.1	-
Emission cross section	3.4	$\times 10^{-17} \text{ mm}^2$
Fluorescence lifetime	120	$\mu\text{s}$
Pump efficiency	0.8	-

Table 5.3 – Parameters used for the simulation of Neodymium-doped KGW.

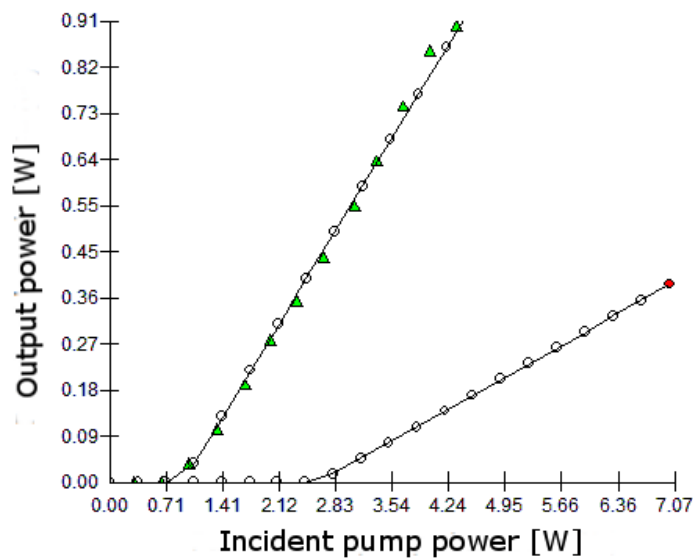


Figure 5.3 – Output power vs incident pump power, triangles are experimental points and circles calculated ones with 3.5% and 20% (for the one with the red dot) intra-cavity losses.

and a multi-modal case is performed. The multi-modal case corresponds to the measured laser output.

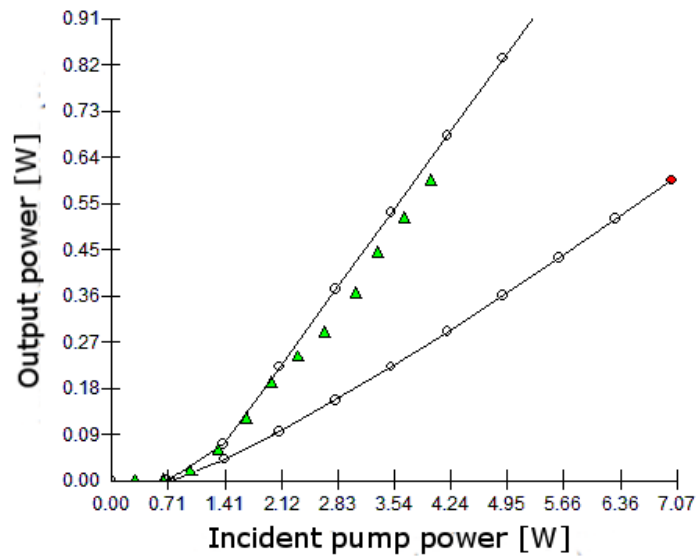


Figure 5.4 – Output power vs incident pump power, triangles are experimental points and circles calculated ones with 5% intra-cavity losses for the monomode and multimode (for the one with the red dot) cases.

In the case of the configurations 2 and 2b, the laser was very unstable. This is probably due to the strong thermal lens occurring inside the material.

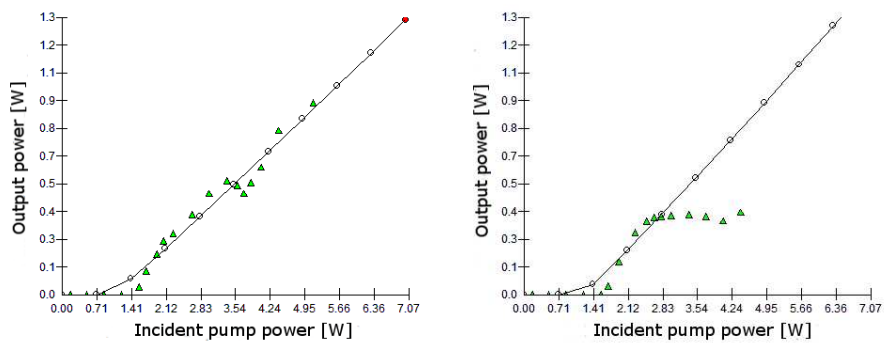


Figure 5.5 – Output power vs incident pump power in case of the configuration 2 (on the left) and 2b (on the right) : triangles are experimental results. Calculations are performed with 5% of intra-cavity losses in the monomode regime.

### Crystal fracture

The crystal fracture limit was reached by increasing the pump power. The fracture happens for an incident pump power around 8 W. The damage observed consists in a curved line of around 1.5 mm length starting from

the middle of the crystal. In order to estimate the stress inside the crystal FEA analysis was performed using LASCAD. Those simulations are carried out using the parameters present in Table 5.3. Using the FEA analysis, one can estimate the mechanical stress present inside the crystal. In this simulation the maximum mechanical stress is around 18 MPa. This is below the minimal fracture limit of around  $\sim 50$  MPa found in the literature. This can be explained by the mechanical stress added by the mounting of the crystal. The crystal is wrapped with an indium foil and then mounted inside a screwed copper mount. This way of mounting adds some mechanical stress, even if the indium is a very soft material.

### 5.1.5 Conclusion

Those first experiments provided interesting information about this material and the way of aligning the system. The really high doping concentration of those samples creates a very strong thermal effect. As those thermal effects are not homogeneously distributed along the crystal, it is difficult to estimate their impact on the laser resonator. In fact, the absorption of all the pump power occurs within few millimeters inside the crystal.

## 5.2 NEODYMIUM KGW - COATED

### 5.2.1 Motivation

In the previous experiments performed with uncoated crystals, the lasing action exactly along the optic axis was not possible. So, the crystals have been coated with an anti-reflection coating for both lasing and pump wavelength in order to reduce the intra-cavity losses. The lasing action along the optic axis should be easier. However, those experiments were still not successful. Only laser action close to the optic axis was possible.

### 5.2.2 Experimental setup

#### Crystal used

The crystal used was the same than in the previous experiment with a shorter length (4x3x8 mm) and an anti-reflection coating reducing the reflection below 0.2% for wavelengths between 800-810 nm and at 1067 nm.

element/distance(mm)	d1	L1	d2	L2	d3	M1	d4	d5	M2
Configuration 3	45	F=45	55	F=55	10	RC=75	50	-	R=95%; RC= $\infty$

Table 5.4 – Description of the configuration used with AR-coated crystal. RC=Radius of Curvature (mm), R = reflectivity, F=focal lens (mm). d = distance, L = lens and M=mirror.

### Cavity and pump

The configuration used was similar to the configuration 1. However, in order to reduce the pump mode size which was too big compared to the laser cavity in the previous experiment, a fiber with 200  $\mu\text{m}$  core diameter has been used. The configuration 3 of this cavity is described Table 5.4.

### 5.2.3 Result

The output of the laser was not impressive. Two of the laser curves are shown on Figure 5.6. Only an efficiency of 47% was reached. However, when the cavity is close to the stability limit one could see on the red curve that the thermal lens inside the crystal reduces drastically the output power.

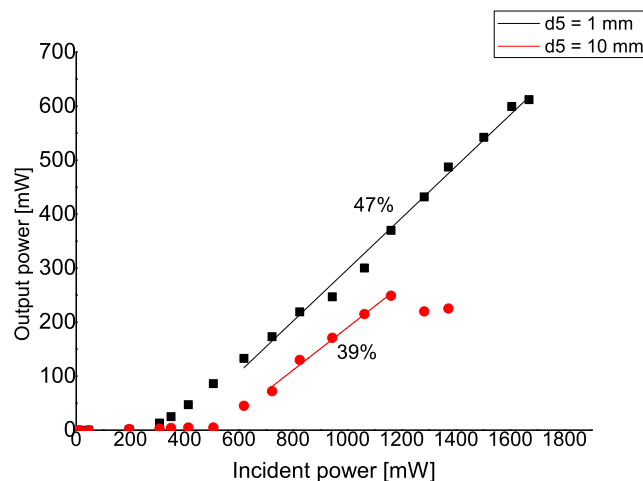


Figure 5.6 – Output power vs incident pump power using AR-coated Neodymium-doped KGW crystal.

The mode of this laser was really awful and strongly elliptical. A picture at maximum output power is shown on Figure 5.7. The ellipticity of the beam has always the same orientation depending on the crystal orientation. If the crystal is turned by  $90^\circ$  this pattern will follow. We can conclude that the ellipticity of this beam results from the anisotropy properties of the crystal.

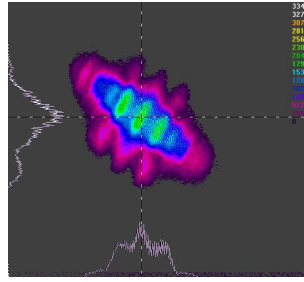


Figure 5.7 – Beam profile at the maximum output power of the Neodymium-doped KGW.

Some experiments have been done in collaboration with the IFSW in Stuttgart, as there was a setup identical to the one presented in the publication [77] with a coated crystal of 17 mm length. They were not able to obtain efficient laser action along the optic axis either with their setup. When propagating along the optic axis, the laser mode was seriously degraded and the optical output power very low. A typical mode that was possible to obtain using their system is shown on Figure 5.8. This output was strongly degraded. This occurs only when the crystal is aligned along/close the optic axis. In other orientations classical laser action was observed.

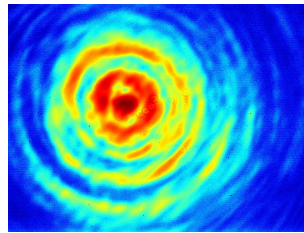


Figure 5.8 – Beam profile along the optic axis of Neodymium-doped KGW obtained at the IFSW.

#### 5.2.4 Conclusion

Those first experiments using the Neodymium-doped KGW sample cut perpendicularly to the optic axis were not successful. Too high doping concentration induced a very strong thermal lensing effect. The elliptical modes observed tend to demonstrate that the athermal direction predicted by Biswal [10], near the optic axis does not exist in this crystal. This is in agreement with the result provided by Loiko *et al.* [103]. Furthermore, no efficient laser action along the optic axis was possible. The high efficiency and good beam quality presented in the publication [77] have not been reached. The efficiency, when lasing close to the optic axis, is rather similar to the one the same authors published at a conference [79]. The result presented here being far away from the one published in [77, 78]

rises some questions about possible systematic measurement errors in the experimental results presented therein.

However, a lot of knowledge results from those experiments. First of all, the maximum tensile stress of those crystals once mounted into the cooling mount is found to be around 18 MPa. The alignment along the optic axis was critical. So for the next experiments different mounting for the crystal had to be used.

### 5.3 HOLMIUM-DOPED CR LASER

In the following the laser experiments performed with the Holmium-doped KYW crystal are presented. A description of the homemade pump laser is given. The crystals used are described. Then the different configurations of the Holmium-doped KYW crystals are shown.

#### 5.3.1 Description of the pump laser

The description of the homemade pump laser is done in this section.

A Thulium fiber laser (Figure 5.9) was build up. It consists of a 3 m long double clad fiber pumped from both sides by two fiber-coupled diodes (LIMO-HLV20) with  $400\ \mu\text{m}$  core diameter fibers and with a lasing wavelength around  $795\ \text{nm}$ . Those diodes have a maximum output power of  $20\ \text{W}$  each. The numerical aperture of the delivery fiber is  $0.22$ . The active core diameter of the thulium fiber is around  $50\ \mu\text{m}$ , and the second clad has a core diameter of  $600\ \mu\text{m}$ . The numerical aperture of the active core is  $0.08$ . The lenses used to couple the laser beam into the fiber have a focal length of  $7\ \text{mm}$  and have an anti-reflection coating for pump and lasing wavelength. The dichroic mirrors used to separate the pump and the laser wavelength were highly-transmitting for the  $2\ \mu\text{m}$  radiation, and highly-reflective for the  $795\ \text{nm}$  radiation under an incident angle of  $45^\circ$ . The output coupler of this laser is simply the end of the fiber cleaved with an angle of  $0^\circ$ . The Fresnel losses ensure the feedback. The other side of the fiber is cleaved with an angle of  $8^\circ$  in order to reduce the feedback from this side.

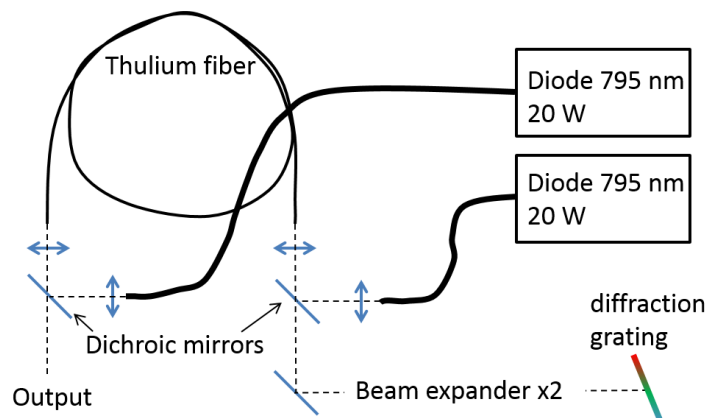


Figure 5.9 – Schematic of the thulium fiber laser.

The wavelength of this laser can be tuned by tilting the diffraction grating which is the cavity end mirror. The diffraction grating has a reflectivity slightly higher than  $70\%$  (data provided by the manufacturer).

The accordability can be obtained for a wavelength range from 1930 nm up to 2060 nm. In Figure 5.10, the measurement points are shown for the maximum output power of the laser (current intensity of the diode,  $I_{diodes} = 30\text{ A}$ , corresponding to 40 W of optical pump). A second measurement performed with another fiber at a lower output power ( $I_{diodes} = 20\text{ A}$ ) is also shown. This second fiber was strongly multimode and has not been used for pumping the Holmium-doped crystals.

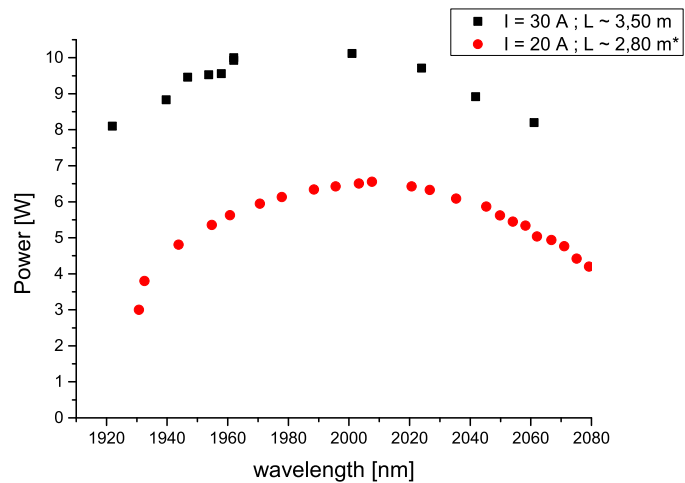


Figure 5.10 – *Accordability of the Thulium fiber laser at maximum pump power ( $I_{diodes} = 30\text{ A}$ ). \*This measurement has been performed with another fiber not described here but very similar.*

The fiber used was almost monomode. In fact the  $M^2$  of this Thulium fiber laser is around 1.3. In Figure 5.11 is shown the propagation of the output beam. The beam is circular once the laser is well aligned and stabilized.

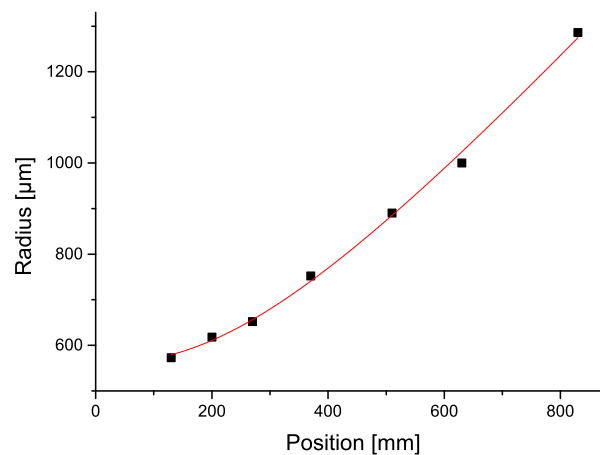


Figure 5.11 – *Beam propagation of the Thulium fiber laser at the output.*

The maximum output power obtained with this laser is 10 W for unpolarized output and 6 W for polarized output. This laser has been polarized by adding a polarizer inside the laser cavity just before the telescope. Best efficiency can be achieved in case of polarized pump power. This maximum pump power is strongly dependent on the optic alignment and the fiber cleaves quality.

### 5.3.2 Description of the crystal used

For all those experiments Holmium-doped KYW crystals have been used. The KYW matrix is available from the crystal grower. The doping concentration has been chosen to be 1%. This concentration has been chosen in order to have a spacing between the doping ions to reduce the effect of energy transfer between ions occurring at high pump power. This effect of upconversion is well known to reduce the efficiency of the laser. This value has been chosen referring to the know-how of the ISL on Holmium-doped crystals. The concentration is around  $6.38 \times 10^{-19} \text{ cm}^{-3}$ . The linear absorption at 1960 nm with this concentration varies from  $0.4 \text{ cm}^{-1}$  up to  $1.5 \text{ cm}^{-1}$  depending on the polarization and the orientation as it has been deeply discussed in the previous chapters. The crystals have a section of  $4 \times 4 \text{ mm}$  and a length of 12 mm to 20 mm. Figure 5.12 shows the percentage of the pump absorption at 1960 nm in the Holmium-doped crystal in the case of single pass. The average for both polarizations is around 60-70%. The length of the crystal is long enough to easily observe conical refraction. The conical refraction-rings radius is  $240 \mu\text{m}$  for the 12 mm long crystal and  $400 \mu\text{m}$  for the 20 mm long crystal.

One critical point for this experiment is the cutting angles of the crystals. The crystal was cut with angles  $V_{N_g} = 44^\circ$  (angle with the dielectric axis  $N_g$  in the plane  $N_g N_p$ ) and  $18^\circ$  between the crystallographic  $c$ -axis and the  $N_g$  axis. With such cutting angles the misalignment at  $2 \mu\text{m}$  with respect to the optic axis was around  $1^\circ$ . The cutting accuracy is not known, however the cutting angle difference observed between several samples varies up to 12 mrad. Figure 5.13 shows the dispersion of several crystals of KYW cut with the same angle from the same manufacturer. The orientation of the crystal is set moving the crystal with two different angles from the initial orientation of the  $b$ -axis. This method is purely mechanical and does not use any optical method in order to check the orientation before the cut of the crystals. The dispersion is so high that it is not possible to get closer to the optic axis with this cutting method. It would have been

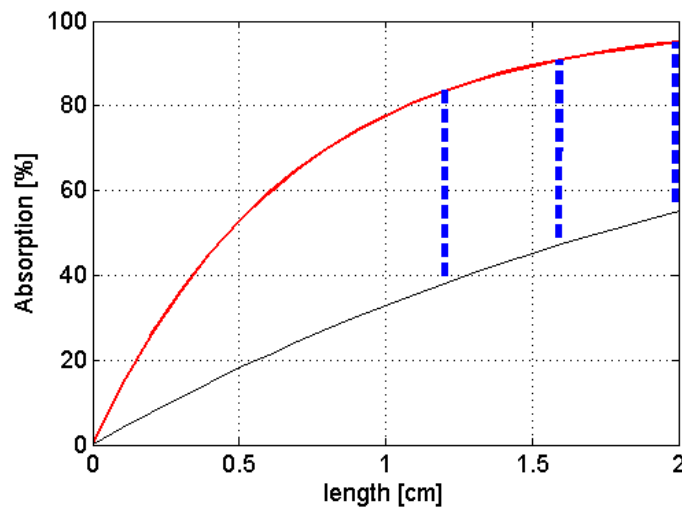


Figure 5.12 – Absorption at 1960 nm of  $\text{Ho}^{3+}:\text{KYW}$  (1at%) for different lengths near the optic axis. The maximum (red) is for  $E \parallel N_m$  polarization and the other (black for  $E \perp N_m$ ). The dashed blue lines correspond to the available crystal lengths.

possible to check the orientation of those crystals using the X-ray as it has been done in Chapter 3. However, the precision of the setup is not better than  $1^\circ$ , and so would not have been a useful measurement. The only way to obtain a better cut is to introduce an optical system checking the crystal orientation before the crystal cut.

This small misalignment with respect to the optic axis of the crystal cut orientation slightly complicates the alignment of the laser cavity along this optic axis.

### 5.3.3 Motivation

This laser was build in order to check the possibility of realizing a conical refraction laser with a quasi-three-level medium. Such a laser has an unknown resonance condition. Furthermore, in the case of quasi-three-level systems the reabsorption plays an important role on the laser action. Even if the previous experiments with Neodymium-doped KGW were not successful, it is still interesting to investigate the conical refraction effect using crystals with lower doping concentration. As it has been shown in previous chapters the absorption properties strongly vary with the orientation and the polarization. This has a drastic influence on the laser performance. Different laser orientations are tested in the following. However, a description of several conical refraction lasers is done in the next section in order to characterize several possible setups.

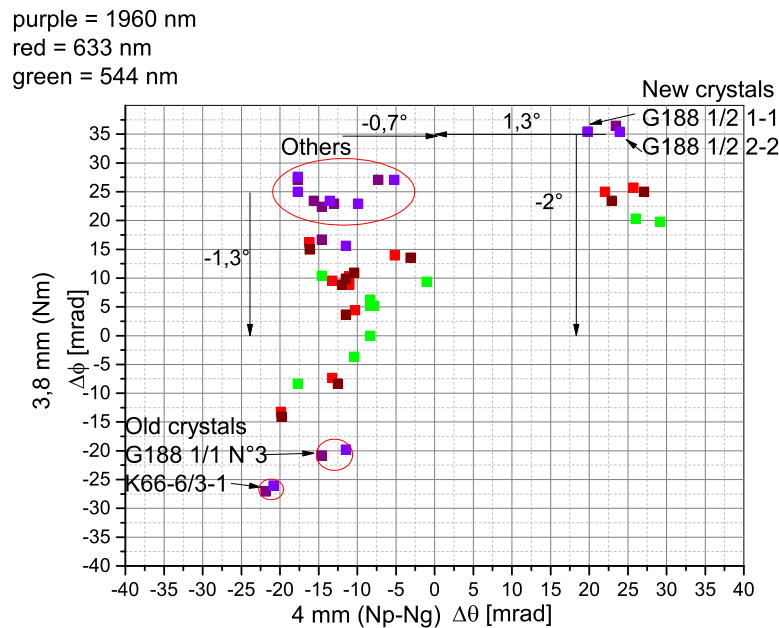


Figure 5.13 – Dispersion of several crystal cuts. The old crystals have been cut with the angle described in the text. New crystals were an unsuccessful tentative to correct the cutting angles. The coordinate (0,0) corresponds to an incident angle of  $90^\circ$ . The measurements are given with an uncertainty of 3 mrad.

### 5.3.4 CR laser: which configuration ?

The conical refraction has been described in the Chapter 3 of this thesis. The propagation of the light inside the crystal is not easy to apprehend. The main question in the case of laser resonators is which kind of mode can result from a CR resonator? What are the different possible parameters ?

Using a simple scheme as presented in Figures 5.14, 5.15, 5.16, 5.17 different possible modes can be expected. In Figure 5.14 a hemispherical cavity is represented with a biaxial crystal aligned for conical refraction inside the cavity. The ideal case would be to have the reflection coating on one side of the crystal to replace the plane mirror. If the output coupler is the concave mirror the output beam will be Gaussian. If it is the plane mirror the output beam will be conically refracted. This case is simple to understand.

However, if there is a space between the crystal and the plane mirror, as presented in Figure 5.15, the transverse mode will not be easy to determine since the conical refraction propagation is not invariant as a Gaussian beam. The mode inside such a cavity is then difficult to predict. That is why the configuration of the laser described in the next section will follow the scheme of Figure 5.14.

In order to choose the cavity parameter such as the length and the radius of curvature of the mirror we will simply use the classical Gaussian resonator theory in order to set the waist of the incident beam on the crystal. Of course the conical refraction pattern will strongly depend on the size of this Gaussian incident beam.

Why should the conical refraction occur towards the plane mirror ? In fact, it is possible to obtain the conical refraction towards the concave mirror like it is represented in Figure 5.16. However, like in the previous case the conical refraction pattern will propagate through air leading to a difficult interpretation of the mode.

In the experiment presented in the next section the orientation of the conical refraction pattern will be set by the pump since the crystal is longitudinally pumped from one side. The pump is then conically refracted.

It is also possible to use the external conical refraction in order to obtain a CR laser as described in Figure 5.17. In this case, the crystal has to be aligned along the biradial axis and not along the classic optic axis. This case is discussed further below.

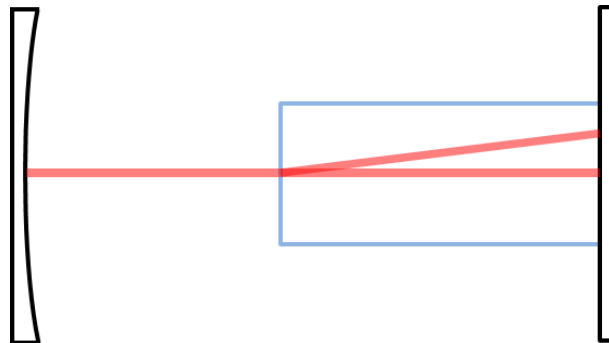


Figure 5.14 – Schematic of a CR laser with a hemispherical cavity. In this case the CR is refracting towards the plane mirror.

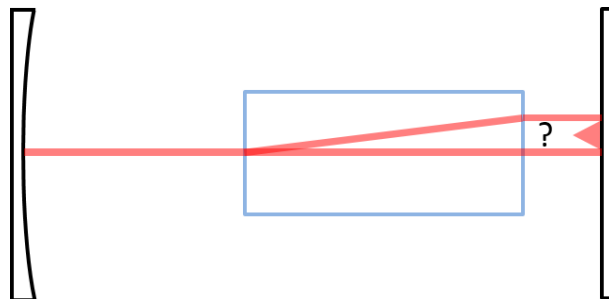


Figure 5.15 – Schematic of a CR laser with a hemispherical cavity. In this case the CR is refracting towards the plane mirror with space between the crystal and the mirror.

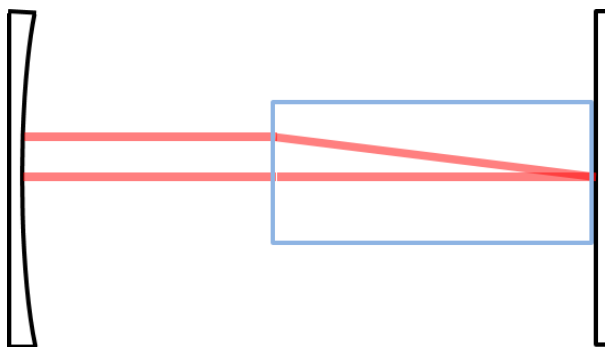


Figure 5.16 – Schematic of a CR laser with a hemispherical cavity. In this case the CR is refracting towards the concave mirror.

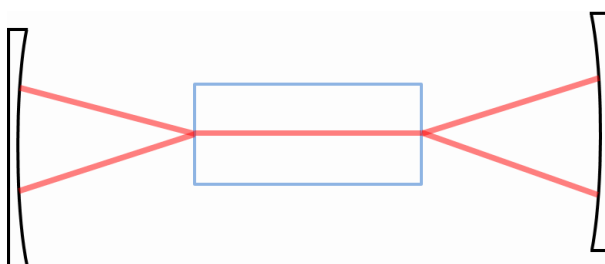


Figure 5.17 – Schematic of an ECR laser with a spherical cavity. In this case the CR is refracting towards the plane mirror with space between the crystal and the mirror.

### 5.3.5 Almost hemispherical CR laser experiments

In this section, the laser results of Holmium-doped KYW crystals cut perpendicularly to the optic axis inside an almost hemispherical cavity are presented. Different orientations have been tested in order to check the influence of the spectroscopic properties of the crystal. The cavity is almost hemispherical, that means that both mirrors are spherical but one has a bigger radius. This results in a cavity minimum waist close to this mirror like in hemispherical cavities. This type of cavity is easier to align for these experiments than a true hemispherical cavity.

#### Experimental setup

The pump in these experiments was the same laser as in the previous sections for the absorption measurements. The maximum output power was around 6 W after a Glan-Taylor prism in order to obtain a linearly polarized beam. The setup is shown in Figure 5.18. This hemispheric cavity had a spherical mirror with a radius of curvature of 91 mm. The total length of the cavity was around 6-8 cm, with the crystal as close as possible from the almost plane mirror (radius of curvature of 500 mm). The plane mirror was partially reflective for both lasing and pump wavelengths. When the entrance mirror was a dichroic mirror.

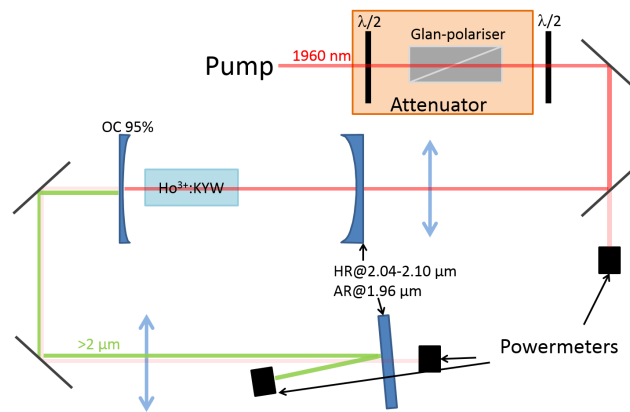


Figure 5.18 – Laser setup showing the linear cavity. OC: Output coupler, RC: Radius of Curvature.

## Results

Figure 5.19 shows the results for lasing operation for several orientations and polarizations with respect to the incident pump power. All the measurements are limited by the available pump source. Three main behaviours are clearly visible: Best results were obtained on orientation (1) and (2) for  $E \parallel N_m$ , and worst ones for  $E \perp N_m$ . This difference of lasing threshold (more than 2 times higher) is in agreement with the absorption measurements shown in the previous section. Furthermore, for  $E \perp N_m$  and only in this orientation the lasing wavelength was at  $2.056 \mu\text{m}$ . For all other orientations and polarizations the lasing wavelength was at  $2.074 \mu\text{m}$ . On orientation (3) and (4) the lasing thresholds are in between lasing operation obtained for (1) for  $E \parallel N_m$  and  $E \perp N_m$  polarizations. This is still in agreement with the absorption profile. Rotating the polarization of  $45^\circ$  along (3) and (4) allows a better efficiency of the laser, simply because in this polarization, we obtain only one refracted spot. In fact, near the singularity the pump polarization leads to only one refracted spot which is rotating like the polarization pattern of conical refraction [104]. This polarization pattern corresponds to the one on Figure 2.15. It also corresponds to how one should turn the polarization in order to directly measure the imaginary part of  $\bar{n}^-$  plotted on Figure 2.14.

As the absorption is significantly different with respect to the orientation, we performed other measurements taking into account the real absorbed pump power. For this purpose we estimated the absorbed pump power by measuring the 5% of the residual pump power which was passing through the output coupler. Those measurements are depicted on Figure 5.20. In that case, all curves give similar thresholds around  $0.70 \text{ W}$ ,

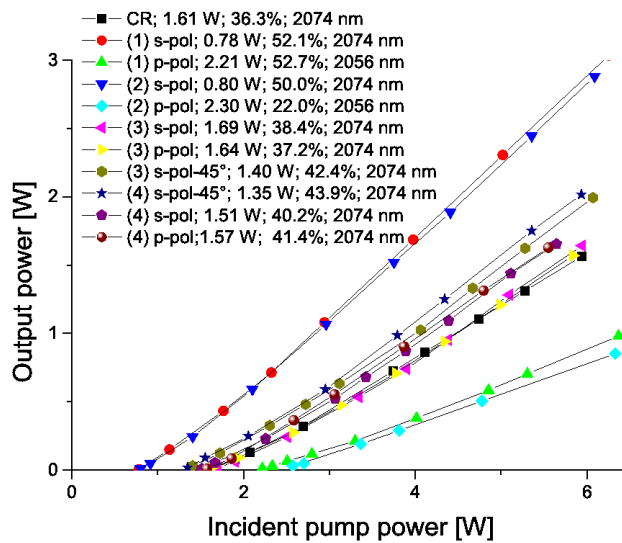


Figure 5.19 – Output power vs incident pump power along different orientations (see Figure 4.11). In the legend are written as following: orientation; polarization (s-pol (p-pol) corresponding to  $E \parallel N_m$  ( $E \perp N_m$ )); threshold; slope efficiency; lasing wavelength.

except for the CR orientation where the threshold is around 1.3 W. As the maximum pump power available was lower than in our previous results, the maximum output power was also lower. The maximum slope efficiency of 74% has been achieved for the orientation (4). The maximum output power for the orientations (3) and (4) was obtained for a polarization state close to  $45^\circ$  from  $E \parallel N_m$  as expected. Along the optic axis, a slope efficiency of 52% has been achieved with respect to the absorbed pump power.

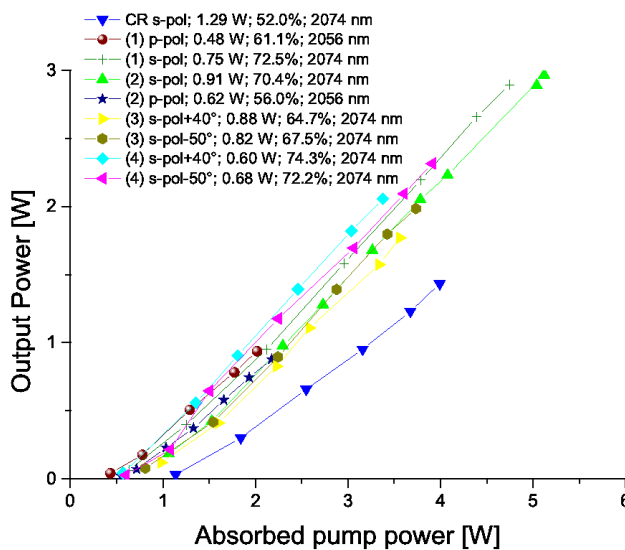


Figure 5.20 – Output power vs absorbed pump power along different orientations (see Figure 4.11). In the legend are written as following: orientation; polarization (s-pol (p-pol) corresponding to  $E \parallel N_m$  ( $E \perp N_m$ )); threshold; slope efficiency; lasing wavelength.

The output beam was Gaussian and had an  $M^2$  close to 1 for an orientation along (1) at full power. Thermal lensing was not observable, as the thermal load inside the crystal was too low. For CR-oriented crystal the  $M^2$  can not be measured since the output mode was not Gaussian (see Figure 5.21).

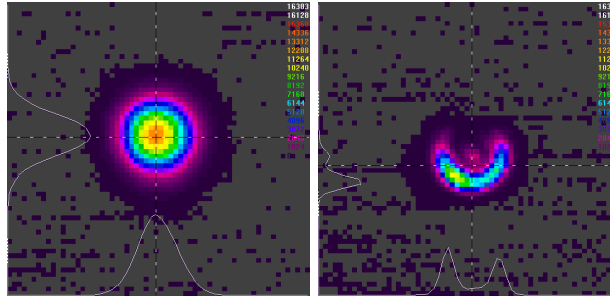


Figure 5.21 – On the left: far field output of the Gaussian laser. On the right: CR laser output close to the focal plane of a 300 mm lens.

### Discussion

It results from those experiments that the strong variation of the optical properties near the optic axis of monoclinic crystals lead to important variations of the laser efficiency. Those different behaviors can be easily understood when compared with the absorption measurement performed in the previous chapter.

Concerning the laser action along the optic axis, it will always be with a lower efficiency than the maximum possible for a classical Gaussian beam near the optic axis. This is due to the fact that even for one linear polarization the light is refracted along different orientations and so exert different spectroscopic parameter values.

So such a laser can not be more efficient than a classical Gaussian laser using the same crystal cut along the maximum absorption direction.

Furthermore, the alignment of the crystal and the cavity is much more sensitive than for classical Gaussian lasers. It exists a gap between the Gaussian regime and the CR regime where there is no laser action possible. The size of this gap depends on the incident pump power. For this experiment, it was around 10 mrad around the optic axis orientation.

### 5.3.6 ECR laser

In this section a new architecture is presented. This laser setup is using the External Conical Refraction (ECR). The motivation is explained before the experimental setup description.

### Motivation

In the previous experiments, the conical refraction was happening inside the crystal for both pump and lasing wavelength. The internal conical refraction induces different properties for each polarization state as the beam expands inside the crystal. Both of these effects tend to decrease the efficiency of the CR laser. In fact, the optical properties for an unpolarized beam along the optic axis are the mean of the values obtained for the two eigen-state polarizations. Furthermore, the beam expansion inside the crystals tends to lower the optical density of the pump. That is why a conical refraction laser will always have a higher pump threshold and a lower efficiency than a classical Gaussian laser as it has been proved in the previous section.

A way to avoid those two effects is to use the External Conical Refraction. If a conically refracted light is focused at the crystal entrance along the biradial axis (this axis is separated from the optic axis  $y$  by the angle  $A$ ), then the light will propagate along this axis.

### Description

If the conically refracted light is focused with an angle corresponding to  $2A$ , the propagation inside the crystal should have its original properties (the same properties it has before being conically refracted). Of course, the orientation of the crystal is important. In order to obtain the conically refracted light a biaxial crystal will be used. The second crystal should have the same orientation or being tilted by  $180^\circ$  depending on the number of lenses used to adjust the beam. If the second crystal is not well oriented the beam will diverge inside the crystal (totally or partially).

The experimental setup tested is presented in Figure 5.22. The pump beam is refracted by a 20 mm long undoped KYW crystal. For this purpose two lenses of 75 mm focal length are used. The second lens position is adjusted to image the CR rings on the third lens used to focus the CR beam to the 20 mm long Holmium-doped KYW crystal facet. The distance between the second and the third lens was adjusted to have a ring diameter of 5 mm at the third lens. The ring is focused with an angle close to  $2A$  with such an arrangement.

The laser cavity was composed of two concave mirrors. The distances between the mirror and the crystal were close to their radius of curvature. This is done in order to ensure that the rings resulting from the ECR are focused inside the crystal after their reflection. This ensures a resonance



order modes like in classical Gaussian lasers. The crescent shape corresponds to the polarization  $E \parallel N_m$ . The higher order modes have an increasing number of dots.



Figure 5.23 – ECR laser beam profiles. Those modes can be observed using a lens after the output coupler to image the “rings” on the camera. On the left, the lower order mode observed. On the right, higher order modes.

### Discussion

This experiment is a proof of principle that shows the possibility of having laser action using the ECR. Those results are the first experiment performed using the ECR. Of course, the laser efficiency was not important. This comes from several points, that need to be improved. First of all the pump beam was diverging inside the Holmium-doped KYW crystal. The angle of the incident pump beam was not perfect. Secondly, the cavity mirrors were not on translation stages. The position adjustment of these mirrors can help to improve the cavity alignment and stability and last but not least, having a shorter radius of curvature on the concave mirror could reduce the alignment difficulty.

Furthermore, the conically refracted output of the laser is not a convenient beam to work with.

However, the real interest of this setup is the pump scheme. In fact, if by using the ECR the divergence of the pump inside the crystal can be reduced, then longer crystals can be used without using the total internal refraction. If the dispersion of the optic axis between the pump and lasing wavelength is important, the lasing wavelength can resonate with a Gaussian mode while the crystal is pumped using the external conical refraction. This is the interest of such a setup.

# CONCLUSION AND PERSPECTIVE

This thesis is a first step to new innovative laser experiments. The aim at the beginning of this work was to check the veracity of recent publications and try to get advantage of the effect of conical refraction in order to reduce the influence of the thermal lens inside the laser medium. The historical background of this interesting study lead us to perform different investigations. The research of an athermal orientation in the monoclinic double tungstates lead Biswal *et al.* [10] to propose an orientation close to the optic axis. This orientation has then been tested by Hellström *et al.* [76] using Ytterbium-doped KGW. They were not able to prove that this orientation was athermal, but they discovered polarization dependency of their laser by moving the output coupler. Few years later two publications presented impressive laser performances along the optic axis of Neodymium-doped KGW [79, 78]. This thesis demonstrates that their work were not reproducible and probably erroneous.

The optical properties of the monoclinic double tungstates have been deeply investigated. The complex absorption orientation and polarization dependency of the Holmium-doped KYW have been performed. A simple model predicting these properties is provided. This investigation on the absorption properties gives a thorough understanding of the laser behavior. The demonstration of the drastic influence of the crystal orientation on the laser efficiency using biaxial crystals cut for a propagation along the optic axis have been performed. Laser action close to the optic axis with very good beam quality of the Holmium-doped KYW crystal was achieved. A slope efficiency up to 74% was achieved. No thermal effects were observed since the pump power available was not sufficient to induce thermal stress.

New innovative laser architecture has been tested. It results from this study that the conical refraction can be used to obtain new pumping schemes. The proof of principle has been provided in this thesis. The demonstration of the first laser using the external conical refraction has been performed. An output power of 800 mW was reached with the setup. The efficiency of the system can still be greatly improved by improving the

pump injection inside the crystals and using a smaller cavity. The benefit of such system has still to be proved compared to other laser setups, since it really needs accurate settings. Furthermore, the external conical refraction has to be tested with low quality beams provided by classical fiber coupled diodes. The use of the external conical refraction can be of great interest if it can help to reduce the divergence inside the pumped crystal. This investigation needs the use of crystals with larger aperture.

The conical refraction was a really interesting effect to study. I hope that the work presented in this thesis will be followed and will lead to new ways of building laser resonators.

ANNEXES



# ANNEXES

# A



## A.1 RÉSUMÉ EN FRANÇAIS

Nous nous sommes intéressés durant cette thèse à l'étude des cristaux monocliniques pour la réalisation de lasers à solides. Ces cristaux biaxes possèdent des propriétés physiques dépendant de l'orientation et des propriétés optiques dépendant de l'orientation ainsi que de la polarisation. Les cristaux étudiés sont des cristaux de la famille des doubles tungstates. Nous nous sommes focalisés sur des cristaux de  $\text{KGd}(\text{WO}_4)_2$  (KGW) et  $\text{KY}(\text{WO}_4)_2$  (KYW). Ces derniers sont déjà utilisés en tant que milieu amplificateur dans des lasers. Leur principal avantage réside dans de larges spectres d'émission pour les ions incorporés dans ces matrices. Cette propriété est utile pour l'obtention d'un régime femtoseconde, ce qui est la principale utilisation actuelle de ces cristaux. Les propriétés thermiques de ce cristal sont moindres comparées à celles d'un cristal de YAG mais elles restent cependant correctes. La principale difficulté avec l'utilisation de ces cristaux réside dans la anisotropie des propriétés physiques suivant l'orientation du cristal. Ainsi, pour obtenir un rendement laser optimal l'orientation du cristal doit être soigneusement étudiée en fonction des propriétés optiques du matériau. Cependant pour ces orientations les propriétés thermiques et mécaniques entraînent des effets indésirables lors de l'échauffement du matériau survenant avec une forte intensité de pompage. Une lentille thermique asymétrique se crée dégradant ainsi les performances du laser sans compensation de ces effets. Ainsi plusieurs travaux ont porté sur la recherche d'une direction dite "athermique" dans ces cristaux [10]. Dans cette hypothèse, l'orientation du cristal n'est pas choisie pour ses propriétés optiques mais pour ses propriétés thermiques et mécaniques afin de réduire l'asymétrie de la lentille thermique. Une des orientations proposées se situe proche de l'axe optique. Plusieurs groupes ont ainsi testé cette orientation avec des cristaux de KGW dopés avec de l'Ytterbium et du Néodyme. Au final, les résultats sont mitigés quant à l'intérêt de cette orientation pour diminuer l'effet de la lentille thermique. Les travaux de ces groupes ne permettant pas de comprendre en profondeur les résultats obtenus, cette présente thèse a pour vocation d'approfondir ce point. Pour comprendre les différents rendements lasers obtenus aux alentours de l'axe optique, il faut s'intéresser au lien entre la polarisation et les propriétés optiques. Pour débiter, il était nécessaire de connaître l'orientation de coupe des cristaux. Pour déterminer cette orientation, les indices de réfraction du matériau sont utilisés. Nous avons découvert que ces indices n'étaient pas connus avec suffisamment de pré-

cision pour déterminer cette orientation au degré près pour des longueurs d'onde de  $2 \mu\text{m}$ . Nous avons donc mesuré la dispersion de l'axe optique. Ces mesurent sont présentes sur la Figure A.1. L'angle  $V$  étant l'angle entre l'axe dielectrique du plus grand indice de réfraction et l'axe optique.

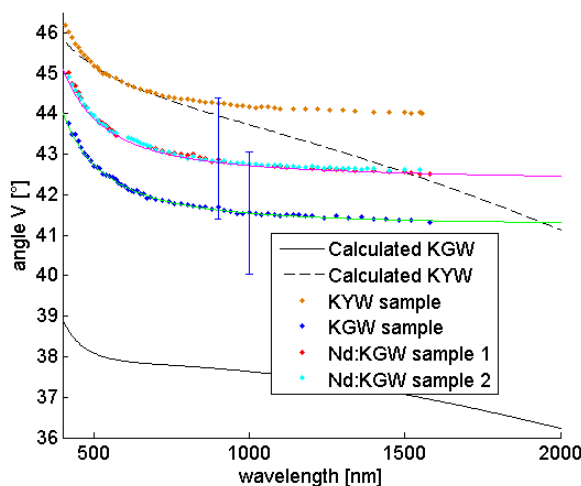


Figure A.1 – Dispersion de l'angle  $V$  (Valeurs calculées 1 et 2: avec l'équation de Sellmeier de Pujol et al. [13] et de Konstantinova et al. [21], respectivement, mesures de la variation de l'angle  $V$  référencé à  $43.3^\circ$  et  $42.1^\circ$  à  $630 \text{ nm}$  pour  $\text{Nd}^{3+}:\text{KGW}$  et le KGW non dopé, respectivement; les courbes vertes et roses sont caculées en utilisant l'indice de réfraction  $n_z$  modifié).

Nous constatons ainsi que la dispersion réelle et celle calculée avec les indices de réfraction sont très différentes. Ces mesures sont à prendre avec précaution étant donnée l'incertitude sur l'angle de coupe original des cristaux mesurés par diffraction atomique de plus d'un degré. Par ailleurs, cette dispersion semble ne pas montrer de rotation autour de l'axe de symétrie de ces cristaux monocliniques. Or des mesures effectuées sur d'autres cristaux monocliniques mettent en évidence une rotation de l'ellipsoïde des indices autour de cet axe [105]. Par conséquent il reste possible que la dispersion mesurée ne soit en fait qu'une rotation de l'ellipsoïde des indices. Cependant, cela est peu probable car cela entrerait en contradiction avec les mesures de diffraction aux rayons X. Une fois les cristaux disponibles avec une erreur de coupe d'environ un degré, des mesures d'absorption aux alentours de l'axe optique ont été réalisées en fonction de l'orientation ainsi que de la polarisation pour des cristaux de KYW dopés Holmium. Ces résultats présent sur la Figure A.2, illustrent parfaitement la complexité des propriétés optiques près de l'axe optique. Les variations dépendent bien évidemment de la polarisation ainsi que de

l'orientation, ces deux paramètres étant intimement liés à l'approche de cette singularité.

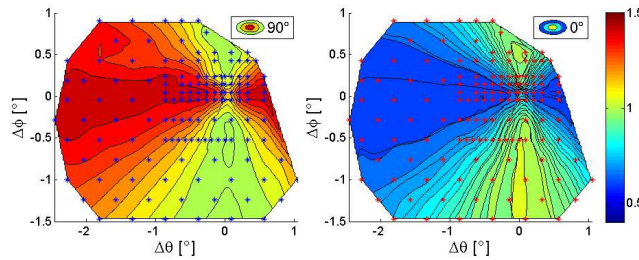


Figure A.2 – Absorption en  $\text{cm}^{-1}$  près de l'axe optique pour un cristal de 16 mm de long de KYW dopé Holmium (1%at.) pour un faisceau incident de  $400 \mu\text{m}$  de rayon.  $90^\circ$  et  $0^\circ$  correspondent to  $E \parallel N_m$  and  $E \perp N_m$ , respectivement. Les angles  $\Delta\theta$  et  $\Delta\phi$  sont des angles internes (prenant en compte la réfraction à l'intérieur du cristal) en coordonnées sphériques, avec pour origine l'axe optique.

Avec ces mesures, les différentes efficacités du laser avec un régime de fonctionnement aux alentours de l'axe optique deviennent très compréhensibles. On comprend que de part et d'autre de l'axe pour une même polarisation, l'absorption est identique. Dans notre cas, il existe une polarisation où l'absorption est beaucoup plus efficace. Il est à noter que dans ces mesures, seuls les points compris sur l'axe des abscisses sont issus de modes propres de propagations, c'est-à-dire que tous les autres points de mesures correspondent à un mélange des deux modes propres de propagation. Pour obtenir une mesure représentant l'absorption d'un mode propre en fonction de l'orientation, il faudrait tourner la polarisation du faisceau incident en fonction de l'orientation. Par ailleurs, il est à noter que lorsque la direction de propagation d'un faisceau lumineux est parfaitement alignée avec l'axe optique un effet appelé "réfraction conique" se produit. La réfraction d'un faisceau lumineux le long de cet axe produit un anneau en sortie du cristal. Ceci modifie complètement le mode laser en se propageant dans la cavité et ces effets restent peu étudiés. L'utilisation de cet effet en cavité laser a déjà été démontrée [79, 78]. Le but de cette thèse fut dans un premier temps, de confirmer ces résultats. Ainsi, nous avons utilisé des cristaux de  $\text{KGd}(\text{WO}_4)_2$  (KGW) dopés au Néodyme. Les premiers résultats furent décevants. La stabilité, la qualité de faisceau ainsi que l'efficacité étaient plus que médiocres. L'efficacité maximale obtenue fut d'environ 40 % contre 74 % dans la publication de Abdovland *et al.* [77]. La Figure A.3 montre mes meilleurs résultats avec la représentation du mode laser sur la Figure A.4.

Le faisceau de sortie présentait un profil elliptique indiquant la

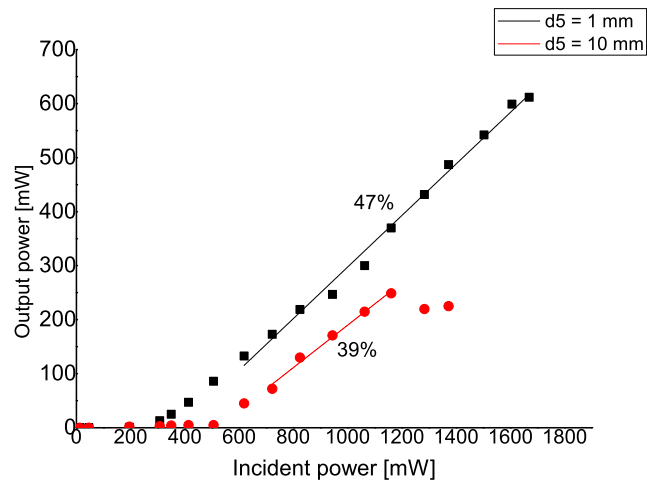


Figure A.3 – Puissance de sortie en fonction de la puissance de pompe incidente pour un cristal de  $\text{Nd}^{3+}:\text{KGW}$  avec traitement anti-reflet.

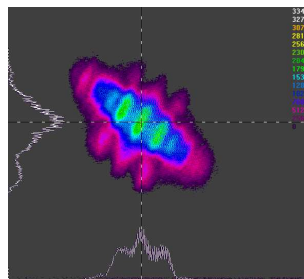


Figure A.4 – Mode laser obtenu avec la puissance de sortie maximale.

présence d'une lentille thermique avec un fort astigmatisme. (Ainsi, cette orientation qui devrait être proche d'une direction athermal (ne présentant pas d'astigmatisme) selon Biswal [10] ne l'est pas dans une cavité laser pour ce cristal ( $\text{Nd}^{3+}:\text{KGW}$  dopé à 3at.%)). De plus ce laser étant très peu stable et difficile à aligner avec des fluctuations importantes de l'efficacité, celles-ci ont amené une interrogation quant à la dépendance des propriétés optiques aux alentours de l'axe optique, thème succinctement présenté au début de ce résumé. Les résultats de cette étude montrent que ces propriétés varient non seulement suivant la polarisation mais également en fonction de l'orientation aux alentours de l'axe optique. Les dépendances en orientation et polarisation sont liées étant donné que l'état de polarisation autour de l'axe optique varie avec l'orientation. C'est pourquoi une étude simple de la réfraction est fournie afin de comprendre cette dépendance complexe. La dépendance de l'absorption aux alentours de l'axe optique a pu être simulée pour la première fois. La Figure A.5 montrent les rapides variations en fonction de l'orientation du cristal (les angles correspondent à l'inclinaison du cristal par rapport à l'axe optique.).

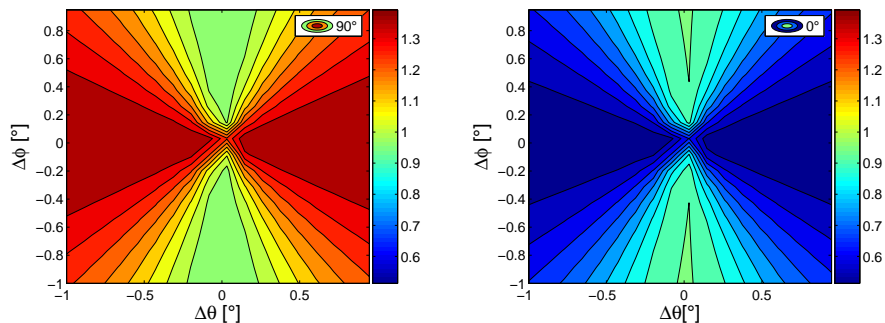


Figure A.5 – Simulation de l'absorption en  $\text{cm}^{-1}$  aux alentours de l'axe optique d'un cristal de  $\text{KYW}$  dopé avec de l'Holmium (1%at.) avec une résolution de 2 mrad.  $90^\circ$  et  $0^\circ$  correspondent à  $E \parallel N_m$  et  $E \perp N_m$ , respectivement.

Après les premières expérimentations laser, le cas de cristaux de  $\text{KY}(\text{WO}_4)_2$  ( $\text{KYW}$ ) dopés Holmium pour une émission laser à  $2 \mu\text{m}$  a été étudié. L'Holmium, ayant un faible « défaut quantique » entre la longueur d'onde de pompe (1960 nm) et la longueur d'émission (2074 nm), permet d'avoir une longueur d'onde de pompe et d'émission proches ce qui réduit ainsi la dispersion potentielle de l'axe optique entre ces deux longueurs d'onde. Grâce à un montage amélioré par rapport aux premières expériences effectuées avec les cristaux  $\text{KGW}$  dopés au Néodyme, la dépendance de la polarisation ainsi que de l'orientation a pu être mise en évidence. Différents rendements ont pu être atteints en fonction de l'orientation du

cristal. La Figure A.6 résume les efficacités obtenues suivant différentes orientations.

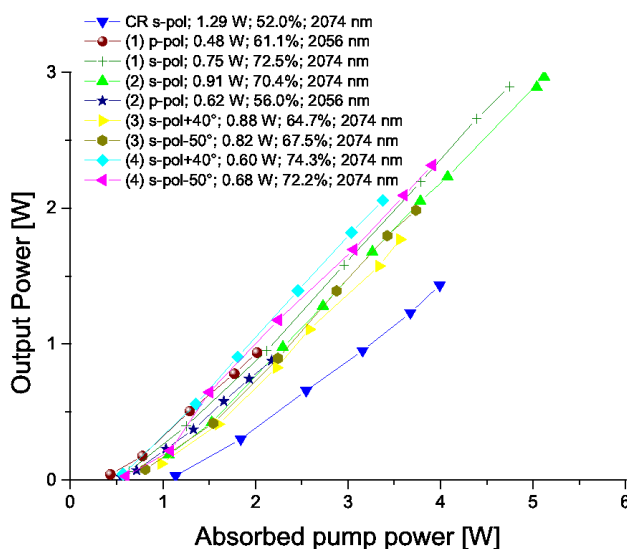


Figure A.6 – Puissance de sortie vs puissance de pompe absorbée suivant différentes orientations (voir Figure 4.11). La légende donne: l'orientation; la polarisation s-pol (p-pol) correspond à  $E \parallel N_m$  ( $E \perp N_m$ ); le seuil; la pente; longueur d'onde laser.

Une efficacité atteignant jusqu'à 70 % pour une puissance de sortie d'environ 3 W a pu être obtenue pour une orientation proche de l'axe optique. Cela représente à l'heure actuelle la meilleure performance pour cette famille de cristaux. Le taux de dopage des cristaux de KYW dopés à l'Holmium étant plus approprié au fonctionnement à forte puissance, l'astigmatisme dû à la lentille thermique n'a pas été observé. Par ailleurs, l'alignement de la cavité laser avec l'axe optique a pu être réalisé. Ainsi, nous avons prouvé qu'un mode laser « conique » est possible dans une cavité conçue pour des faisceaux Gaussiens (Figure A.7).

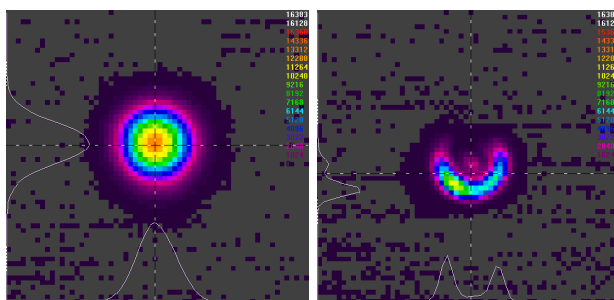


Figure A.7 – A gauche: champ lointain. A droite: proche du plan focale d'une lentille de 300 mm.

Cependant, la dépendance des propriétés optiques selon l'orientation entraîne de facto une efficacité moindre qu'un mode Gaussien classique. Des efficacités atteignant presque 50 % ont pu être obtenues suivant cette

orientation. Aucun problème de lentille thermique n'a pu être observé avec une puissance de pompe maximale de 6 W. Le taux de dopage faible ainsi que la longueur de plus de 1 cm des cristaux permettent une bonne répartition de la charge thermique dans le cristal. Enfin, un montage innovant a été testé afin d'utiliser la réfraction conique. La puissance de sortie ainsi que l'efficacité de ce montage étaient très faibles, environ 800 mW en sortie pour 4 W de puissance de pompe. Cette thèse a permis de décrire en détail les propriétés optiques des cristaux monocliniques avec le cas particulier des doubles tungstates. Avec ces connaissances, d'excellentes performances ont pu être obtenues pour une émission laser à  $2 \mu\text{m}$  avec un cristal de  $\text{Ho}^{3+}:\text{KYW}$ . Par ailleurs, nous avons réussi à faire fonctionner une cavité sur un mode de réfraction conique avec un rendement honorable de 50%. Nous avons ainsi prouvé qu'un mode "conique" pouvait résonner dans une cavité laser conçu avec des miroirs sphériques.



# BIBLIOGRAPHY

- [1] M. Eichhorn. *Laser Physics: From Principles to Practical Work in the Lab*. Graduate Texts in Physics. Springer, 2014. (Cité page 7.)
- [2] R.L. Nowack. A tale of two beams: an elementary overview of Gaussian beams and Bessel beams. *Studia Geophysica et Geodaetica*, 56(2):355–372, 2012. (Cité page 12.)
- [3] D. McGloin and K. Dholakia. Bessel beams: diffraction in a new light. *Contemporary Physics*, 46(1):15–28, 2005. (Cité page 12.)
- [4] P. Pääkkönen and J. Turunen. Resonators with Bessel–Gauss modes. *Optics communications*, 156(4):359–366, 1998. (Cité page 13.)
- [5] A.N. Khilo, E.G. Katranji, and A.A. Ryzhevich. Axicon-based Bessel resonator: analytical description and experiment. *JOSA A*, 18(8):1986–1992, 2001. (Cité page 13.)
- [6] W. Koechner. *Solid-State Laser Engineering*. Springer Series in Optical Sciences. Springer, 2006. (Cité page 14.)
- [7] I.V Mochalov. Laser and nonlinear properties of the potassium gadolinium tungstate laser crystal  $\text{KGd}(\text{WO}_4)_2\text{Nd}^{3+}$ . *Opt. Eng.*, 36(6):1660–1669, 1997. (Cité pages 14, 46, 48 et 63.)
- [8] S. Chénais, F. Druon, S. Forget, F. Balembois, and P. Georges. On thermal effects in solid-state lasers: The case of ytterbium-doped materials. *Progress in Quantum Electronics*, 30(4):89–153, 2006. (Cité pages 15 et 85.)
- [9] A.K. Cousins. Temperature and thermal stress scaling in finite-length end-pumped laser rods. *Quantum Electronics, IEEE Journal of*, 28(4):1057–1069, 1992. (Cité page 15.)
- [10] S. Biswal, S.P. O’Connor, and S.R. Bowman. Thermo-optical parameters measured in ytterbium-doped potassium gadolinium tungstate. *App. Opt.*, 44(15):3093–3097, 2005. (Cité pages 16, 51, 92, 107, 113, 117, 134 et 136.)

- [11] R.C. Powell. *Symmetry, Group Theory, and the Physical Properties of Crystals*, volume 824. Lecture Notes in Physics, 2010. (Cité page 20.)
- [12] A. Yariv and P. Yeh. *Optical Waves in Crystals: Propagation and Control of Laser Radiation*. Wiley Series in Pure and Applied Optics. Wiley, 2002. (Cité page 21.)
- [13] M.C. Pujol, M. Rico, C. Zaldo, R. Solé, V. Nikolov, X. Solans, M. Aguiló, and F. Diaz. Crystalline structure and optical spectroscopy of  $\text{Er}^{3+}$ -doped  $\text{KGd}(\text{WO}_4)_2$  single crystals. *Appl. Phys. B*, 68:187–197, 1999. (Cité pages 23, 34, 35, 37, 63, 73, 77, 78, 80 et 114.)
- [14] A. Majchrowski, M.T. Borowiec, and E. Michalski. Top seeded solution growth of  $\text{KHo}(\text{WO}_4)_2$  single crystals. *Journal of crystal growth*, 264(1):201–207, 2004. (Cité page 23.)
- [15] M.C. Pujol, R. Solé, J. Massons, Jna. Gavalda, X. Solans, C. Zaldo, F. Díaz, and M. Aguiló. Structural study of monoclinic  $\text{KGd}(\text{WO}_4)_2$  and effects of lanthanide substitution. *Journal of Applied Crystallography*, 34(1):1–6, 2001. (Cité pages 24 et 80.)
- [16] M.C. Pujol, X. Mateos, A. Aznar, X. Solans, S. Suriñach, J. Massons, F. Díaz, and M. Aguiló. Structural redetermination, thermal expansion and refractive indices of  $\text{KLu}(\text{WO}_4)_2$ . *Journal of Applied Crystallography*, 39(2):230–236, Apr 2006. (Cité pages 24 et 63.)
- [17] X. Mateos, R. Solé, Jna. Gavalda, M. Aguiló, J. Massons, and F. Díaz. Crystal growth, optical and spectroscopic characterisation of monoclinic  $\text{KY}(\text{WO}_4)_2$  co-doped with  $\text{Er}^{3+}$  and  $\text{Yb}^{3+}$ . *Optical Materials*, 28(4):423 – 431, 2006. (Cité pages 24 et 37.)
- [18] W.L. Bond. Measurement of the refractive indices of several crystals. *Journal of Applied Physics*, 36(5):1674–1677, 1965. (Cité page 32.)
- [19] A.A. Kaminskii, A.F. Konstantinova, V.P. Orekhova, A.V. Butashin, R.F. Klevtsova, and A.A. Pavlyuk. Optical and nonlinear laser properties of the  $\chi$  (3)-active monoclinic  $\alpha$ - $\text{KY}(\text{WO}_4)_2$  crystals. *Crystallography Reports*, 46(4):665–672, 2001. (Cité pages 34, 35, 37, 78 et 79.)
- [20] C. Traum, P.L. Inácio, C. Felix, P. Segonds, A. Peña, J. Debray, B. Boulanger, Y. Petit, D. Rytz, and G. Montemezzani. Direct measurement of the dielectric frame rotation of monoclinic crystals as a function of the wavelength. *Optical Materials Express*, 4(1):57–62, 2014. (Cité page 35.)

- [21] A.F. Konstantinova, V.V. Filippov, S.P. Palto, E.A. Evdishchenko, K.B. Imangazieva, and V.P. Orekhova. Investigation of the Optical Properties of  $\text{KGd}(\text{WO}_4)_2:\text{Nd}^{3+}$  Crystals with Allowance for Absorption. *Crystallography Reports*, 52(6):1079–1087, 2007. (Cité pages 35, 37, 76, 77 et 114.)
- [22] P.A. Loiko, V.V. Filippov, N.V. Kuleshov, A.A. Pavlyuk, and K.V. Yumashev. All-space existence and dispersion of athermal directions in monoclinic  $\text{KY}(\text{WO}_4)_2$ . *Optics Communications*, 326:144–149, 2014. (Cité pages 35, 37 et 77.)
- [23] M.C. Pujol, J. Massons, M. Aguiló, F. Diaz, M. Rico, and C. Zaldo. Emission Cross Sections and Spectroscopy of  $\text{Ho}^{3+}$  Laser Channels in  $\text{KGd}(\text{WO}_4)_2$  Single Crystal. *Journal of quantum electronics*, 38(1), 2002. (Cité pages 39 et 80.)
- [24] Y. Petit, B. Boulanger, P. Segonds, C. Félix, B. Ménaert, J. Zaccaro, and G. Aka. Absorption and fluorescence anisotropies of monoclinic crystals: the case of  $\text{Nd}:\text{YCOB}$ . *Opt. Express*, 16(11):7997–8002, 2008. (Cité pages 39, 42 et 57.)
- [25] V. Jambunathan, X. Mateos, M.C. Pujol, J.J. Carvajal, M. Aguiló, F. Díaz, U. Griebner, and V. Petrov. Diode-pumped ho-doped  $\text{KLu}(\text{WO}_4)_2$  laser at  $2.08 \mu\text{m}$ . *Applied Physics Express*, 4(7):072601, 2011. (Cité page 40.)
- [26] S. Bjurshagen, P. Brynolfsson, V. Pasiskevicius, I. Parreu, M.C. Pujol, A. Pena, M. Aguilo, and F. Diaz. Crystal growth, spectroscopic characterization, and eye-safe laser operation of erbium- and ytterbium-codoped  $\text{KLu}(\text{WO}_4)_2$ . *Applied optics*, 47(5):656–665, 2008. (Cité page 40.)
- [27] V. Jambunathan, X. Mateos, M.C. Pujol, J.J. Carvajal, J. Massons, M. Aguilo, and F. Diaz. Near-infrared photoluminescence from  $\text{Ho}^{3+}$ -doped monoclinic  $\text{KLu}(\text{WO}_4)_2$  crystal codoped with  $\text{Tm}^{3+}$ . *Journal of Luminescence*, 129(12):1882–1885, 2009. (Cité pages 40 et 81.)
- [28] X. Mateos, V. Jambunathan, M.C. Pujol, J.J. Carvajal, F. Díaz, M. Aguiló, U. Griebner, and V. Petrov. CW lasing of Ho in  $\text{KLu}(\text{WO}_4)_2$  in-band pumped by a diode-pumped  $\text{Tm}:\text{KLu}(\text{WO}_4)_2$  laser. *Opt. Express*, 18(20):20793–20798, 2010. (Cité pages 40, 43, 45 et 81.)

- [29] Yujin Chen, Yanfu Lin, Xinghong Gong, Qiguang Tan, Jian Zhuang, Zundu Luo, and Yidong Huang. Polarized spectroscopic properties of Nd<sup>3+</sup>-doped KGd(WO<sub>4</sub>)<sub>2</sub> single crystal. *Journal of Luminescence*, 126(2):653 – 660, 2007. (Cité pages 40 et 41.)
- [30] R. Soulard, A. Zinoviev, J.L. Doualan, E. Ivakin, O. Antipov, and R. Moncorgé. Detailed characterization of pump-induced refractive index changes observed in Nd: YVO<sub>4</sub>, Nd: GdVO<sub>4</sub> and Nd: KGW. *Optics express*, 18(2):1553–1568, 2010. (Cité page 40.)
- [31] V. Petrov, M.C. Pujol, X. Mateos, O. Silvestre, S. Rivier, M. Aguiló, R.M. Solé, J. Liu, U Griebner, and F. Díaz. Growth and properties of KLu(WO<sub>4</sub>)<sub>2</sub>, and novel ytterbium and thulium lasers based on this monoclinic crystalline host. *Laser & Photonics Reviews*, 1(2):179–212, 2007. (Cité pages 41 et 80.)
- [32] Y. Petit, S. Joly, P. Ségonds, and B. Boulanger. Recent advances in monoclinic crystal optics. *Laser & Photonics Reviews*, 7(6):920–937, 2013. (Cité pages 41, 45 et 80.)
- [33] J.Q. Yao and T.S. Fahlen. Calculations of optimum phase match parameters for the biaxial crystal KTiOPO<sub>4</sub>. *Journal of applied physics*, 55(1):65–68, 1984. (Cité pages 41, 57 et 63.)
- [34] Y. Petit. *Nouvelles approches en optique cristalline: distributions angulaires de l'absorption et de l'émission, auto-doublage, quasi-accord de phase angulaire*. PhD thesis, Université Joseph-Fourier-Grenoble I, 2007. (Cité page 41.)
- [35] R.L. Aggarwal, D.J. Ripin, J.R. Ochoa, and T.Y. Fan. Measurement of thermo-optic properties of Y<sub>3</sub>Al<sub>5</sub>O<sub>12</sub>, Lu<sub>3</sub>Al<sub>5</sub>O<sub>12</sub>, YAIO<sub>3</sub>, LiYF<sub>4</sub>, LiLuF<sub>4</sub>, BaY<sub>2</sub>F<sub>8</sub>, KGd(WO<sub>4</sub>)<sub>2</sub>, and KY(WO<sub>4</sub>)<sub>2</sub> laser crystals in the 80–300K temperature range. *Journal of Applied Physics*, 98(10):–, 2005. (Cité pages 46 et 47.)
- [36] Ò. Silvestre, J. Grau, M.C. Pujol, J. Massons, M. Aguiló, F. Díaz, M.T. Borowiec, A. Szewczyk, M.U. Gutowska, M. Massot, A. Salazar, and V. Petrov. Thermal properties of monoclinic KLu(WO<sub>4</sub>)<sub>2</sub> as a promising solid state laser host. *Opt. Express*, 16(7), 2008. (Cité page 46.)
- [37] V.V. Filippov, N.V. Kuleshovuleshov, and I.T. Bodnar. Negative thermo-optical coefficients and athermal directions in monoclinic

- KGd(WO<sub>4</sub>)<sub>2</sub> and KY(WO<sub>4</sub>)<sub>2</sub> laser host crystals in the visible region. *App. Phys. B*, 87:611–614, 2007. (Cité page 48.)
- [38] P.A. Loiko, K.V. Yumashev, N.V. Kuleshov, and A.A. Pavlyuk. Thermo-optic coefficients and thermal lensing in Nd-doped KGd(WO<sub>4</sub>)<sub>2</sub> laser crystals. *App. Opt.*, 49(34):6651–6659, 2010. (Cité pages 48 et 80.)
- [39] V.V. Filippov. Athermal directions in KGd(WO<sub>4</sub>)<sub>2</sub> and KLu(WO<sub>4</sub>)<sub>2</sub> crystals under uniform heating. *Applied optics*, 52(18):4377–4384, 2013. (Cité page 48.)
- [40] P.A. Loiko, K.V. Yumashev, N.V. Kuleshov, G.E. Rachkovskaya, and A.A. Pavlyuk. Thermo-optic dispersion formulas for monoclinic double tungstates KRe(WO<sub>4</sub>)<sub>2</sub> where Re= Gd, Y, Lu, Yb. *Optical Materials*, 33(11):1688–1694, 2011. (Cité page 48.)
- [41] A.M. Belskii and A.P. Khapalyuk. Internal conical refraction of bounded light beams in biaxial crystals. *Optics and Spectroscopy*, 44:436–439, 1978. (Cité pages 49, 62 et 64.)
- [42] H. Lloyd. On the phenomena presented by light in its passage along the axes of biaxial crystals. *Phil. Mag.*, 1, 1833. (Cité page 50.)
- [43] J.C. Poggendorff. Ueber die konische refraction. *Pogg. Ann*, 48:461–462, 1839. (Cité page 50.)
- [44] G.S. Sokolovskii, D.J. Carnegie, T.K. Kalkandjiev, and E.U. Rafailov. Conical refraction: New observations and a dual cone model. *Opt. Express*, 21(9):11125–11131, 2013. (Cité page 50.)
- [45] C.V. Raman, V.S. Rajagopalan, and T.M.K. Nedungadi. Conical refraction in naphthalene crystals. *Proceedings Mathematical Sciences*, 14(3):221–227, 1941. (Cité pages 50 et 69.)
- [46] D.L. Portigal and E. Burstein. Internal conical refraction. *JOSA*, 59(12):1567–1573, 1969. (Cité pages 50, 54 et 62.)
- [47] N. Bloembergen and H. Shih. Conical refraction in nonlinear optics. *Optics Communications*, 1(2):70–72, 1969. (Cité page 50.)
- [48] H. Shih and N. Bloembergen. Conical Refraction in Second-Harmonic Generation. *Phys. Rev.*, 184:895–904, Aug 1969. (Cité pages 50 et 51.)

- [49] É. Lalor. An analytical approach to the theory of internal conical refraction. *Journal of Mathematical Physics*, 13(4):449–454, 1972. (Cité pages 50 et 62.)
- [50] A.J. Schell and N. Bloembergen. Laser studies of internal conical diffraction. II. Intensity patterns in an optically active crystal,  $\alpha$ -iodic acid. *JOSA*, 68(8):1098–1106, 1978. (Cité page 50.)
- [51] J.P. Fève, B. Boulanger, and G. Marnier. Experimental study of internal and external conical refractions in KTP. *Optics communications*, 105(3):243–252, 1994. (Cité page 50.)
- [52] B. Boulanger, J.P. Feve., G. Marnier, G.M. Loiacono, D.N. Loiacono, and C. Bonnin. SHG and internal conical refraction experiments in CsTiOAsO<sub>4</sub>, comparison with KTiOPO<sub>4</sub> and KTiOAsO<sub>4</sub>, for 1.32- $\mu$ m type II SHG. *Quantum Electronics, IEEE Journal of*, 33(6):945–949, 1997. (Cité page 50.)
- [53] M.V. Berry and M.R. Jeffrey. Conical diffraction asymptotics: fine structure of Poggendorff rings and axial spike. *J. Opt. A*, 6:289–300, 2004. (Cité pages 51, 62, 64 et 65.)
- [54] A. Belafhal. Theoretical intensity distribution of the internal conical refraction. *Optics communications*, 178(4):257–265, 2000. (Cité page 51.)
- [55] A.M. Belsky and M.A. Stepanov. Internal conical refraction of light beams in biaxial gyrotropic crystals. *Optics Communications*, 204(1–6):1–6, 2002. (Cité page 51.)
- [56] M.R. Jeffrey. *Conical Diffraction: Complexifying Hamilton's Diabolical Legacy*. PhD thesis, University of Bristol, 2007. (Cité pages 51, 52 et 64.)
- [57] R.P. Burns. On the possibility of using conical refraction phenomena for laser beam steering. *Applied Optics*, 3(12):1505–1506, 1964. (Cité page 51.)
- [58] Y.P. Mikhailichenko. Conical refraction: Experiments and large-scale demonstrations. *Russian Physics Journal*, 50(8):788–795, 2007. (Cité pages 51 et 57.)
- [59] C.F. Phelan, D.P. O'dwyer, Y.P. Rakovich, J.F. Donegan, and J.G. Lunney. Conical diffraction and Bessel beam formation with a high op-

- tical quality biaxial crystal. *OPTICS EXPRESS*, 17(15):12891–12899, 2009. (Cité pages 51 et 65.)
- [60] A. Abdolvand. Conical diffraction from a multi-crystal cascade: experimental observations. *Applied Physics B*, 103(2):281–283, 2011. (Cité pages 51 et 56.)
- [61] R.T. Darcy, D. McCloskey, K.E. Ballantine, B.D. Jennings, J.G. Lunney, P.R. Eastham, and J.F. Donegan. White light conical diffraction. *Optics express*, 21(17):20394–20403, 2013. (Cité page 51.)
- [62] R.T. Darcy, D. McCloskey, K.E. Ballantine, J.G. Lunney, P.R. Eastham, and J.F. Donegan. Conical diffraction intensity profiles generated using a top-hat input beam. *Optics Express*, 22(9):11290–11300, 2014. (Cité pages 51 et 64.)
- [63] A. Turpin, Y.V. Loiko, T.K. Kalkandjiev, H. Tomizawa, and J. Mompart. Wave-vector and polarization dependence of conical refraction. *Optics express*, 21(4):4503–4511, 2013. (Cité pages 51 et 64.)
- [64] A. Turpin, Y.V. Loiko, T.K. Kalkandkiev, H. Tomizawa, and J. Mompart. Super-Gaussian conical refraction beam. *Optics letters*, 39(15):4349–4352, 2014. (Cité pages 51 et 64.)
- [65] A. Turpin, Y.V. Loiko, T.K. Kalkandjiev, and J. Mompart. Multiple rings formation in cascaded conical refraction. *Opt. Lett.*, 38(9):1455–1457, May 2013. (Cité pages 51, 56 et 64.)
- [66] V. Peet. The far-field structure of Gaussian light beams transformed by internal conical refraction in a biaxial crystal. *Optics Communications*, 311:150–155, 2013. (Cité pages 51, 66, 67 et 68.)
- [67] V. Peet. Experimental study of internal conical refraction in a biaxial crystal with Laguerre–Gauss light beams. *Journal of Optics*, 16(7):075702, 2014. (Cité pages 51 et 64.)
- [68] S.D. Grant and A. Abdolvand. Evolution of conically diffracted gaussian beams in free space. *Optics express*, 22(4):3880–3886, 2014. (Cité page 51.)
- [69] C.F. Phelan, K.E. Ballantine, P.R. Eastham, J.F. Donegan, and J.G. Lunney. Conical diffraction of a Gaussian beam with a two crystal cascade. *Optics express*, 20(12):13201–13207, 2012. (Cité pages 51, 56 et 64.)

- [70] V. Peet. Biaxial crystal as a versatile mode converter. *J. Opt.*, 12(9):095706, 2010. (Cité page 51.)
- [71] V. Peet. Conical refraction and formation of multiring focal image with Laguerre-Gauss light beams. *Opt. Letters*, 36:2913–2915, 2011. (Cité pages 51 et 64.)
- [72] N.A. Khilo. Conical diffraction and transformation of Bessel beams in biaxial crystals. *Opt. Communications*, 286:1–5, 2013. (Cité page 51.)
- [73] C.F. Phelan, J.F. Donegan, and J.G. Lunney. Generation of a radially polarized light beam using internal conical diffraction. *Opt. Express*, 19:21793–21802, 2011. (Cité page 51.)
- [74] D.P. O'Dwyer, C.F. Phelan, Y.P. Ralovich, P.R. Eastham, J.G. Lunney, and J.F. Donegan. The creation and annihilation of optical vortices using cascade conical diffraction. *Opt. Express*, 19:2580–2588, 2011. (Cité page 51.)
- [75] Y.V. Loiko, A. Turpin, T.K. Kalkandjiev, E.U. Rafailov, and J. Mompart. Generating a three-dimensional dark focus from a single conically refracted light beam. *Optics letters*, 38(22):4648–4651, 2013. (Cité page 51.)
- [76] J. Hellström, H. Henricsson, V. Pasiskevicius, U. Bünting, and D. Haussmann. Polarization-tunable Yb:KGW laser based on internal conical refraction. *Opt. Lett.*, 32(19):2783–2785, 2007. (Cité pages 51 et 107.)
- [77] A. Abdolvand, K.G. Wilcox, T.K. Kalkandjiev, and E.U. Rafailov. Conical refraction Nd:KGd(WO<sub>4</sub>)<sub>2</sub> laser. *Opt. Express*, 18(3):2753–2759, 2010. (Cité pages 51, 83, 84, 86, 87, 92, 115, 134 et 136.)
- [78] K.G. Wilcox, A. Abdolvand, T.K. Kalkandjiev, and E.U. Rafailov. Laser with simultaneous gaussian and conical refraction outputs. *Applied Physics B*, 99:619–622, 2010. (Cité pages 51, 83, 84, 92, 107, 115, 134 et 136.)
- [79] Amin Abdolvand, K.G. Wilcox, T.K. Kalkandjiev, and E.U. Rafailov. Cone-refrangent solid-state bulk laser. In *Lasers and Electro-Optics 2009 and the European Quantum Electronics Conference. CLEO Europe - EQEC 2009. European Conference on*, pages 1–1, June 2009. (Cité pages 51, 84, 92, 107, 115, 134 et 136.)

- [80] S. Rosen, G.Y. Sirat, H. Ilan, and A.J. Agranat. A sub wavelength localization scheme in optical imaging using conical diffraction. *Opt. Express*, 21(8):10133–10138, Apr 2013. (Cité page 51.)
- [81] G.Y. Sirat, S. Shorte, L.P.O. Braitbart, L. Moisan, J.Y. Tinevez, J. Caron, and C. Fallet. Conical Diffraction Based Super-resolution System for Fluorescence Microscopy: System Description and Demonstration visualizing Biological Objects. *Microscopy and Microanalysis*, 19(S2):1178–1179, 2013. (Cité page 51.)
- [82] D.P. O’Dwyer, K.E. Phelan, C.F. Ballantine, P.R. Rakovich, J.G. Lunney, and J.F. DoneganODW10. Conical diffraction of linearly polarised light controls the angular position of a microscopic object. *Opt. Express*, 18(26):27319–27326, 2010. (Cité page 51.)
- [83] A. Turpin, V. Shvedov, C. Hnatovsky, Y.V. Loiko, J. Mompart, and W. Krolikowski. Optical vault: A reconfigurable bottle beam based on conical refraction of light. *Opt. Express*, 21(22):26335–26340, 2013. (Cité page 51.)
- [84] C. McDonald, C. McDougall, E. Rafailov, and D. McGloin. Characterising conical refraction optical tweezers. *arXiv preprint arXiv:1408.6987*, 2014. (Cité page 51.)
- [85] A.J. Schell and N. Bloembergen. Laser studies of internal conical diffraction. III. Second-harmonic conical refraction in  $\alpha$ -iodic acid. *Physical Review A*, 18(6):2592, 1978. (Cité page 51.)
- [86] S.A. Zolotovskaya, A. Abdolvand, T.K. Kalkandjiev, and E.U. Rafailov. Second-harmonic conical refraction: observation of free and forced harmonic waves. *Applied Physics B*, 103(1):9–12, 2011. (Cité page 51.)
- [87] A. Turpin, Y.V. Loiko, T.K. Kalkandjiev, J. Trull, C. Cojocar, and J. Mompart. Type I and type II second harmonic generation of conically refracted beams. *Optics letters*, 38(14):2484–2486, 2013. (Cité page 51.)
- [88] S.D. Grant, S.A. Zolotovskaya, T.K. Kalkandjiev, W.A. Gillespie, and A. Abdolvand. On the frequency-doubled conically-refracted Gaussian beam. *Optics express*, 22(18):21347–21353, 2014. (Cité page 51.)

- [89] D.P. O'Dwyer, C.F. Phelan, Y.P. Rakovich, P.R. Eastham, J.G. Lunney, and J.F. Donegan. Generation of continuously tunable fractional optical orbital angular momentum using internal conical diffraction. *Optics express*, 18(16):16480–16485, 2010. (Cité page 51.)
- [90] K.E. Ballantine, J.F. Donegan, and P.R. Eastham. Conical diffraction and the dispersion surface of hyperbolic metamaterials. *Physical Review A*, 90(1):013803, 2014. (Cité page 51.)
- [91] M.V. Berry. Conical diffraction from an n-crystal cascade. *J. Opt. A*, 12:6651–6659, 2010. (Cité pages 56 et 64.)
- [92] M. Born, E. Wolf, A.B. Bhatia, D. Gabor, A.R. Stokes, A.M. Taylor, P.A. Wayman, and W.L. Wilcock. *Principles of Optics: Electromagnetic Theory of Propagation, Interference and Diffraction of Light*. Cambridge University Press, 2000. (Cité pages 58 et 72.)
- [93] M. Sluijter. *RAY-OPTICS ANALYSIS OF INHOMOGENEOUS OPTICALLY ANISOTROPIC MEDIA*. PhD thesis, Technische Universiteit Delft, 2010. (Cité page 59.)
- [94] W.R. Hamilton. Third supplement to an essay on the theory of systems of rays. *Transactions of the Royal Irish Academy*, 17(part 1):1–144, 1837. (Cité page 62.)
- [95] M.V. Berry, M.R. Jeffrey, and J.G. Lunney. Conical diffraction: observations and theory. *Proc. R. Soc. A*, 462:1629–1642, 2006. (Cité page 63.)
- [96] H.P. Christensen, H.P. Jenssen, and D.R. Gabbe. BaY<sub>2</sub>F<sub>8</sub> as a host for Ln ions, I: Optical properties of the crystal and spectroscopic results for Pr, Dy, Ho, and Er doping. (Cité page 63.)
- [97] Y.W. Zhao, X.H. Gong, Y.J. Chen, L.X. Huang, Y.F. Lin, G. Zhang, Q.G. Tan, Z.D. Luo, and Y.D. Huang. Spectroscopic properties of Er<sup>3+</sup> ions in Li<sub>6</sub>Y(BO<sub>3</sub>)<sub>3</sub> crystal. *Appl. Phys. B*, 88:51–55, 2007. (Cité page 63.)
- [98] H. Hellwig, J. Liebertz, and L. Bohaty. Linear optical properties of the monoclinic bismuth borate BiB<sub>3</sub>O<sub>6</sub>. *J. App. Phys.*, 88(1):240–244, 2000. (Cité page 63.)
- [99] P.A. Loiko, K.V. Yumashev, N.V. Kuleshov, and A.A. Pavlyuk. Thermo-optical properties of pure and yb-doped monoclinic KY

- (WO<sub>4</sub>)<sub>2</sub> crystals. *Applied Physics B*, 106(3):663–668, 2012. (Cité page 80.)
- [100] S. Vatik, M.C. Pujol, J.J. Carvajal, X. Mateos, M. Aguiló, F. Díaz, and V. Petrov. Thermo-optic coefficients of monoclinic KLu(WO<sub>4</sub>)<sub>2</sub>. *Applied Physics B*, 95(4):653–656, 2009. (Cité page 80.)
- [101] Y. Petit, S. Joly, P. Segonds, and B. Boulanger. Refined modeling of angular distributions of linear absorption and fluorescence in biaxial crystals. *Laser Physics*, 21(7):1305–1312, 2011. (Cité page 80.)
- [102] R. Moncorgé, B. Chambon, J.Y. Rivoire, N. Garnier, E. Descroix, P. Laporte, H. Guillet, S. Roy, J. Mareschal, D. Pelenc, et al. Nd doped crystals for medical laser applications. *Optical Materials*, 8(1):109–119, 1997. (Cité page 85.)
- [103] P.A. Loiko, V.G. Savitski, A. Kemp, A.A. Pavlyuk, N.V. Kuleshov, and K.V. Yumashev. Anisotropy of the photo-elastic effect in Nd<sup>3+</sup>:KGd(WO<sub>4</sub>)<sub>2</sub> laser crystals. *Laser Physics Letters*, 11(5):055002, 2014. (Cité page 92.)
- [104] M.V. Berry, M.R. Jeffrey, and M. Mansuripur. Orbital and spin angular momentum in conical diffraction. *Journal of Optics A: Pure and Applied Optics*, 7(11):685, 2005. (Cité page 101.)
- [105] S. Joly, P. Segonds, B. Boulanger, Y. Petit, A.P. Revellez, C. Félix, and B. Ménaert. Rotation of the absorption frame as a function of the electronic transition in the Nd<sup>3+</sup>:YCa<sub>4</sub>O(BO<sub>3</sub>)<sub>3</sub> monoclinic crystal. *Optics express*, 18(18):19169–19174, 2010. (Cité page 114.)





**Titre** Investigation sur des sources lasers émettant à  $2 \mu\text{m}$  utilisant des cristaux monocliniques

**Résumé** Cette thèse est consacrée à l'étude du potentiel des cristaux biaxes dans le but de réaliser un laser de puissance. Les cristaux biaxes possèdent deux axes optiques ce qui donnent lieu à un effet appelé "réfraction (ou diffraction) conique". Cet effet, connu depuis 1832, est intensément étudié depuis une décennie. Les progrès en croissance et découpe cristalline permettent d'obtenir des échantillons de longueurs et de qualités optiques suffisantes pour observer ce phénomène. L'utilisation de cet effet en cavité laser ayant déjà été réalisée [79, 78], l'objectif de cette thèse fut dans un premier temps de confirmer ces résultats. Ainsi, un système utilisant des cristaux de  $\text{KGd}(\text{WO}_4)_2$  (KGW) dopés au Néodyme a été préalablement testé. Ces premiers résultats furent décevants. La stabilité, la qualité de faisceau ainsi que l'efficacité étaient plus que médiocres. L'efficacité maximale fut d'environ 40 % contre 74 % dans la publication [77]. Par ailleurs, le faisceau de sortie présentait un profil elliptique indiquant la présence d'une lentille thermique avec un fort astigmatisme. Ainsi, cette orientation, qui devrait être proche d'une direction athermale (ne présentant pas d'astigmatisme d'origine thermique) selon Biswal [10], ne l'est pas dans une cavité laser pour ce cristal. De plus ce laser est très peu stable et difficile à aligner. Les fluctuations importantes de l'efficacité de celui-ci ont abouti à une interrogation quant à la dépendance des propriétés optiques aux alentours de l'axe optique. Ainsi, dans les premiers chapitres de cette thèse, figurent une étude détaillée des principales propriétés optiques d'absorption et d'émission. Les résultats de cette étude montrent que ces propriétés varient non seulement suivant la polarisation mais également suivant l'orientation aux alentours de l'axe optique. Etant donné que l'état de polarisation autour de l'axe optique varie avec l'orientation, les dépendances en orientation et polarisation sont liées. C'est pourquoi une étude simple de la réfraction est fournie afin de comprendre cette dépendance complexe. Après ces premières expérimentations laser, le cas de cristaux de  $\text{KY}(\text{WO}_4)_2$  (KYW) dopés Holmium pour une émission laser à  $2 \mu\text{m}$  a été étudié. Le choix de l'Holmium comme dopant est lié à son faible "défaut quantique" entre la longueur d'onde de pompe (1960 nm) et la longueur d'émission (2074 nm). Avoir un faible "défaut quantique" permet d'avoir une longueur d'onde de pompe et d'émission proches et réduit ainsi la dispersion potentiel de l'axe optique entre ces deux longueurs d'onde. Ainsi, lorsque la longueur

d'onde de pompe est alignée, la longueur d'onde d'émission laser l'est également. Ceci justifie que l'ion Thulium a été négligé, bien qu'il puisse avoir une bonne efficacité avec une longueur d'onde de pompe de 790 nm grâce à l'effet de relaxation croisée présent dans cet ion. Grâce à un montage amélioré par rapport aux premières expériences effectuées avec les cristaux KGW dopés au Néodyme, la dépendance de la polarisation ainsi que de l'orientation a pu être mise en évidence. Différents rendements ont pu être atteints en fonction de l'orientation du cristal. Une efficacité atteignant jusqu'à 70 % pour une puissance de sortie d'environ 3 W a pu être obtenue pour une orientation proche de l'axe optique. Le taux de dopage des cristaux de KYW dopés à l'Holmium étant plus approprié au fonctionnement à forte puissance, l'astigmatisme dû à la lentille thermique n'a pas été observé. Par ailleurs, l'alignement de la cavité laser avec l'axe optique a pu être réalisé. Ainsi, nous avons prouvé qu'un mode laser « conique » est possible dans une cavité conçue pour des faisceaux Gaussiens. Cependant, la dépendance entre les propriétés optiques et l'orientation entraîne *de facto* une efficacité moindre qu'un mode Gaussien classique. Des efficacités honorables atteignant presque 50 % ont pu être obtenues suivant cette orientation. Aucun problème de lentille thermique n'a pu être observé avec une puissance de pompe maximale de 6 W. Le taux de dopage faible ainsi que la longueur de plus de 1 cm des cristaux permettent une bonne répartition thermique dans le cristal. Une puissance de pompe supérieure (plusieurs dizaines de watts) est nécessaire pour atteindre les limites de fonctionnement de ces cristaux. Enfin, un montage innovant a été testé afin d'utiliser la réfraction conique. La puissance de sortie ainsi que l'efficacité de ce montage étaient très faibles, environ 800 mW en sortie pour 4 W de puissance de pompe.

**Mots-clés** laser, tungstates, réfraction conique, KYW, KGW, Holmium

**Title** Investigation on 2  $\mu\text{m}$  laser sources based on monoclinic host crystals

**Abstract** This thesis is devoted to the study on the potential of biaxial crystals in order to increase laser output power. Biaxial crystals have two optic axes and an effect called conical refraction (or diffraction) can occur. This effect is known since 1832, and intensively studied since the last decade. Thanks to the progress of crystal growth and crystal cutting, it is possible to have long samples of good optical quality in order to ob-

serve the conical refraction. This effect has already been used in a laser cavity [79, 78]. The aim of this thesis was to confirm the results previously obtained. Thus, Neodymium-doped  $\text{KGd}(\text{WO}_4)_2$  (KGW) crystals, cut along the optic axis, have been tested. These first results were disappointing. Stability, beam quality and efficiency were very low. The maximum efficiency achieved was around 40% compared to the 74% claimed in publication [77]. Thus, this orientation which should be an athermal direction using the calculation of Biswal [10] shows astigmatism when there is a temperature gradient. Furthermore, this laser being difficult to align with strong intensity fluctuations, rise interrogations about the optical property variations around the optic axis. Thus, in the first Chapters of this thesis a study of those properties around the optic axis is given. It shows a strong variation of the optical properties depending on the polarization and orientation around the optic axis. The study of the refraction along the optic axis helps to understand this complex dependency with the orientation. In a second time, holmium-doped  $\text{KY}(\text{WO}_4)_2$  (KYW) crystals have been tested for laser emission at  $2 \mu\text{m}$ . The choice of this ion has been done on several criteria. The first one is that the ISL laboratory is used to work with this wavelength and has a lot of equipment. The second one is that Holmium ions have a small "quantum defect" (pump wavelength 1960 nm and lasing wavelength 2074 nm). This low "quantum defect" limits the dispersion between the pump and lasing wavelengths. This decreases the separation between the optic axes of both wavelengths. Thus, when the pump is aligned for conical refraction the lasing wavelength is also aligned along the optic axis. Thanks to a better setup (with new mechanical parts) the polarization and orientation dependencies of the laser efficiency have been investigated. Up to 3 W of output power with a slope efficiency of 70% has been reached near the optic axis. The doping concentration of the Holmium-doped  $\text{KY}(\text{WO}_4)_2$  (KYW) being more appropriated for high power laser, no thermal lens effect has been observed. Furthermore, the first conical refraction laser with a quasi-three-level system has been realized. An efficiency of 50% has been achieved with such a conical refraction laser. Finally, a new innovative setup is proposed using the External Conical Refraction. An output power of 800 mW for 4 W of incident pump power has been reached.

**Keywords** laser, tungstates, conical refraction, conical diffraction, KYW, KGW, Holmium